Experimental and Computational Investigation of Colloidal Semiconductor Nanocrystals with Excess Charge Carriers: Effects of Surface Interactions on Electronic Properties

Anna Merkulova

A dissertation

submitted in partial fulfillment of the

requirements for the degree of

Doctor of Philosophy

University of Washington

2023

Reading Committee:

Scott T. Dunham, Chair

Daniel R. Gamelin

Brandi M. Cossairt

Program Authorized to Offer Degree:

Chemistry

University of Washington

Abstract

Experimental and Computational Investigation of Colloidal Semiconductor Nanocrystal with Excess Charge Carriers: Effects of Surface Interactions on Electronic Properties

Anna Merkulova

Chair of the Supervisory Committee:

Professor Scott T. Dunham

Department of Electrical & Computer Engineering

Band engineering in nanomaterials facilitates wide variety of applications in semiconductor electronics. Understanding properties that enable and govern band engineering is critical for implementing the functionalities that electronically doped nanocrystals provide. The aim of this work is to better understand the effects of surface interactions on electronic properties of semiconductor nanocrystals, explore the emergence of supercapacitance, and examine the effects of band engineering on electron transfer in complex nanocrystal systems. To achieve this aim, experimental methods for nanocrystal synthesis and characterization are combined with a computational framework for modeling of nanocrystal-ligand interfaces. Unique energy storage properties of ZnO and ZnO-related colloidal nanocrystals are explored with focus on supercapacitance and band edge potential tuning. It is shown that ZnO acquires a surprisingly high capacitance under various conditions, such as aluminum doping, interactions with Li^+,

and shape/media changes, due to electrostatic interactions on the nanocrystal surface and within the tunneled ZnO crystal structure. Modulation of band edge potentials by perturbations in surface chemistry is explored on colloidal PbS, CdS, and CdSe quantum dots. CdS presents a particularly interesting system to investigate, as it exhibits an apparent change in electrochemical properties when mixed with ZnO nanocrystals, forming an electron transfer pair. Experimental evidence and modeling of CdS-ligand interactions support the hypothesis that a shift in band edge potentials happens upon mixing of ZnO and CdS nanocrystals due to change in total dipole caused by new ligands present in the mixture, thus enabling CdS-to-ZnO electron transfer. More broadly, it is shown in this dissertation that ligands have a profound effect on electronic properties of various colloidal nanocrystal materials. The developed computational approach generalizes this phenomenon and offers an opportunity to predict, through modeling, the effects of ligand-nanocrystal interactions on nanocrystal properties and resulting behavior of complex nanomaterial systems. Overall, this work provides new insights into properties of colloidal semiconductor nanocrystals with excess charge carriers and informs rational design and tuning of electronic properties for next-generation nanomaterials and applications.

Table of Contents

LIST OF FIGURES IV

LIST OF TABLES VIII

ACKNOWLEDGEMENTS IX

CHAPTER 1: INTRODUCTION 1

1.1 Semiconductor nanocrystals as versatile tunable materials 1

1.2 Band engineering in semiconductor nanocrystals 2

1.3 Electronic doping in semiconductor nanocrystals 3

1.4 Summary and dissertation overview 4

CHAPTER 2: SPECTROELECTROCHEMISTRY (specEchem) AS A METHOD TO STUDY ELECTRONIC PROPERTIES OF COLLOIDAL NANOCRYSTALS 7

2.1 Methods for characterization of electronic properties of semiconductors 7

2.2 Description of specEchem setup used in this dissertation 8

2.3 Optimization of specEchem for colloidal nanocrystals 9

2.4 Summary 12

CHAPTER 3: COMPUTATIONAL METHODS FOR THE STUDY OF ELECTRONIC PROPERTIES 14

3.1 Using VASP for DFT calculations 14

3.2 Geometry optimization: molecular dynamics and local optimization 15

3.3 Density of states, potentials, and wavefunction analysis 15

3.4 Data post-processing and visualization 16

3.5 Summary 17

CHAPTER 4: PREPARATION AND CHARACTERIZATION OF NANOCRYSTALS WITH TUNABLE ELECTRONIC PROPERTIES 18

4.1 Nanoparticle characterization methods 18

4.2 Preparation of Cu-doped ZnSe nanocrystals 19

4.3 Preparation of PbS nanocrystals 21

4.4 Preparation of CdS nanocrystals 25

4.5 Summary 27

CHAPTER 5: SUPERCAPACITANCE IN ZnO-BASED NANOMATERIALS 28

5.1 Nanocrystal supercapacitors as energy storage materials 28

5.2 Strategies for achieving supercapacitance in colloidal ZnO nanocrystals 30

5.2.1 Effects of electrolyte concentration on ZnO capacitance 30
5.2.2 Increase in capacitance in non-spherical ZnO nanocrystals 32
5.2.3 Emergence of supercapacitance upon ZnO doping with aluminum 33
5.2.4 Li^+-induced supercapacitance in ZnO nanocrystals 39

5.3 Investigating origins of supercapacitance 42

5.4 Summary 45

CHAPTER 6: ELECTRON TRANSFER IN CdS/ZnO COLLOIDAL NANOCRYSTAL SYSTEM 47

6.1 Synthesis and characterization of ZnO and CdS NCs 47

6.2 Electron transfer in CdS/ZnO colloidal nanocrystal system 49

6.3 Kinetics of CdS/ZnO electron exchange 54

6.4 Effect of electrolyte concentration on electron exchange efficiency 58

6.5 Summary 58

CHAPTER 7: CHARACTERIZATION OF THE CdS/ZnO SYSTEM 59

7.1 Experimental investigation of the impact of ligands on NC band edge potential . 60

7.1.1 Ligand treatment of CdS NCs 60
7.1.2 Electron transfer behavior of CdSe NCs 62

7.2 Computational framework for modeling of NC-ligand electronic properties 65
7.2.1 Modeling of nanocrystal facets.....65
7.2.2 Choosing an appropriate ligand model.....68
7.2.3 Global and local optimization of slab-ligand interfaces 69
7.3 Applying computational framework to CdS slab-ligand system..... 69
7.3.1 Analysis of slab-ligand potentials.....70
7.3.2 Structural analysis of bonding in slab-ligand systems 72
7.3.3 DOS analysis of bonding in slab-ligand systems.....74
7.3.4 Effect of NC-ligand interaction on the total dipole of the system 75
7.4 Applying modeling results to CdS/ZnO charge transfer system..... 77
7.5 Summary..... 80

CHAPTER 8: EMERGING APPLICATIONS OF THE COMPUTATIONAL FRAMEWORK FOR MODELING OF NANOCRYSTAL-LIGAND INTERACTIONS.....81
8.1 Electron transfer behavior in CdSe/ZnO nanocrystal system 81
8.2 Going beyond experimentally measured ligands: expanding library of surface molecules..... 83
8.3 Effects of surface passivation on properties of diamond 84
8.4 Impact of ligands on phase stability..... 85
8.5 Summary..... 87

CHAPTER 9: DISSERTATION SUMMARY 88

LITERATURE CITED 91

PYTHON CODE FOR DATA ANALYSIS..... 102

List of Figures

Figure 2.1 SpecEchem setup. 9

Figure 2.2 Gamry potentiostat instrument performance check.....10

Figure 2.3 Measuring the performance error of the potentiostat in organic solvent.....11

Figure 2.4 Potential drift and band edge potential trends in CHCl.....11

Figure 2.5 SpecEchem with LiEt.....12

Figure 3.1 Computational framework for modeling of nanocrystal-ligand interfaces. 17

Figure 4.1 Characterization of ZnSe nanocrystals. 20

Figure 4.2 Characterization of Cu-doped ZnSe nanocrystals. 20

Figure 4.3 Procedure optimization for improved Cu doping.....21

Figure 4.4 Electronic absorption spectrum of as-prepared PbS NCs (d = 5.7 nm) in tetrachloroethylene. 22

Figure 4.5 Spectroelectrochemical potentiometry of PbS NCs. 23

Figure 4.6 Ligand exchange of as-synthesized PbS NCs.....24

Figure 4.7 Spectroelectrochemical potentiometry of PbS NCs after ligand exchange. ...25

Figure 4.8 Electronic absorption spectrum of as-prepared CdS NCs (d = 5.7 nm) in hexane. 26

Figure 4.9 Spectroelectrochemical potentiometry of CdS NCs. 27

Figure 5.1 Effect of electrolyte concentration on capacitance. 31

Figure 5.2 Capacitance and ZnO morphology. 33

Figure 5.3 AZO sample characterization. 34

Figure 5.4 SpecEchem of 15% AZO. 37

Figure 5.5 Change in potentiometric titrations for AZO NCs with different Al content. ..38

Figure 5.6 Crystal structures of Metal Oxide NCs. 40

Figure 5.7 Effect of Li+ on capacitance. 41

Figure 5.8 Spectroscopic investigation of Li doped ZnO nanocrystals. 43

Figure 5.9 Modeling of 1-100 ZnO slabs with Li insertion. 44

Figure 5.10 Modeling of 0001 ZnO slab with Li insertion. 45

Figure 5.11 Summary of the approaches for increasing capacitance in ZnO nanocrystals. 46

Figure 6.1 Characterization of ZnO nanocrystals. 48

Figure 6.2 Characterization of CdS nanocrystals. 48

Figure 6.3 Experimental setup for the study of CdS-to-ZnO electron transfer. 49

Figure 6.4 Control experiment for CdS-selective excitation. 50

Figure 6.5 Simultaneous electronic doping in mixture of CdS and ZnO NCs. 51

Figure 6.6 Quantitative titrations of ZnO NCs. 52

Figure 6.7 Spectroelectrochemical potentiometry in mixture of CdS and ZnO NCs. 53

Figure 6.8 Electron transfer in CdS/ZnO mixture. 54

Figure 6.9 Kinetics of electron transfer. 55

Figure 6.10 Charging of ZnO NCs through charge/discharge of CdS NCs in CdS/ZnO NC mixture. 55

Figure 6.11 Difference in behavior of photodoped electrons in CdS and ZnO NCs. 56

Figure 6.12 SpecEchem of CdS/ZnO NC mixture. 57

Figure 6.13 Electrolyte effect on electron transfer.....58

Figure 7.1 Ligand-induced effects on band edge potential and CdS/ZnO electron transfer. 59

Figure 7.2 Band-edge potentials in CdS/ZnO NC mixture vs individual components.....61

Figure 7.3 Characterization of CdS before and after ligand treatment procedure. 61

Figure 7.4 Spectroelectrochemical characterization of CdSe NCs.....63

Figure 7.5 Electronic absorption spectra of CdSe NCs, collected after various durations of selective photoexcitation in airtight cuvette.....64

Figure 7.6 Facets of a spherical CdS nanocrystal. 66

Figure 7.7 Structure of slab-vacuum unit cell. 66

Figure 7.8 Validation of correct fractional charge of pseudo-H atoms for slab passivation. 67

Figure 7.9 Planar average potentials of CdS slab with different ligand models.....68

Figure 7.10 CdS slab-oleate geometry optimization via simulated annealing. 69

Figure 7.11 DFT modeling of ligand-induced potential differences for CdS slabs along 0001 facet.....71

Figure 7.12 Ligand coverage dependent potential offsets in CdS-oleate. 72

Figure 7.13 Structure analysis of bonding in CdS-molecule systems. 73

Figure 7.14 DOS analysis of bonding in CdS-molecule systems. 74

Figure 7.15 Dipole analysis in CdS slab-ligand system from charge density.....75

Figure 7.16 Dipole analysis in CdS slab-ligand system from differences in planar average potentials.....76

Figure 7.17 Effect of dipoles on potential offsets in CdS slab-ligand system. 77

Figure 7.18 Total charge distribution in CdS slab-ligand system. 78

Figure 7.19 Electron transfer is enabled by changing the CdS NC environment in solution. 79

Figure 8.1 Potential offset calculated for CdSe slab with different ligands. 82

Figure 8.2 Predicting NC band edge potentials from modeling inorganic ligands. 83

Figure 8.3 Modeling of diamond slab. 84

Figure 8.4 Modeling of bornite.....86

Figure 8.5 Modeling of elpasolite.....86

List of Tables

Table 5.1 Capacitance of ZnO NCs electronically doped in different environment. 32

Table 5.2 Capacitance of AZO NCs with different Al content. 39

Table 7.1 Transformation matrix to expose 1-100 facet from 0001 67

Table 7.2 Transformations to expose 1-101 facet from 1-100 67

Table 7.3 Calculated potential differences for different facets of CdS 70

Table 7.4 Position and magnitude of dipole in CdS-ligand system 76

Table 8.1 Formation energies of elpasolite and its decomposition products 87

Acknowledgements

Throughout my academic career I have been fortunate to work with great educators, mentors, and scientists, who inspired me to pursue research in Chemistry – I would like to sincerely thank all my teachers, colleagues, friends, and family for their invaluable guidance and support during this journey. I am deeply grateful to my research advisor Scott Dunham for giving me an opportunity to engage in computational work and make modeling a major part of my dissertation. As an experimental researcher entering the world of computational chemistry, I truly appreciated Scott's patience and willingness to teach me and help me climb the steep learning curve, making connections between experimental systems and computational models. I would also like to thank Daniel Gamelin, who welcomed me to his lab first as an undergraduate intern and then as a new graduate student in the Department of Chemistry, guiding me through formulating research hypotheses and developing experimental systems for my dissertation. I enjoyed working in the friendly collaborative atmosphere created by members of Dunham and Gamelin groups – I am thankful for thoughtful discussions, help, and support. A special word of gratitude goes to my committee members and collaborators at the Molecular Engineering Materials Center at the University of Washington. Exposure to interdisciplinary projects helped me gain insights from different perspectives and put my work in the broader context of materials research.

CHAPTER 1: INTRODUCTION

Semiconductor nanocrystals are promising materials for photovoltaics, photocatalysis, display technologies, energy storage, and biomedical applications (*1–8*). Unlike their bulk analogues, the band edge potential of nanocrystals is strongly dependent on factors such as size and surface chemistry of the material. Therefore, it is important to know band-edge potentials of these materials and understand how they can be rationally tuned in order to maximize device efficiency and control its behavior.

1.1 Semiconductor nanocrystals as versatile tunable materials

Nanomaterials, materials with a typical size of 1-100 nm, have been explored for a wide variety of applications. Group II-VI semiconductors and oxides are particularly interesting. Semiconductor nanocrystals (NCs) exhibit unique properties, which depend on chemical composition, size, and shape of the nanoparticles (*9–11*). In quantum dots (QDs) in particular, size effects due to quantum confinement yield tunability of the band gap and the position of the valence and the conduction bands. This tunability makes QDs promising materials for variety of applications (*12*, *13*). Unlike their bulk analogues, the band-edge potential of NCs is strongly dependent on surface chemistry of the material. Nanocrystals feature high surface-to-volume ratio (in contrast to bulk materials). As a result, perturbations to surface of nanocrystals play a major role in defining the fundamental properties of the material, thus opening an opportunity to use surface chemistry for tuning of nanocrystal properties for specific

applications (*14–20*). However, the effect of surface chemistry on the band-edge potentials of colloidal NCs has not yet been fully studied. Therefore, it is important to determine (experimentally and through modeling) what governs the band-edge potential shifts of colloidal nanomaterials and what role surface chemistry, NC composition, and size play in this process.

1.2 Band engineering in semiconductor nanocrystals

Nanomaterial applications benefit from tunability of these materials. Surface chemistry control, such as redox potential tuning (changes in surface dipoles via ligands, ionic impurities) and electronic doping (electron transfer, photodoping, defect doping) as well as size, shape, and chemical composition control are methods for tuning nanomaterial performance (*21*).

Band positions of many promising materials are reported in literature (*22*). Band edge potentials of the complex systems are not always accurately described by individual band edge potentials of components (*23–25*). Electric field generated at the system interface may shift band positions (*23*). The nature of solution the system is in and nanocrystal capping ligands affect the energetic characteristics of the system (*24, 26, 27*). Effects of reorganization energy play a significant role in complex nanocrystal systems, however there is still a lot to learn about what exactly these effects are and how to tune them (*25*).

In quantum confined semiconductor nanocrystals (quantum dots), band gap engineering can be readily achieved via altering the nanocrystal size. As in bulk semiconductors, valence band and conduction band are separated by a band gap. Electrons in the ground state are typically confined to the valence band but can be promoted to the conduction band if sufficient energy (greater than the band gap) is provided, for example in the form of a photon. The size of band gap is generally defined by the chemical composition. However, in quantum dots, physical dimensions smaller than the exciton Bohr radius impose quantum confinement on charge

carriers. Smaller quantum dots experience greater degree of confinement and feature larger band gap in comparison to larger quantum dots of the same chemical composition. As physical size of nanocrystals can be controlled via synthetic procedure parameters (*28–32*), band gap can be precisely defined and tuned.

Nanocrystal electronic properties can also be tuned through non-stoichiometry. Addition of ionic impurities allows to shift band energies (*33*).

Surface chemistry plays a major role in defining nanocrystal properties, in part due to high surface-to-volume ratio in nanomaterials. As a result, surface chemistry perturbations allow to tune structures of nanoparticles, thus tuning their properties (*34–36*). Nanocrystal band edge potentials can be shifted by up to 0.5 V through changes in surface ion stoichiometry and electrolyte concentration (*26*). Altering nanocrystal ligand passivation, in particular, allows to tune dipole moments (sum of ligand and interface dipoles) due to changes in surface binding. Withdrawal of electrons from nanocrystals by ligand molecules stabilizes nanoparticles, lowering NC band energies (*37*).

1.3 Electronic doping in semiconductor nanocrystals

Electronic doping of semiconductor nanocrystals is a key strategy for application of these highly tunable materials in semiconductor electronics. It has previously been demonstrated that photodoping, electron transfer and defect doping are successful methods for doping NCs with electrons. Unlike chemical/photochemical reduction, defect doping results in very stable (not oxidized by air) n-doped or p-doped NCs (*21*). The appearance and stability of excess free carriers depends on availability of charge-carrier reservoirs such as solvated redox active species (surface traps, electrolyte ions, sacrificial reductants) that compensate doped electrons.

During electronic doping the Fermi level of NCs is shifted from the middle of the bandgap (intrinsic semiconductors) beyond the conduction band edge (electronically doped NCs) and delocalized charge carriers are introduced. Excess electrons generate two absorption features: a bleached interband band-edge absorption and an infrared (IR) intraband absorption. Accumulation of large electron densities results in localized surface plasmon resonances (LSPRs). Presence of extra electrons in the conduction band of NCs is confirmed by electron paramagnetic resonance (EPR), shortening of photoluminescence (PL) decay times and decrease in luminescence quantum yields. Electronically doped NCs show a change in chemical potential of the system with a change in the number of excess electrons, making potentiometry a suitable technique to track electronic doping. Tunability of chemical potential via electronic doping is a powerful tool for making the performance of NCs in electronic devices better via band engineering (*21*).

1.4 Summary and dissertation overview

Semiconductor nanocrystals feature unique properties due to quantum confinement of charge carriers (in case of quantum dots), large surface-to-volume ratio, and sensitivity of electronic properties to nanocrystal chemical composition, shape, size, and surface interactions. All of these enable tunability of the band gap and the position of valence and conduction bands. Tunability of electronic properties makes semiconductor NCs promising materials for band engineering.

In this work we employ experimental and computational approaches to study electronic structures of colloidal Cu:ZnSe, PbS, CdS, CdSe, ZnO nanocrystals and explore strategies for tuning of electronic properties of those materials. Phenomena that govern band-edge potential

shifts of colloidal nanomaterials are probed and the role of surface chemistry, nanocrystal composition, size, and shape are discussed.

Chapters 1-3 provide a general introduction into the subject of our investigation – colloidal semiconductor nanocrystals with excess charge carriers – and describe key experimental (Chapter 2) and computational (Chapter 3) tools used in this study.

Chapter 4 delves into synthesis and characterization of common group II-VI semiconductor nanoparticles – Cu-doped ZnSe, PbS, CdS. Tunability of electronic structures in these compounds is demonstrated via defect doping (in case of Cu:ZnSe) or alterations of surface chemistry (in case of PbS and CdS).

Chapter 5 describes electronic doping of ZnO nanocrystals and highlights the emergence of supercapacitance in ZnO under certain conditions. Specifically, we show that capacitance can be increased via Al doping, interactions with Li^+, and shape/media changes. We attribute these effects to electrostatic interactions on the nanocrystal surface and within the tunneled ZnO crystal structure.

Chapter 6 explores a unique electron transfer system – mixture of colloidal CdS and ZnO nanocrystals – where both participants of electron transfer are electronically doped at the same time. Selective photodoping of CdS NCs leads to initial accumulation of electrons on CdS followed by sustained electron transfer to ZnO NCs. Yet, even this behavior is surprising, as relative band edge potentials of individual CdS and ZnO NCs are unfavorable for CdS-to-ZnO electron transfer. We propose a hypothesis that ligand composition on CdS NCs changes upon mixing with ZnO NCs, leading to shift in CdS potential.

Chapter 7 presents a computational framework for investigation of nanocrystal-ligand interactions. Our model predicts band edge potential shifts in CdS NCs consistent with

experimentally observed trends. We explore in greater detail the effects of different ligands on NC structure and electronic properties and show that ligand-induced changes in total dipole play a major role in defining NC behavior.

Chapter 8 highlights several emerging applications of our computational framework. Pilot results predict ligand-induced changes in electronic properties in CdSe NCs (in line with CdS work presented in this dissertation). The library of ligands is expanded to include inorganic ligands, which yield further stabilization of band edge potential. Further, this approach is applied to structurally different systems, such as diamond, multiple compositions/structures in Fe-Cu-S family, and elpasolite nanocrystals.

Chapter 9 summarizes key findings and achievements of this work and presents an outlook for future research.

CHAPTER 2: SPECTROELECTROCHEMISTRY (specEchem) AS A METHOD TO STUDY ELECTRONIC PROPERTIES OF COLLOIDAL NANOCRYSTALS

Chapter 1 has introduced the importance of nanocrystal electronic properties. Here, we delve into the main methodology we used to characterize electronic properties of colloidal nanocrystals – spectroelectrochemistry, or specEchem.

2.1 Methods for characterization of electronic properties of semiconductors

Many applications involve exchange of electrons, and, thus, it is critical to know the redox properties of nanocrystal materials in order to maximize device efficiency (*38*). Redox properties of nanomaterials are determined by band edge potentials. Electronic doping deposits electrons in the conduction band of NCs and thus changes chemical potentials in the system. Potentials can be evaluated using such techniques as scanning tunneling spectroscopy (*39*),(*40*) and photoelectron spectroscopy (*41*), but these methods require sophisticated sample treatment. Moreover, sample preparation might affect potential values. Cyclic voltammetry (CV) is commonly used for this purpose (*42*, *43*). There are several drawbacks that limit the use of CV, including irreversibility, difficulty of analysis of peaks associated with NCs, possibility of sample decomposition during the CV experiment, and the lack of a quantitative optical handle. Sometimes, CV measurements are performed on NCs immobilized on electrodes, but in this case the surface chemistry of NCs is altered, and this might affect the potential values.

In this dissertation, we use spectroelectrochemical potentiometry (specEchem) (*44*) to measure band edge potentials of colloidal NCs and investigate the influence of dynamic surface chemistry. SpecEchem is a contactless method for measuring the open-circuit potential of colloidal NCs in electrolyte, making it a technique of choice for understanding RedOx properties of colloidal NCs (*43, 45*). Compared to CV, specEchem has several advantages: the measurement is non-destructive, redox processes are reversible, and there is optical sample control. Furthermore, this measurement gives insight into the redox properties of NCs in the colloid, where applications such as photocatalysis, bio-labeling, and excited state dynamics are more relevant.

2.2 Description of specEchem setup used in this dissertation

During typical specEchem experiment (**Figure 2.1**) NCs are dissolved in $TBAPF_6$/THF mixture and placed in a 4 ml cuvette with a stir bar in the N_2 atmosphere inside the glovebox. Three electrodes (Ag/AgCl reference, Pt working and Pt counter), connected to the potentiostat (Gamry) outside the glovebox through coaxial cables, are inserted through the rubber cuvette cap, and cuvette holder is coupled to the spectrophotometer (Agilent Cary 5000 UV-Vis-NIR) through fiberoptic cables to ensure that spectroscopy can be done at the same time with potentiometry. Potentiostat is set up in galvanostatic mode to measure the Fermi level of the solution. Hole quencher (EtOH or $LiEt_3BH$) is added to the NC solution and the LED is turned on to start photodoping. Completeness of the photodoping is determined based on lack of change in absorption. As soon as photodoping is done, equivalents of $FcBF_4$ are added to titrate excess electrons from the conduction band of nanocrystal. The change in open circuit potential of the nanocrystal solution is measured at the same time as changes in absorption. This change in potential is plotted vs equivalents of $FcBF_4$. Cyclic voltammetry was conducted on ferrocene dissolved in the solution used for potentiometry. CV diagram was analyzed (potentials of the

peak current of reduction and oxidation reactions were averaged) in order to reference the potential measured during potentiometry to a $Fc^{0/+}$ potential.

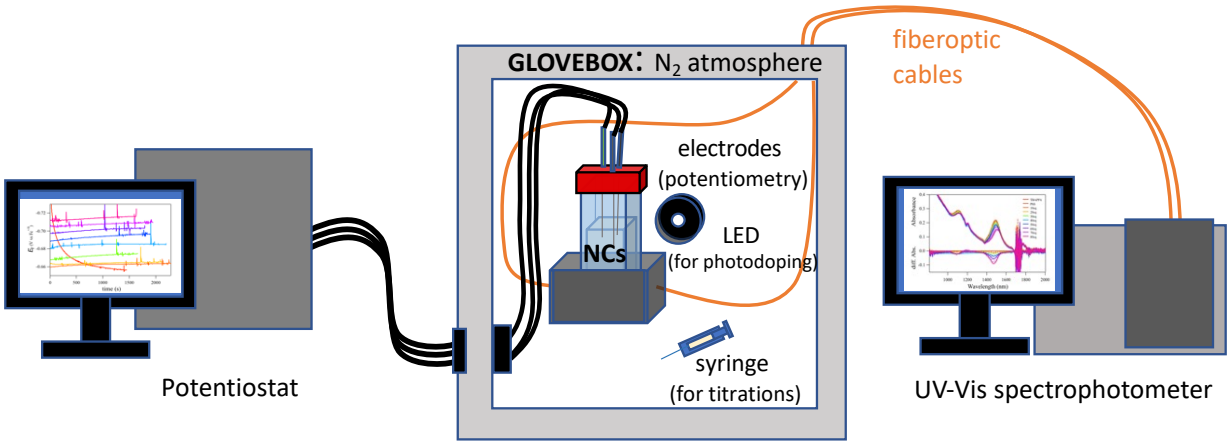

Figure 2.1 SpecEchem setup. Experimental setup consisted of a sample cuvette positioned inside a glovebox with N_2 atmosphere and connected to a UV-Vis spectrophotometer for an optical read-out of sample absorbance as well as potentiostat for the measurement of an open circuit potential.

2.3 Optimization of specEchem for colloidal nanocrystals

Gamry potentiostats are widely used in electrochemistry, however most of the systems studied are in water-based solutions, so the specifics of working in organic solvents are not always reported. It was important to adapt the instrument for organic solvent, specifically to determine the measurement error for our system. Typically, there are two types of errors: potentiostat performance errors and cell performance errors. First the instrument performance checks were conducted to make sure the potentiostat behaves as expected (**Figure 2.2**). The instrument test results were consistent with reference manuals, so the cell performance was tested next.

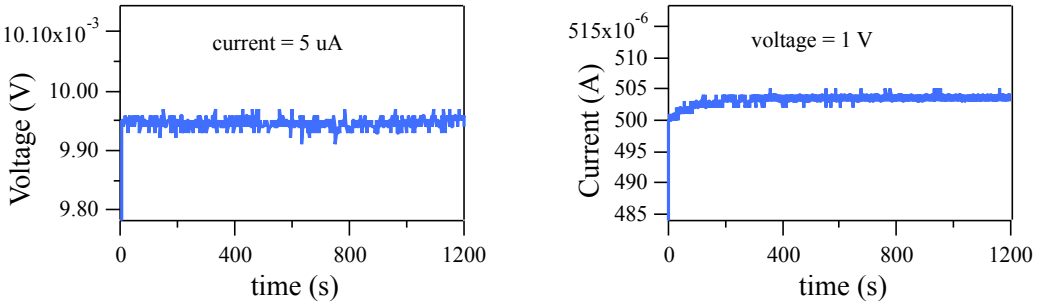

Figure 2.2 Gamry potentiostat instrument performance check. Voltage and current stability are measured over time.

Potentiometry of electronically doped nanocrystals in organic solutions can be challenging for several reasons. First of all, the setup has to be airfree, because contact of nanocrystals with air results in oxidation and loss of excess electrons. To fulfill this requirement potentiostat was connected to the glovebox, where the measurement was conducted. Secondly, the setup for the electrochemical cell consisted of 4ml cuvette with 3 microelectrodes (reference Ag/AgCl, working – platinum wire, and counter – also platinum wire). Microelectrodes are custom made and resistivity of the reference electrode has to be tested before each experiment, to confirm the electrode is working properly. Once the potentiostat and the cell performed as expected the measurement error was calculated as a difference of $E_{1/2}$ for the same reference compound before and after the experiment (**Figure 2.3**). Potential drift in organic solvent was measured to be <20mV.

Different organic solvent mixtures were tested to minimize the potential drift error, while keeping nanocrystals colloidally stable. $CHCl_3$ was showing smaller potential drift error than THF, but the properties of nanocrystals seemed to be affected (**Figure 2.4**). Larger nanocrystals are known to have lower band edge potential values than smaller ones, however in $CHCl_3$ the trend is reversed, indicating possible side surface chemistry reactions, resulting in band edge potentials of larger nanocrystals becoming higher.

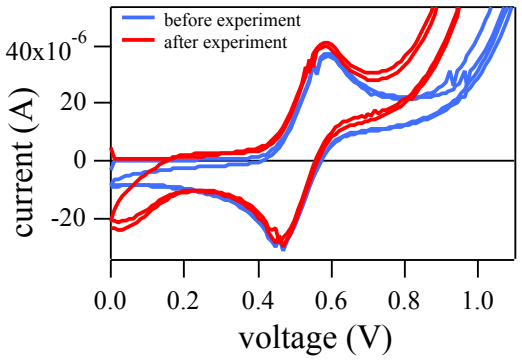

Figure 2.3 Measuring the performance error of the potentiostat in organic solvent. Minimal potential drift error was observed.

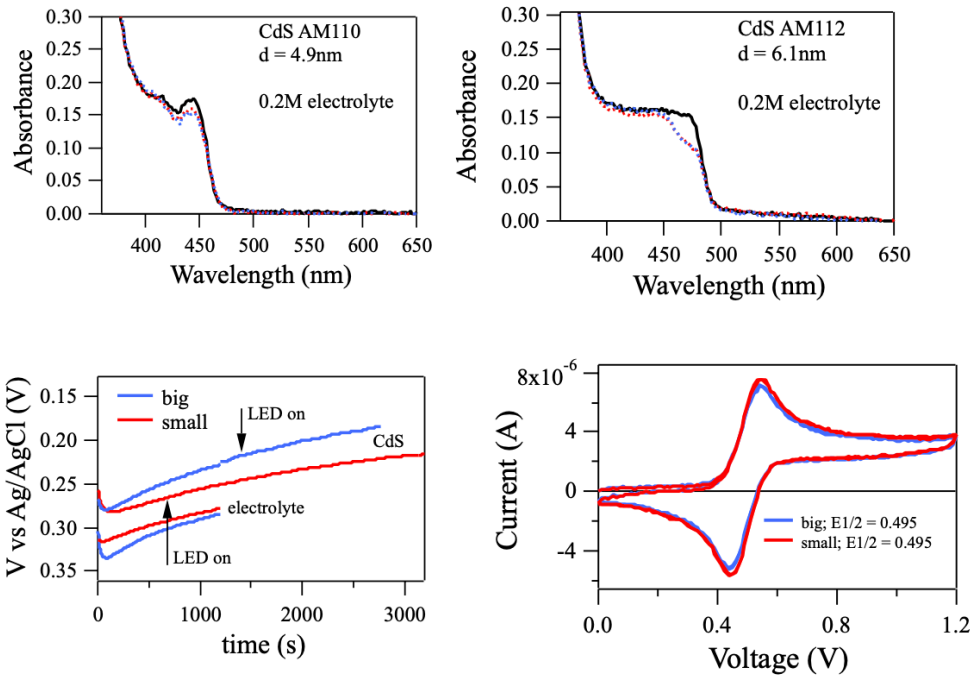

Figure 2.4 Potential drift and band edge potential trends in $CHCl_3$. Potential drift is smaller, but band edge potential trends are reversed.

Electronically doped nanocrystals are prepared using hole quenchers – molecules that react with excitons. EtOH and $LiEt_3BH$ are most commonly used, however little is known about the side reactions these molecules participate in. Here we show that – all things equal except the hole quencher – specEchem shows different results, suggesting that $LiEt_3BH$ not only stabilizes excess charges, but participates in other processes effecting nanocrystal energetics (**Figure 2.5**).

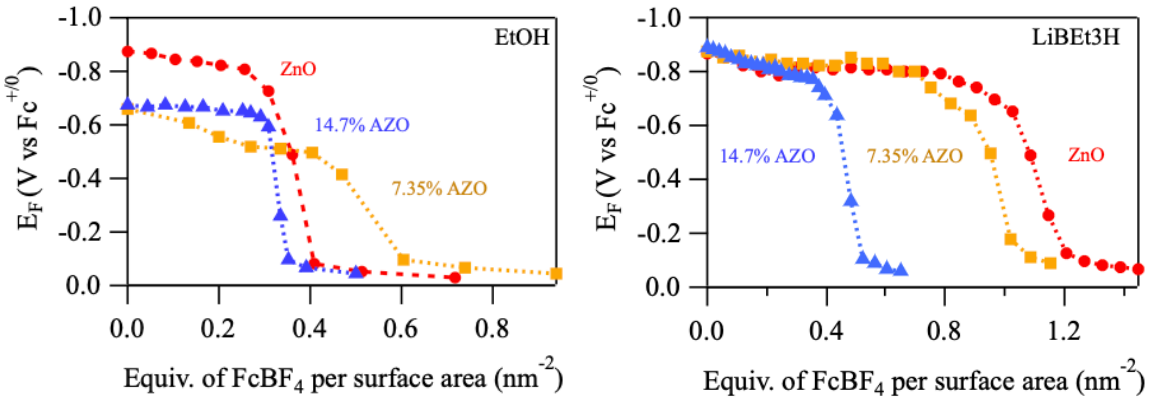

Figure 2.5 SpecEchem with $LiEt_3BH$. Common hole quencher employed for electron doping also affects nanocrystal energetics. Measurements were performed on ZnO and Al-doped ZnO NCs (described in more detail in Chapter 5).

2.4 Summary

Compared to other techniques that are used to study redox properties of semiconductor materials, SpecEchem is uniquely suited for the characterization of electronic properties of colloidal nanocrystals in various environments. For characterization of colloidal NCs in organic solvents under inert atmosphere, we made a setup consisting of an electrochemical cell placed withing a glove box and connected to potentiostat and spectrophotometer. We have optimized all components of specEchem for our samples to minimize measurement errors due to side reactions and effects of supporting media in the electrochemical cell. We have established

conditions under which potentiostat has smallest instrument error, while electrochemical cell exhibits the least side reactions. We have also determined that $LiEt_3BH$ (superhydride), commonly used as a hole quencher, may affect electronic properties of measured NCs, necessitating the use of ethanol as a hole quencher instead.

CHAPTER 3: COMPUTATIONAL METHODS FOR THE STUDY OF ELECTRONIC PROPERTIES

Computational approaches provide a complementary set of tools for the study of electronic properties (*46–54*), offering mechanistic insights into the behavior of nanocrystal-ligand systems and alternative angles at characterization of materials, particularly when experimental methods might not be feasible or practical to apply.

Computational methods to calculate electronic structure include tight-binding, Hartree-Fock, DFT (*55*). DFT is commonly used to describe periodic systems as well as molecules absorbed on the surfaces of the solids (*37*, *56–58*). Success of DFT originates in simple yet accurate local density approximation (LDA) and generalized gradient approximation (GGA) approaches. Different basis sets can be used – atomic orbitals basis (Gaussian software package, for example) and plane wave basis (VASP software package, for example). Generally, plane waves offer a more universal solution (*59*). Hence, we used VASP for computational investigation of nanocrystal systems in this dissertation.

3.1 Using VASP for DFT calculations

Total free energies of nanocrystal slabs and ligand molecules, ligand-nanocrystal binding energies, potentials and densities of states were calculated using the VASP simulation package with Projector-Augmented-Wave (PAW) Perdew-Burke-Ernzerhof (PBE) generalized gradient approximation (GGA) functional (*55*, *60*). Cutoff energy for the plane wave basis set were

chosen based on the biggest cutoff energy of the atomic species found in pseudopotential files and was kept constant for all calculations. Gamma centered $5 \times 5 \times 3$ k-point mesh was chosen as Bloch vectors due to hexagonal Bravais lattice. Ratios between the subdivisions were manually chosen to be inversely proportional to slab cell vectors to make sure that the lattice vectors do not affect the k-point mesh.

3.2 Geometry optimization: molecular dynamics and local optimization

To find the lowest total free energy of the system, global and local geometry optimization was performed. Global energy optimization was done through simulated annealing (molecular dynamics), when the starting geometry was heated through coupling to Nose-Hover thermostat under different conditions, such as temperatures, thermostat coupling parameters, and time (*61*, *62*). Starting from different configurations under various conditions allowed to overcome local energy minima and reach the optimal geometry of the structure. Once the lowest energy configuration was found, the atom positions from the XDATCAR file were used as a starting configuration for local optimization (at 0 K).

3.3 Density of states, potentials, and wavefunction analysis

Planar average potential data allows to evaluate band edge positions relative to vacuum. Dipole correction was applied to account for total dipole coming from mismatch of atomic charges. Python script was used to find average values for slab and vacuum regions to align data. Differences between vacuum regions and slab vacuum regions were then compared for each system to determine the potential offsets.

Density of states (DOS) analysis allowed to compare charge density distribution between valence band and conduction band for different conditions (such as surface ligands). The simplified (rotationally invariant) approach to DFT+U correction, introduced by Dudarev et al (*63*), was applied to cadmium d orbitals to open the band gap. Effective on-site Coulomb interaction was initially set to 4.5 eV as suggested in literature for wurtzite CdS (*64*) and gradually increased to 8 eV until the calculated band gap value was closest to experimental value. Total DOS and partial DOS (top Cd and S atoms) were measured to evaluate binding nature between slab and ligand.

Wavefunction analysis was done by plotting Bloch wavefunctions forming CB and VB found in EIGENVAL files. This allowed to visualize charge distribution at the slab/ligand interface.

3.4 Data post-processing and visualization

DOSCAR and LOCPOT data was visualized using QuantumATK package (*65*) and plotted with Python3 [https://www.python.org] using pandas, scipy, and matplotlib libraries.

Distribution of charge density allowed to evaluate interfacial and ligand dipoles. Charge density data was obtained from CHGCAR grid files through vaspkit (*66*). Core electrons were simulated using Gaussian functions. Electron and core charge densities were integrated to obtain total charge distributions for dipole moment analysis.

Slab-ligand configurations were visualized using VESTA (*67*) and DIAMOND [https://www.crystalimpact.de/diamond] packages.

Molecular dynamics results were visualized and analyzed using py4vasp [https://www.vasp.at/py4vasp/latest], OVITO (*68*) packages.

3.5 Summary

Various computational methods exist to explore, characterize, and predict electronic properties of materials. By performing geometry optimization and analysis of resulting structures (potentials, DOS, and dipoles) we have developed a computational framework for investigation of colloidal nanocrystal-ligand systems based on DFT modeling and supporting tools for data analysis (**Figure 3.1**).

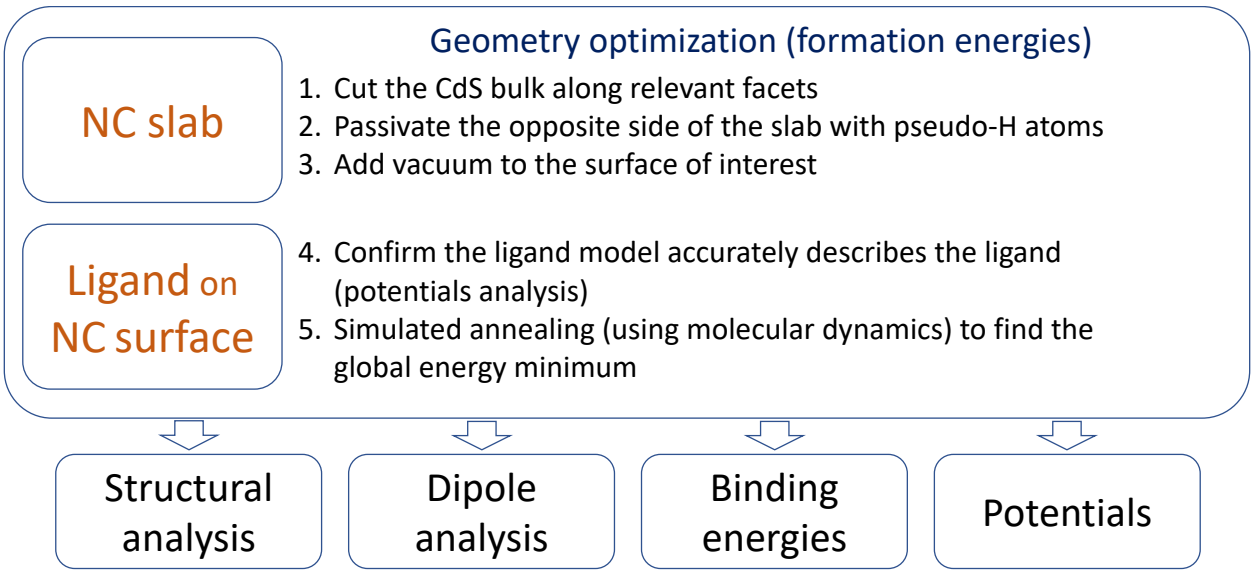

Figure 3.1 Computational framework for modeling of nanocrystal-ligand interfaces.

CHAPTER 4: PREPARATION AND CHARACTERIZATION OF NANOCRYSTALS WITH TUNABLE ELECTRONIC PROPERTIES

Chapter 4 describes preparation and characterization of various group II-VI colloidal semiconductor nanocrystals and strategies for tuning of their electronic properties. Specifically, Cu-doped ZnSe, PbS, and CdS materials are discussed.

4.1 Nanoparticle characterization methods

Spectroscopy. Absorption spectra were taken with an Agilent Cary 60 or Agilent Cary 5000 UV-Vis-NIR spectrophotometer.

TEM. NC TEM images were obtained using a FEI TECNAI F20 microscope operating at 200 kV. Samples for TEM were prepared by dropcasting NC suspensions onto carbon-coated copper grids from TED Pella, Inc. Reported NC sizes reflect measurement of 100 individual nanocrystals in each case.

ICP. Elemental composition was determined by inductively coupled plasma – atomic emission spectroscopy (ICP-AES, PerkinElmer 8300). Samples were prepared by digesting the NCs in concentrated nitric acid overnight with sonication.

XRD. X-ray diffractograms were collected on a Brucker D8 Discover and analyzed using EVA software. Samples were prepared by dropcasting nanocrystals on silicon wafer.

4.2 Preparation of Cu-doped ZnSe nanocrystals

Cu-doped ZnSe nanocrystals have promising electronic properties (*69*). There have been several reports on synthesis of these nanocrystals, however systematic study of ZnSe synthesis and Cu-doping is required to fully understand how to use band engineering to tune properties of this material to reach high levels of Cu-doping (*70–74*).

High quality ZnSe cores of different sizes were synthesized for future growth-doping with Cu by modifying existing strategies (*71*, *72*) (**Figure 4.1**). $Zn(stearate)_2$ (0.1 mmol, 0.0632 g) in 5 mL ODE and 0.25g ODA was heated up to 270°C under N_2 flow, and 1 mL of degassed mixture of Se (0.1895 g) dissolved in 0.5 ml TBP (2.4 mol/L) (TBPSe) was injected into the $Zn(stearate)_2$ solution. NCs are left to grow at least for 10-15 minutes (the reaction mixture became yellow after 5 minutes) then the reaction mixture was cooled to 190°C. At 190°C Cu-doping solution (CuI(17.3 mg)-ODE(2.5g)-TBP(0.3ml)) was injected. NCs were spun down as prepared for 20 minutes, dissolved in toluene and OA and MeOH, and stored in toluene.

For Cu-doping (**Figure 4.2**): After cooling the ZnSe reaction mixture to 190°C, Cu-doping solution (CuI(17.3 mg)-ODE(2.5g)-TBP(0.3ml)) was injected. NCs were spun down as prepared for 20 minutes, dissolved in toluene and OA and MeOH, and stored in toluene.

Synthetic procedure was optimized by reducing Cu concentration, changing Cu precursor, changing ligand from TOP to TBP, and reducing doping temperature to 190° C compared to procedure reported in literature (*71*, *72*). Even though optimized synthetic procedure (**Figure 4.3**) resulted in high-quality Cu:ZnSe nanoparticles (with no need to shell), those materials were not stable (scattering) and degraded over time (several days), probably due to Cu out diffusion.

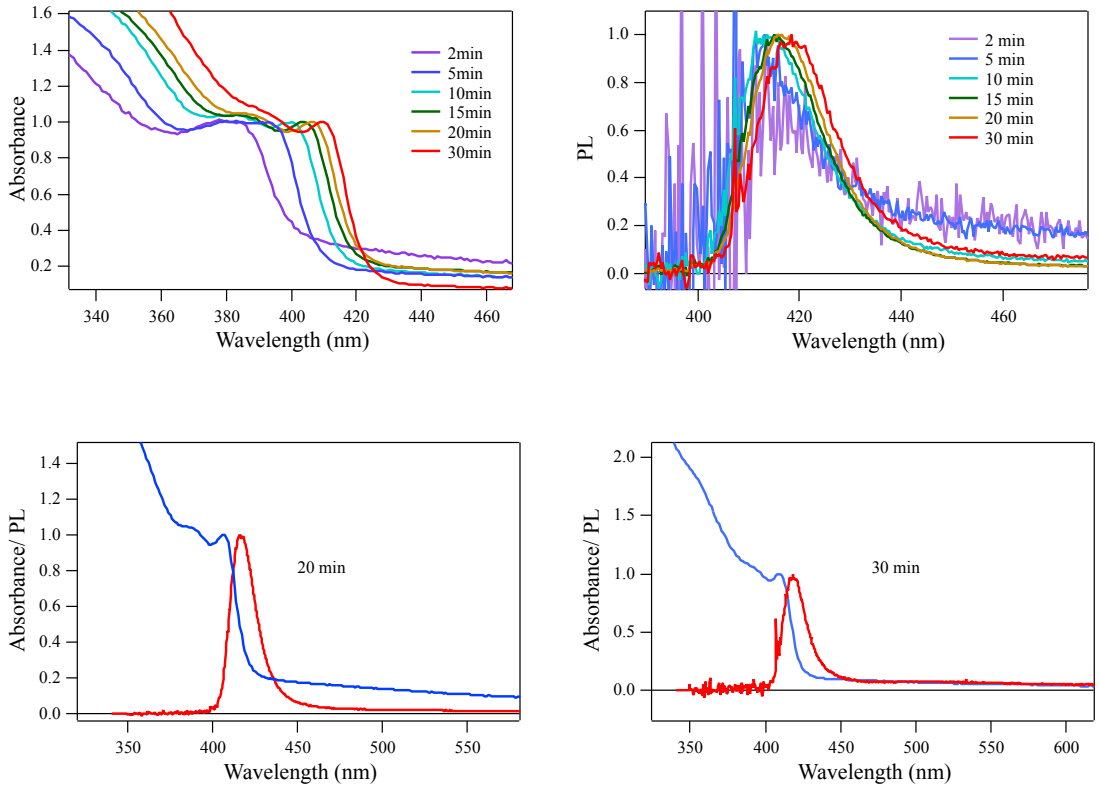

Figure 4.1 Characterization of ZnSe nanocrystals. Absorbance and fluorescence of ZnSe NCs were measured at different times during synthesis.

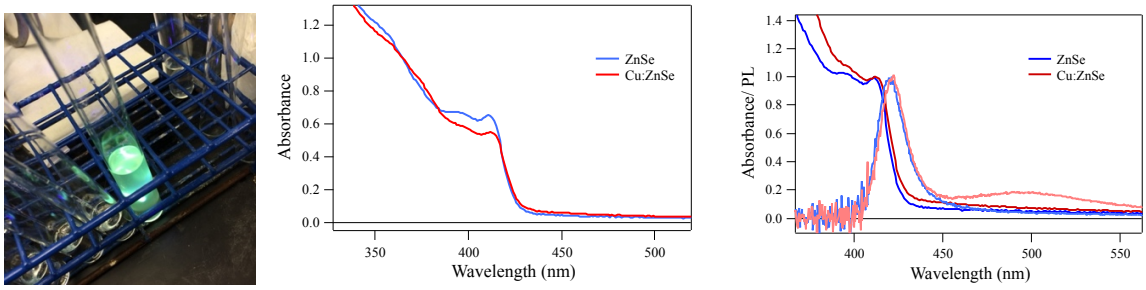

Figure 4.2 Characterization of Cu-doped ZnSe nanocrystals. Colloidal nanocrystals with blue-green fluorescence were obtained. Absorbance and fluorescence were measured to confirm Cu doping.

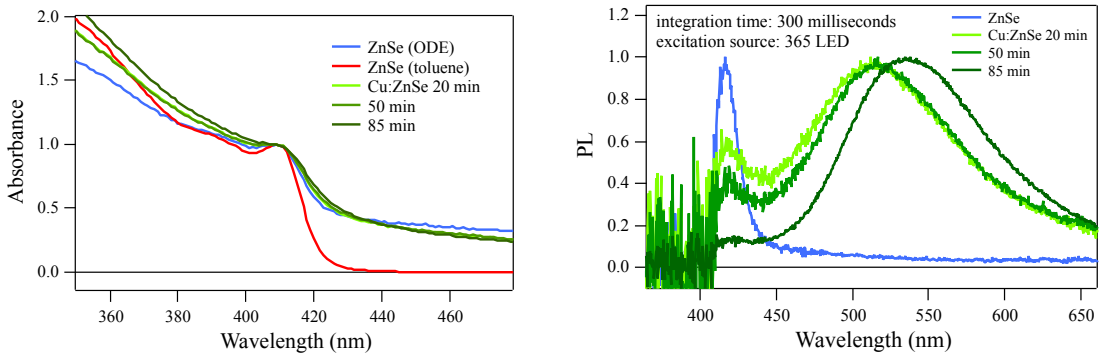

Figure 4.3 Procedure optimization for improved Cu doping. An increase in Cu content was achieved as measured by increase in photoluminescence at 550 nm.

4.3 Preparation of PbS nanocrystals

PbS QDs were synthesized using known procedure (*75*). In brief, mixture of $PbCl_2$ and oleylamine is degassed and heated in a three-neck flask to 120°C under N_2. After that the mixture of S in oleylamine is swiftly injected. QDs are grown for 2 minutes. After that heating is immediately removed and particles are dissolved in hexane. Oleic acid is added dropwise to the NCs solution and then particles are washed with EtOH. Diameter of particles (5.7 nm) was determined based on energy of the first excitonic feature (*76*).

Absorption spectrum of PbS QDs agrees well with previous reports (**Figure 4.4**). After washing, the NCs are dried under N_2 and brought inside the glovebox, where they are dissolved in tetrahydrofuran (THF), filtered, and stored. NCs are stable for several months.

Data for a typical specEchem experiment is shown in **Figure 4.5**. Briefly, the experiment is performed in an optical cuvette inside an N_2 glovebox. A standard three-electrode setup is employed, with two platinum wires serving as the working and counter electrodes, and a 1 mm leakless Ag/AgCl reference electrode. Cobaltocene is used as a chemical agent (in RedOx reaction) for electronic doping of PbS NCs (*77*). Known amount of cobaltocene is added to NCs

in electrolyte solution. The progress in electronic doping is monitored via change in first excitonic feature of PbS QDs.

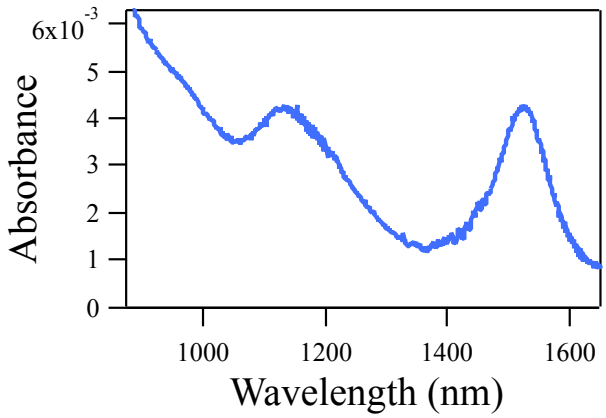

Figure 4.4 Electronic absorption spectrum of as-prepared PbS NCs (d = 5.7 nm) in tetrachloroethylene. Excitonic transitions are well-resolved. Data is in agreement with literature (*75*).

As equivalents of Cp_2Co are added to the solution, the first excitonic feature of the QDs bleaches (**Figure 4.5**a), consistent with addition of electrons to the CB. This bleach provides a quantitative handle on the average number of electrons per QD ($\langle n \rangle$). Concurrent with excitonic bleach, the potential of the solution becomes more negative (**Figure 4.5**b), consistent with the Fermi level of the solution moving into the conduction band. We define the band-edge potential as the potential of the solution when $\langle n \rangle = 1$ (*44*). Our redox potentials are referenced to the well-known $Fc^{+/0}$ redox couple by adding a small amount of ferrocene at the end of the experiment and performing cyclic voltammetry (**Figure 4.5**c). **Figure 4.5**d plots the solution potential vs $\langle n \rangle$. From these data, we can extract a band-edge potential of – 0.68 V vs $Fc^{+/0}$. This value is more negative than the CB potential (-0.61V vs $Fc^{+/0}$) measured by photoelectron spectroscopy of PbS NCs of the same size as in our work (*78*). Both of these values are more negative than what is predicted from bulk (- 0.54V vs $Fc^{+/0}$) (*79*). This is probably due to the different surface chemistry in each of those cases: our sample is passivated with oleic acid and

Cl- ions, in literature oleic acid is the only capping ligand and in bulk materials surface chemistry does not affect the system.

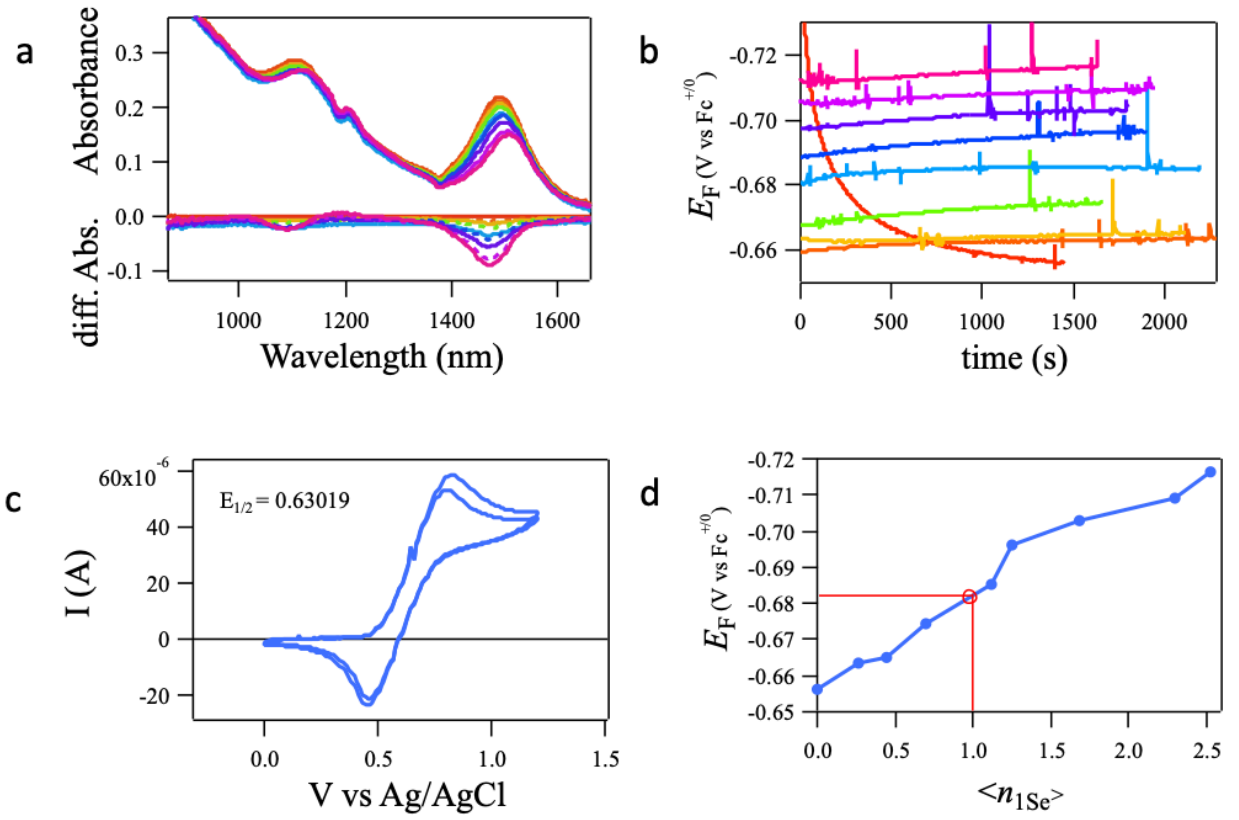

Figure 4.5 **Spectroelectrochemical potentiometry of PbS NCs.** (a) Top: electronic absorption spectra of as-prepared (red), fully electronically doped (pink) and intermediate cases (orange – purple) PbS NCs (d = 5.7 nm). Experiments were performed using TBAPF6 solution of PbS NCs. Electronic doping was conducted by adding equivalents of chemical agent – Cp_2Co. Bottom: differential absorption (b) Open-circuit potential of as-prepared (red), fully electronically doped (pink) and intermediate cases (orange – purple) PbS NCs. Potential was measured simultaneously with absorption. (c) CV of ferrocene in PbS NCs solution after potentiometry to reference the potentials shown in (b). (d) Potentials shown in (b) are plotted vs average number of electrons calculated from (a) using 8(A – A0)/A0, where A0 is absorption of as-prepared PbS NCs (red trace in (a)).

It has been shown in films that the band-edge potentials of PbS NCs are strongly dependent on capping ligands, with a significant difference in potentials being observed between Cl – and benzenethiol capped particles. Therefore, we decided to investigate whether it will remain true for colloidal NCs. To study this, we conducted ligand exchange of as-synthesized PbS QDs. As-synthesized PbS NCs are capped with oleic acid and Cl – ions. We attempted to change these ligands with benzenethiol. The procedure for ligand exchange was adapted from literature (*80*). In brief, slight excess of ArS^- / $TEA\text{-}H^+$, where Ar is benzene, is added to PbS QDs in DCM. As a result of ligand exchange treatment, particles retain stability and show minimal changes in optical properties (**Figure 4.6**).

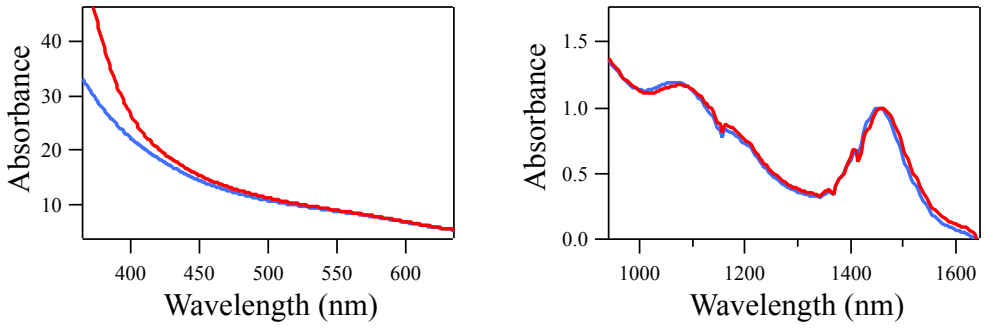

Figure 4.6 Ligand exchange of as-synthesized PbS NCs. Electronic absorption spectra of as-prepared (red) PbS NCs and PbS NCs after ligand exchange procedure (blue). Experiments were performed using benzenethiol solution.

SpecEchem measurements of PbS NCs after ligand exchange show that the band-edge potential is – 0.92 V vs Fc+/0 (**Figure 4.7**). These data suggest that band-edge potentials of PbS QDs can be tuned by hundreds of mVs with simple ligand exchange treatments. However, the role of capping ligands in change of band-edge potentials of QDs remains yet unclear. Furthermore, the influence of synthetic procedure on potential values is not known.

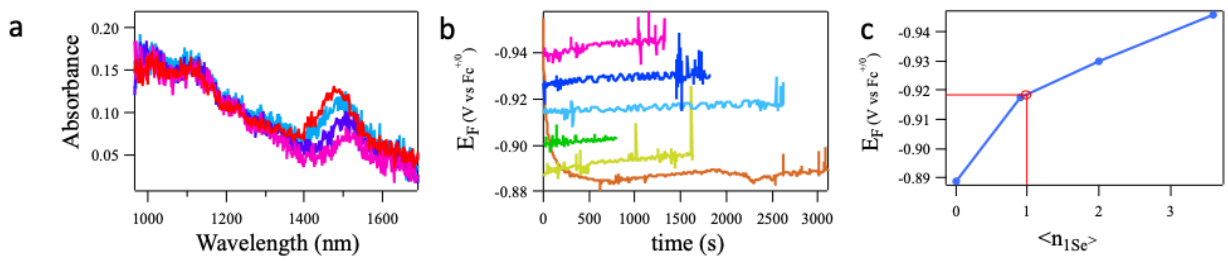

Figure 4.7 Spectroelectrochemical potentiometry of PbS NCs after ligand exchange. (a) electronic absorption spectra of as-prepared (red), fully electronically doped (pink) and intermediate cases (blue and purple) PbS NCs (d = 5.7 nm). Experiments were performed using 0.1M $TBAPF_6$ solution of PbS NCs. Electronic doping was conducted by adding equivalents of chemical agent – Cp_2Co. (b) Open-circuit potential of as-prepared (red), fully electronically doped (pink) and intermediate cases (yellow – blue) PbS NCs. Potential was measured simultaneously with absorption. (c) Potentials shown in (b) are plotted vs average number of electrons calculated from (a) using 8(A – A0)/A0, where A0 is absorption of as-prepared PbS NCs (red trace in (a)).

4.4 Preparation of CdS nanocrystals

CdS NCs is a well-known QD system commonly used for shelling (*81–83*), however CdS can be used as a stand-alone nanoparticle for various electronic applications. QDs were synthesized using known procedure (*84*). In brief, mixture of CdO, OA and ODE is heated to 300°C, TOP is added. After that the mixture of S in ODE is swiftly injected. Reaction should be quenched immediately after injection. Particles were washed with methanol and ethanol/acetone mixture. Diameter of particles (5.8 nm) was determined based on energy of the first excitonic feature (*85*). Absorption spectrum of CdS NCs is presented in **Figure 4.8**. After washing, particles are dried under N_2 and brought inside the glovebox, where they are dissolved in THF and stored. NCs are stable for several months.

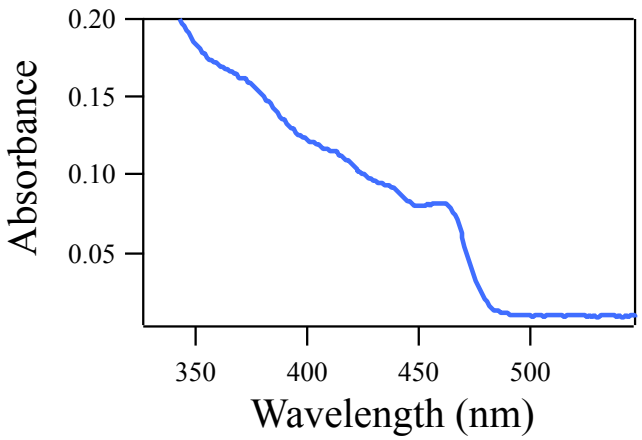

Figure 4.8 Electronic absorption spectrum of as-prepared CdS NCs (d = 5.7 nm) in hexane. First exciton peak position is at 461 nm. Excitonic transitions are well-resolved. Data is in agreement with literature (*84*).

Spectroelectrochemical potentiometry for CdSe NCs has been reported previously (*44*). Super hydride is used as a chemical agent (hole quencher) for electronic doping of CdS NCs (*86*). Known amount of super hydride is added to CdS NCs in electrolyte solution. Then CdS sample is excited with an LED for several minutes to provide an exciton for the hole quencher. The progress in electronic doping is monitored via change in the first excitonic feature of CdS QDs. The band-edge potential is – 1.48 V vs $Fc^{+/0}$. From bulk band-edge potentials (*87*) we expected band-edge potential of CdS to be more negative than that of CdSe (– 1.48 V vs $Fc^{+/0}$). However, we conducted spectroelectrochemical potentiometry of our CdS sample and obtained a more positive band-edge potential of – 1.1 V vs $Fc^{+/0}$ (**Figure 4.9**). Since the size effect in QDs is too small to result in such big difference, we hypothesize that either capping ligands or synthetic procedure affects the value of band-edge potential.

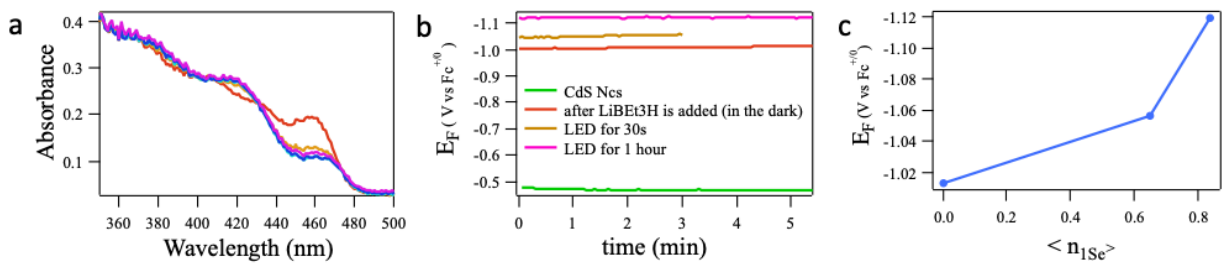

Figure 4.9 Spectroelectrochemical potentiometry of CdS NCs. (a) electronic absorption spectra of as-prepared (red), fully electronically doped (pink) and intermediate cases (yellow – blue) CdS NCs (d = 5.8 nm). Experiments were performed using TBAPF6 solution of CdS NCs, $LiEt_3BH$. Electronic doping was conducted by photodoping CdS NCs using $LiEt_3BH$ as a hole quencher. (b) Open-circuit potential of as-prepared (green), fully electronically doped (pink) and intermediate cases (yellow – red) PbS NCs. Potential was measured simultaneously with absorption. (c) Potentials shown in (b) are plotted vs average number of electrons calculated from (a) using 2(A – A0)/A0, where A0 is absorption of as-prepared CdS NCs (red trace in (a)).

4.5 Summary

Group II-VI semiconductor nanoparticles – Cu-doped ZnSe, PbS, and CdS – were synthesized and characterized. Tunability of electronic structures in these compounds was evaluated with specEchem. In Cu:ZnSe NPs, defect doping yields a Cu band within the NP electronic structure. In PbS and CdS NPs, alterations of surface chemistry result in substantial shifts in band edge potentials, highlighting the effect of nanocrystal surface interactions on electronic properties.

CHAPTER 5: SUPERCAPACITANCE IN ZnO-BASED NANOMATERIALS

Nowadays society is switching to clean energy sources. The lack of on-demand availability of these resources makes energy storage essential for the development of clean energy applications. Various nanomaterials have been explored for their high capacitance properties, including ZnO nanomaterials (nanorods)/composites. We demonstrate in this chapter that capacitance can be increased to supercapacitance levels using well-studied, non-toxic, and easily prepared ZnO nanocrystals as a starting material. Commonly used spherical ZnO nanocrystals have small capacitance. However, we show that ZnO-based nanocrystals prepared via 3 different methods show a dramatic increase in capacitance, exceeding the value of many materials that are currently considered state-of-the-art. Specifically, we show that high capacitance can be achieved in (1) non-spherical ZnO NCs; (2) ZnO NCs in presence of Li^+, and (3) ZnO nanocrystals doped with aluminum. Furthermore, we show that change in supporting media (electrolyte) also affects ZnO NC capacitance. These approaches and obtained materials might enable the development of inexpensive and "green" energy storage devices with supercapacitance properties.

5.1 Nanocrystal supercapacitors as energy storage materials

High densities of delocalized electrons in electronically doped NCs potentially enable use of these materials in energy storage. Wide range of emerging applications rely on portable energy storage and on-demand energy release – such as electric vehicles, clean energy,

consumer electronics, medical equipment, portable sensors, space rovers, etc. Batteries and electrochemical capacitors (ECs) have fulfilled this role for decades (*88*). Batteries have been studied extensively (*89*). Although ECs have attracted less attention, for higher power delivery applications, these materials can complement or even replace batteries (*90*).

The biggest challenge to broaden the range of applications for ECs is to increase energy density. Since the storable energy is proportional to capacitance and increases with the square of the voltage attainable upon charge, this goal can be achieved by increasing both the specific capacitance and overall cell voltage. Cell voltage increases when aqueous solvent is substituted by nonaqueous, and specific capacitance can be increased by nanostructuring. Nanomaterials improve characteristics of energy storage materials due to high surface/volume ratio and shortening of diffusion length (*88*, *90*, *91*). Ensemble NC capacitance is governed by classical surface electrical double layers (EDLs) and can be directly measured by potentiometric titrations (*44*). Nanocrystals (NCs) of different composition, for example $RuO_2 \times nH_2O$, MnO_2, Fe_3O_4, V_2O_5, Fe:ZnO, and morphologies, such as quantum dots (0D), nanowires (1D), nanosheets (2D) and nanonetworks (3D), are used to outperform conventional energy storage materials (*91*–*93*). Additional increase in capacitance in metal oxide nanomaterials, such as $H_2Ti_6O_{13}$ and Nb_2O_5, is observed due to their open layered structure suitable for intercalation (*91*, *93*).

ZnO-based nanomaterials are promising for energy storage applications due to their low cost, lack of toxicity, synthetic variability (morphologies include spheres, nanowires and 3D nanonetworks) (*94*). Band engineering for these materials has been shown to be very fruitful (*21*). ZnO NC capacitors can be electronically charged directly via photodoping (*21*) or via electron transfer (*44*) and their capacitance can be measured by potentiometric titrations (*95*). It has been recently shown that Fe-doped ZnO NCs exhibit very high capacitances due to equilibrium between electron localization by Fe^{3+} dopants and electron delocalization within

the conduction band (*92*). However, what is not yet known, is the effect on capacitance of dopants other than Fe^{3+}. Moreover, the possibility of increasing capacitance with other methods, such as intercalation or shape/media tuning remains largely unexplored for ZnO-related nanomaterials.

In order to be able to implement band engineering for design of new promising materials for semiconductor electronics and energy storage it is critical to understand the "structure – properties" relationship in electronically doped NCs. In this work the effect of Al-doping, Li^+ intercalation, change in morphology and supporting media on properties of ZnO NCs are addressed.

5.2 Strategies for achieving supercapacitance in colloidal ZnO nanocrystals

We have observed increase in ZnO NC capacitance under following conditions: (1) change in supporting media (electrolyte), (2) non-spherical NC shape, (3) doping of ZnO NCs with aluminum, and (4) presence of Li^+ ions in solution.

5.2.1 Effects of electrolyte concentration on ZnO capacitance

To probe the effect of electrostatic interactions in double layer on capacitance, specEchem was conducted on ZnO NCs, synthesized by alkaline-activated hydrolysis and condensation procedure (*96*).

ZnO NC were characterized by TEM and XRD. **Figure 5.1**a shows that ZnO sample consists of spherical NCs with average size r = 3.15 nm. XRD data from **Figure 5.1**b demonstrates that ZnO phase is well maintained, because red trace (experimental diffraction pattern) does not have any extra or lost reflections compared to black trace (reference from ICSD database).

Potentiometric titrations of ZnO NCs in 0.1M electrolyte are shown in **Figure 5.1**c. The slope of the titration curve (14mV/eq; Cs =9 μF cm^{-2}) is steeper compared to the slopes of titration curves from 2 different experiments (1.4mV/eq; 3.1 mV/eq; Cs = 94 μF cm^{-2} and 42 μF cm^{-2} respectively) in 0.2M electrolyte given in **Figure 5.1**d. Table 5.1 displays the experimental data and capacitance values. This data indicates that simple change in NC supporting media results in increase in capacitance, providing further support to the hypothesis that electrostatic interactions govern capacitance.

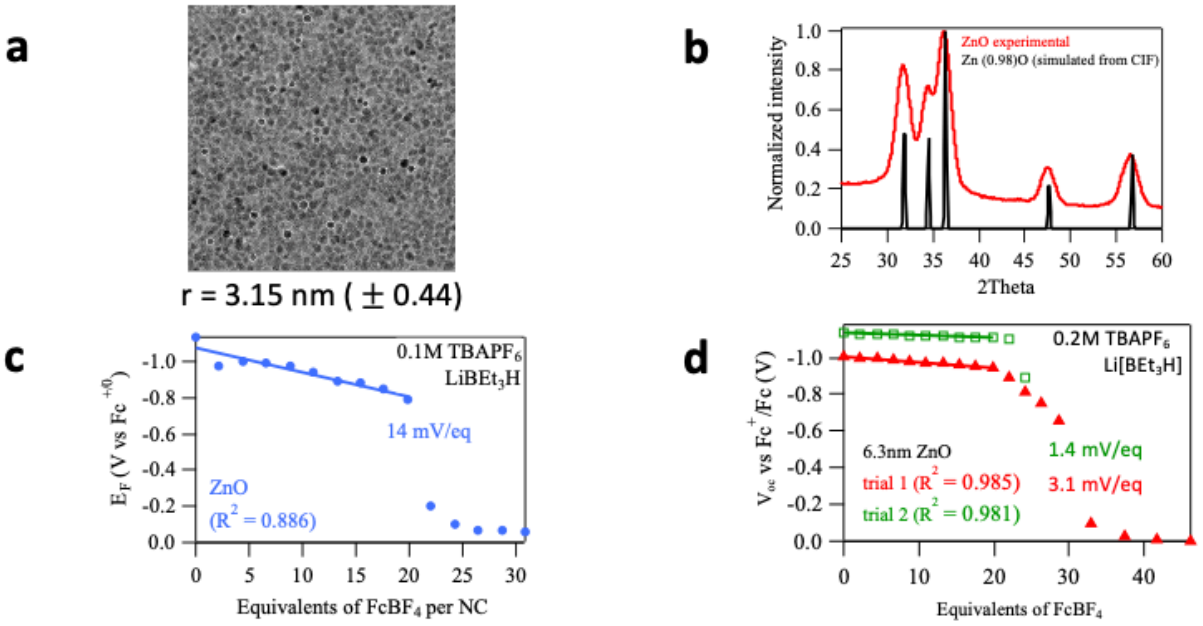

Figure 5.1 **Effect of electrolyte concentration on capacitance.** (a) TEM image of ZnO NCs. 100 nanocrystals were counted to determine average NC size. (b) XRD data for the r = 3.15 nm ZnO NCs from panel a and the bulk ZnO diffraction pattern from ICSD (black trace, deposition number 290323) shown for comparison. (c, d) Potentiometric titrations of colloidal r = 3.15 nm ZnO NCs in (c) 0.1M and (d) 0.2M $TBAPF_6$ (2 trials). Red, blue and green lines are linear fits to the data while photodoped electrons are titrated. Slopes of the fits are given in mV/eq and are proportional to capacitance.

Table 5.1 Capacitance of ZnO NCs electronically doped in different environment.

$TBAPF_6$ concentration, M	mV/equiv.	C_s (uF*cm^{-2})
0.1	14	9
0.2 (trial 1)	3.1	42
0.2 (trial 2)	1.4	94

5.2.2 Increase in capacitance in non-spherical ZnO nanocrystals

One of the key practical factors to increase capacitance is large surface area (*88*). Shape anisotropy of NCs is known to affect properties of excess electrons in NCs (*97*). Indeed, **Figure 5.2** shows shallow slope (0.542 mV/eq) for tetrapod ZnO NCs synthesized by modified etching-regrowth-doping procedure (*98*). Capacitance values of spherical ZnO NCs of similar size (average size determined by XRD) predicted from literature are 10 times smaller (*95*). It is possible, therefore, that increase in capacitance for tetrapod sample is due to increased surface area and perturbations in double layer around tips of tetrapods.

Synthesis of tetrapod ZnO NCs. In a typical reaction for ZnO NCs, $Zn(oleate)_2$ (0.63 g, 1 mmol) was dissolved in 7.89 g of ODE in a 100 mL three-necked flask. The reaction mixture was first degassed and then put under N_2. This step was repeated several times. After that the flask was heated to 100°C under vacuum for 10 min to remove any residual water. The solution was then heated to 300°C under nitrogen flow. A separate solution was prepared by heating solid DDOH to room temperature and mixing (2.25ml, 10 mmol) of it with 1.6 g of ODE as soon as DDOH melts. After that DDOH/ODE solution was heated to 150°C in oil bath and rapidly injected into the reaction flask at 300°C. The reaction temperature dropped to 280°C, and the solution was kept at this temperature for 30 min for ZnO NCs to grow. Then NCs were cooled to room

temperature and washed three times with ethanol. After washing NCs were dried under N_2 and the pallet was transferred to the glovebox and dissolved in THF.

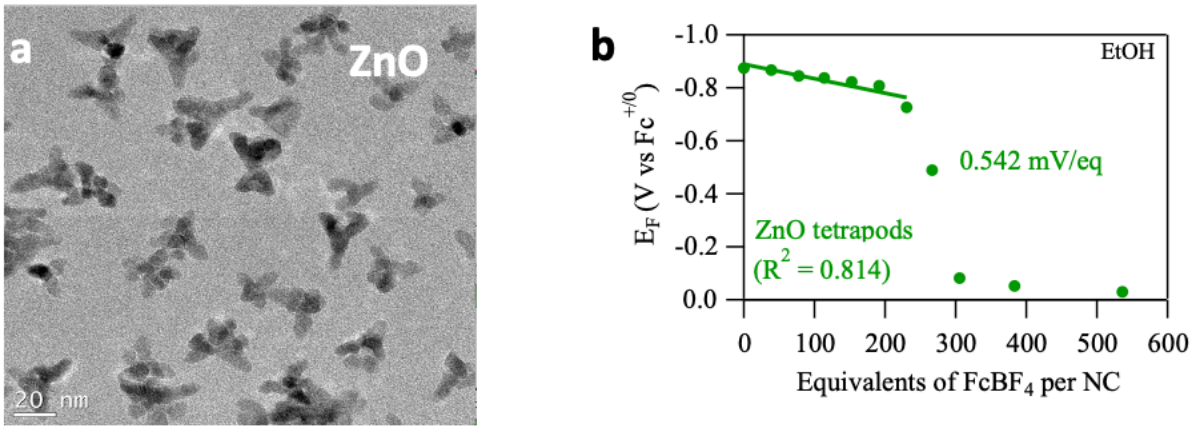

Figure 5.2 Capacitance and ZnO morphology. (a) TEM image of tetrapod ZnO NCs. (b) Potentiometric titrations of colloidal tetrapod ZnO NCs. Green line is a linear fit to the data while photodoped electrons are titrated. Slope of the fit is given in mV/eq and is proportional to capacitance.

5.2.3 Emergence of supercapacitance upon ZnO doping with aluminum

Aliovalent doping offers a powerful approach to NC band engineering. Aluminum-doped ZnO (AZO) feature stable conduction-band electrons compensated by the dopant, while retaining the ability to further accumulate more electrons (e.g., via photodoping). The study of AZO has been previously hampered by the lack of an efficient Al aliovalent doping procedure, which resulted in only some Al^{3+} cations that entered the NC and substituted Zn^{2+} being compensated by delocalized electrons (*21*). A recently reported novel doping procedure (*98*) has enabled significant accumulation of Al^{3+} inside host NCs resulting in enhanced n-type character of AZO. In my work I apply this procedure to obtain AZO NCs with high Al content and study properties of excess electrons in these materials.

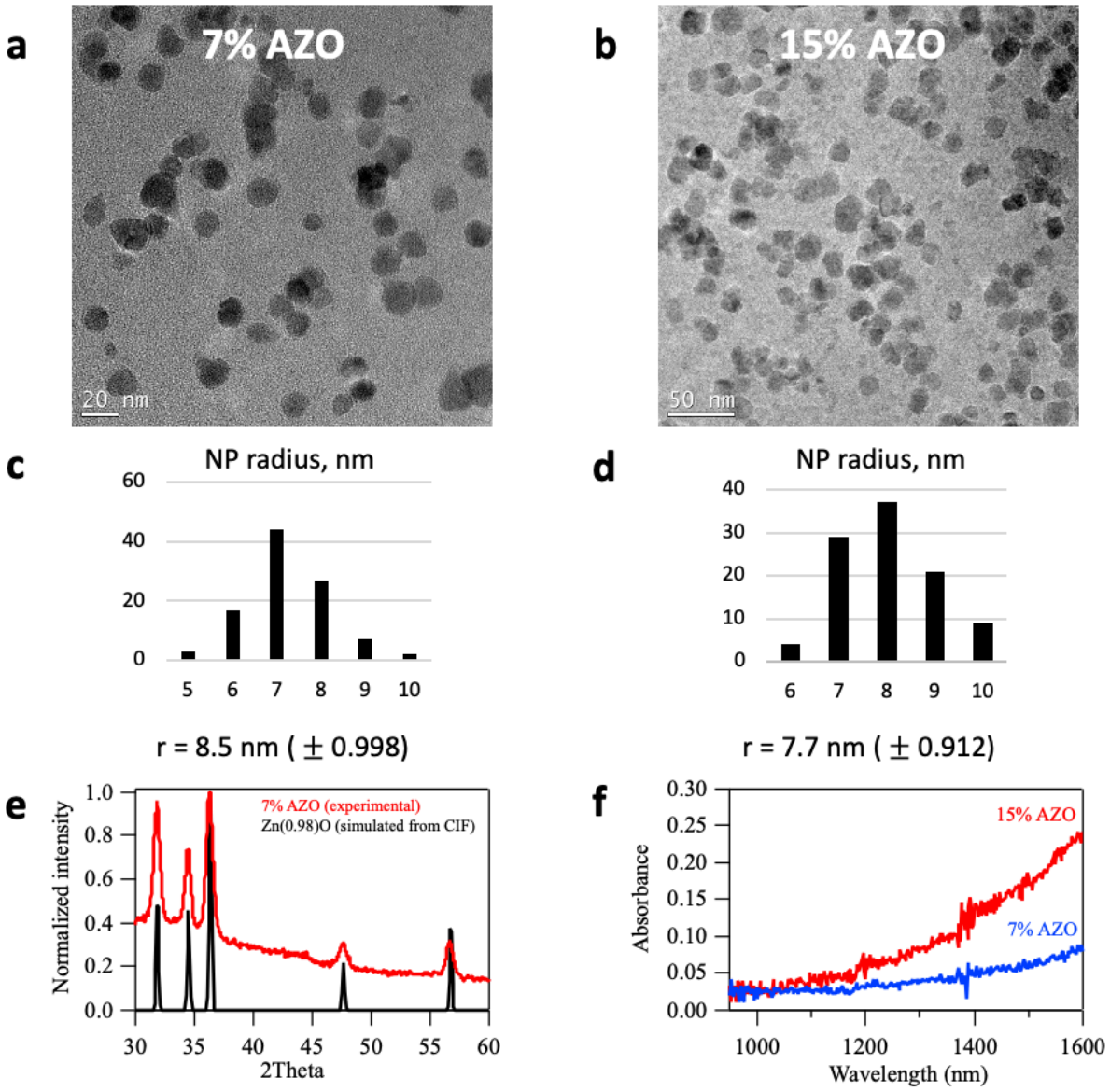

Figure 5.3 **AZO sample characterization.** (a, b, c, d) TEM images and size histograms of Al-doped ZnO NCs with different Al content. 100 nanocrystals were counted to create size histogram for each sample. (e) XRD data for the r = 7.7 nm 7% Al-doped ZnO NCs (red) from panel (a) and the bulk ZnO diffraction pattern from ICSD (black trace, deposition number 290323) shown for comparison. (f) Absorption spectra of colloidal r = 7.7 nm 7% Al-doped ZnO NCs (blue) and r = 8.5 nm 15% Al-doped ZnO NCs (red). The spectra were measured in 0.1M $TBAPF_6$/THF solutions through fiberoptic cables.

Synthesis of Al-doped ZnO (AZO) NCs. AZO NCs were synthesized by etching-regrowth-doping procedure (*98*). $Zn(oleate)_2$ (0.63 g, 1 mmol) and $Al(oleate)_3$ (0.17 g, 0.2 mmol) was dissolved in 7.89 g of ODE in a 100 mL three-necked flask. The reaction mixture was first degassed and then put under N_2. This step was repeated several times. After that the flask was heated to 100°C under vacuum for 10 min to remove any residual water. The solution was then heated to 300°C under nitrogen flow. A separate solution was prepared by heating solid DDOH to room temperature and mixing (2.25ml, 10 mmol) of it with 1.578 g of ODE as soon as DDOH melts. After that DDOH/ODE solution was heated to 150°C in oil bath and rapidly injected into the reaction flask at 300°C. The reaction temperature dropped to 280°C, and the solution was kept at this temperature for 30 min to allow the growth of ZnO NCs. Next, solution of OA (0.565g, 2 mmol) was dissolved in 1.6 of ODE, heated to 150°C and rapidly injected into the reaction mixture to etch NCs. Then solution was heated at 280°C for another 30 min to allow AZO NCs to regrow. Then NCs were cooled to room temperature and washed three times with ethanol. After washing NCs were dried under N_2 and the pallet was transferred to the glovebox and dissolved in THF.

Characterization of Al-doped ZnO (AZO) NCs. AZO NCs were characterized by TEM, XRD and absorption spectroscopy. **Figure 5.3**a,b shows that both AZO samples with different Al content consist of spherical NCs. Average size of NCs was determined from TEM images and size histograms are shown in **Figure 5.3**c,d. XRD data from **Figure 5.3**e demonstrates that ZnO phase is well maintained in AZO NCs, because red trace (experimental diffraction pattern) does not have any extra or lost reflections compared to black trace (reference from ICSD database). **Figure 5.3**f shows that both AZO samples exhibit LSPRs indicating the presence of free excess electrons in AZO NCs (*97*).

Spectroelectrochemical investigation of excess electrons in AZO NCs. Electronic doping deposits electrons in the conduction band of NCs and thus changes chemical potentials in the system. The most common electrochemical method to measure these changes is cyclic voltammetry (CV). However, lack of optical control, difficulty of analysis of peaks associated with NCs and possibility of sample decomposition during the CV experiment makes spectroelectrochemistry (specEchem) a more suitable technique for understanding RedOx properties of colloidal NCs (*26*, *44*). During typical specEchem experiment NCs are dissolved in TBAPF6/THF mixture and placed in a 4ml cuvette with a stir bar in the N_2 atmosphere inside the glovebox. Three electrodes (Ag/AgCl reference, Pt working and Pt counter), connected to the potentiostat outside the glovebox through coaxial cables, are inserted through the rubber cuvette cap, and cuvette holder is coupled to the spectrophotometer through fiberoptic cables to ensure that spectroscopy can be done at the same time with potentiometry. Potentiostat is set up in galvanostatic mode to measure the Fermi level of the solution. Hole quencher (EtOH or $LiEt_3BH$) is added to the NC solution and the LED is turned on to start photodoping. Completeness of the photodoping is determined based on lack of change in absorption. Absorption spectra in **Figure 5.4**a show AZO NCs before (red) and after (blue) photodoping. As soon as photodoping is done, equivalents of $FcBF_4$ are added to titrate excess electrons from the conduction band of AZO. **Figure 5.4**a shows how absorption changes during titrations of photodoped (light blue traces) and Al-compensated (grey traces) electrons. NC absorption (light blue and grey traces in panel a) relative to the absorption before photodoping (red trace in panel a) decreases linearly with the increasing amount of added $FcBF_4$ indicating no change in oxidation state of Al (**Figure 5.4**b). In a recent study of Fe-doped ZnO NCs (*95*) nonlinear behavior of absorption was attributed to changes in oxidation state of Fe responsible for high capacitance values in this material. The change in open circuit potential of the AZO solution is measured at the same time as changes in absorption during titrations (**Figure 5.4**c). This change

in potential is plotted vs equivalents of $FcBF_4$ in **Figure 5.4**d allowing us to analyze the slope of the potentiometric curve proportional to NC capacitance (*95*).

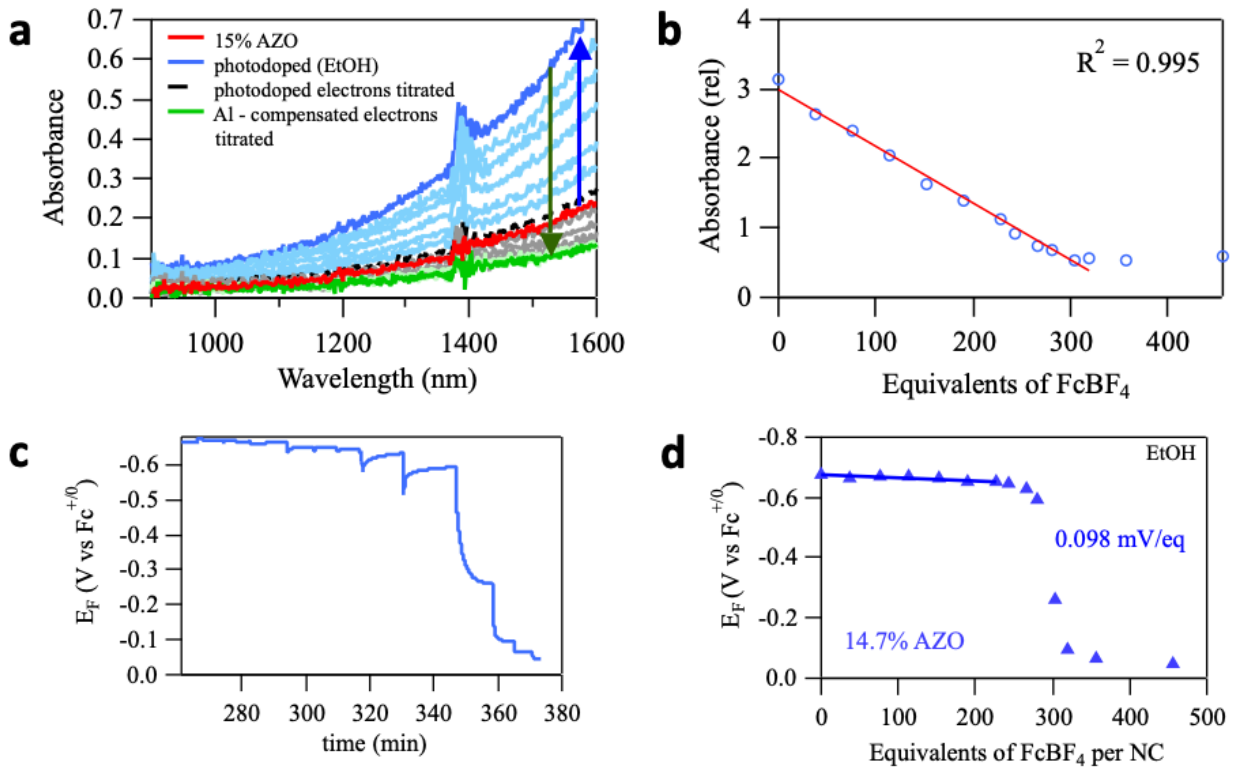

Figure 5.4 **SpecEchem of 15% AZO.** (a) Absorption spectra of as prepared (red, same as Fig. 1 (f)), maximally photodoped (blue) r = 8.5nm AZO NCs (containing 15% Al) during photodoping (light blue) and titrations with $FcBF_4$ (grey). The arrows show the direction of increasing excitation exposure time (blue) and the direction of increasing amount of $FcBF_4$ equivalents (dark green). (b) Relative absorption (absorption at 1600nm divided by absorption of as-prepared AZO sample) vs total number of $FcBF_4$ equivalents added during titrations (panel a). Red line is a linear fit to the data while absorption keeps changing. (c) Potentiometry: open circuit potential of the system (panel a) during titrations. (d) Potentiometric titrations: the Fermi level of the 0.1M $TBAPF_6$/THF AZO NC solution vs equivalents of $FcBF_4$ added during titrations. Blue line is a linear fit to the data while photodoped electrons are titrated (based on blue traces in panel a). Slope of the fit is given in mV/eq and is proportional to capacitance.

Increase in Al content of AZO NCs results in increase in capacitance. **Figure 5.5**a shows specEchem data for 7% AZO NCs. In order to evaluate the effect of Al-doping on specific areal capacitance (independent from surface area of the sample), data from **Figure 5.5**a and **Figure 5.4**d was normalized by surface area of the NCs and plotted in **Figure 5.5**b for comparison. The slope of the potentiometric curve becomes steeper with the decrease of Al content in the sample.

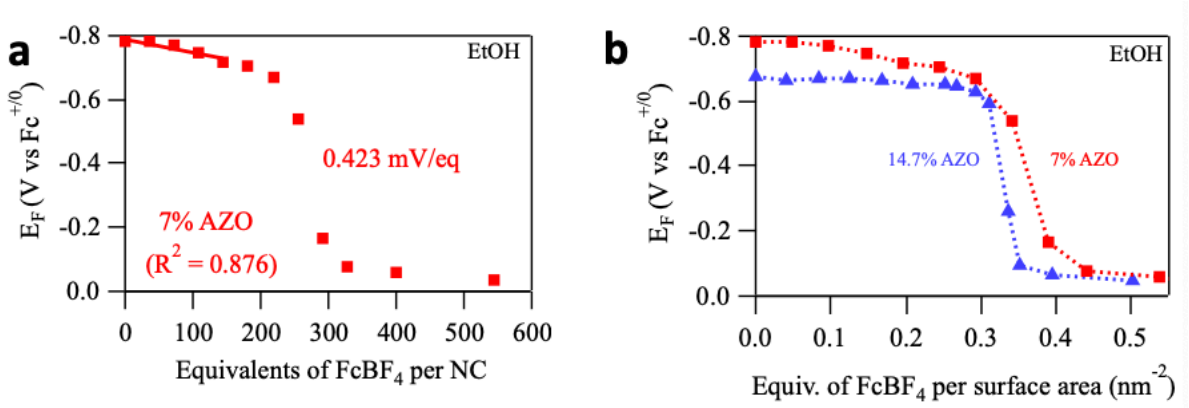

Figure 5.5 **Change in potentiometric titrations for AZO NCs with different Al content.** Potentiometric titrations of colloidal (a) r = 7.7 nm 7% Al-doped ZnO NCs (red). Red line is a linear fit to the data while photodoped electrons are titrated. Slope of the fit is given in mV/eq and is proportional to capacitance. (b) Superposition of data from panel a (red trace) from this Figure and panel d (blue trace) from Fig. 2 normalized by surface area of NCs.

Table 5.2 summarizes slope values for both AZO samples. Experimental capacitance (C) and specific areal capacitance (Cs) were calculated using equation 1, where ΔV is a change in potential, ΔQ is the change in charge, and surface area of NCs, A, – using equation 2, where r is the NC radius taken from **Figure 5.3**c,d.

$$\frac{1}{C} = \frac{1}{C_s A} \equiv \frac{\Delta V}{\Delta Q} \equiv \frac{slope}{elementary\ charge} \qquad (1)$$

$$A = 4\pi r^2 \qquad (2)$$

The specific areal capacitance, Cs, for both AZO samples exceeds very high Cs (33 μF cm^{-2}) value reported for Fe:ZnO NCs. Supercapacitance in Fe:ZnO NCs is attributed to ability of Fe to change oxidation state from +2 to +3, which facilitates electron storage (*95*). However, Al is not known to exhibit changes in oxidation states, and absence of nonlinear change in absorption during AZO titrations (**Figure 5.4**b) confirms that.

Table 5.2 Capacitance of AZO NCs with different Al content.

Al^{3+} cation %	mV/equiv.	Experimental C (aF)	Cs (uF*cm^{-2})
7*	0.423	378	51
14.7	0.098	1633	180

*estimated based on plasmon intensity relative to 15% AZO

Thus it is hypothesized that very high capacitance values in AZO samples are due to electrostatic interactions as opposed to RedOx reactions in Fe:ZnO.

5.2.4 Li^+-induced supercapacitance in ZnO nanocrystals

Li intercalation is known to affect properties of bulk ZnO (*99*). Several reports have shown that presence of Li^+ increases capacitance for metal oxide nanomaterials with tunneled structure (*91*). Although no such studies could be found in literature for ZnO NCs this material has a network structure shown in **Figure 5.6**a,b with channels that can be clearly seen in comparison with another well-known oxide material In_2O_3 (**Figure 5.6**c,d).

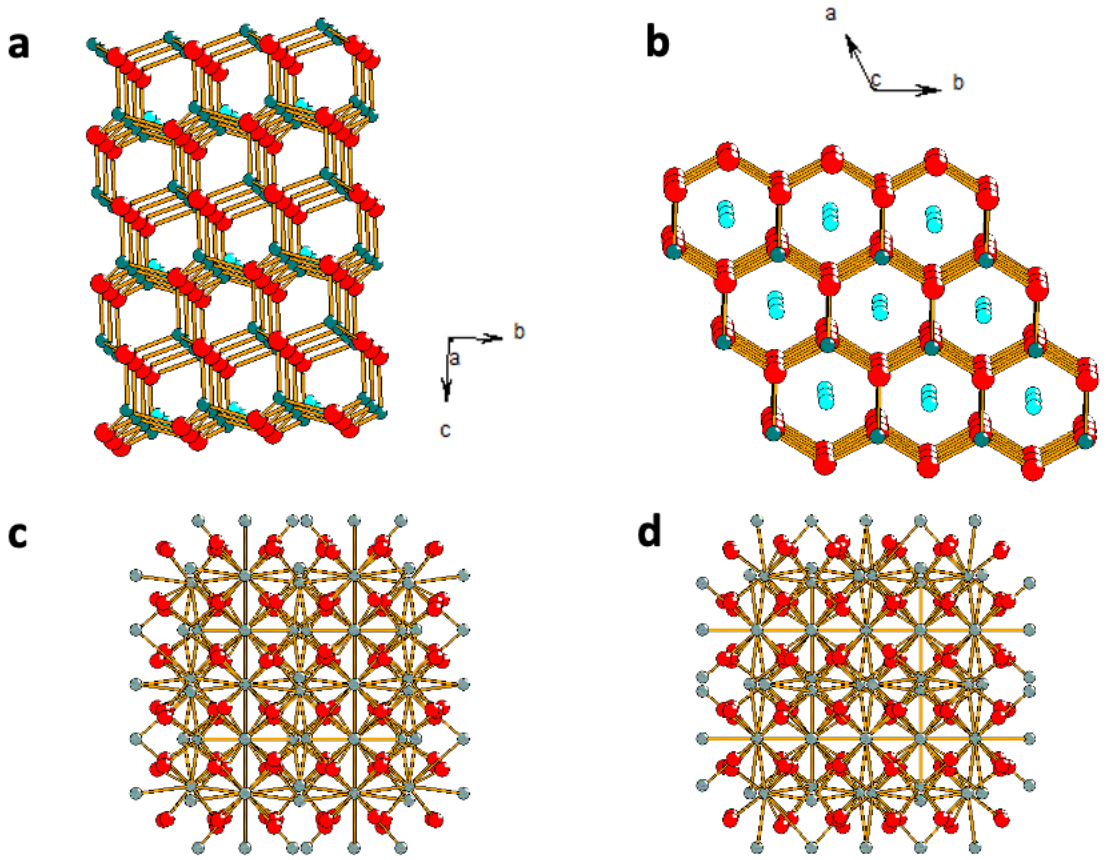

Figure 5.6 Crystal structures of Metal Oxide NCs. (a, b) Crystal structure of ZnO (Zn atoms shown in grey, oxygen atoms shown in red, Zn vacancies shown in cyan) (a) along a direction and (b) along c direction. (c, d) Crystal structure of In_2O_3 (In atoms shown in grey, oxygen atoms shown in red) (c) along a direction and (d) along c direction. Pictures created using DIAMOND software [http://www.crystalimpact.com/diamond].

Potentiometric titrations of photodoped ZnO NCs with EtOH (red) are presented in **Figure 5.7**. The slope of the titration curve (14mV/eq) is steeper compared to the slopes of titration curves (1.4mV/eq) in titrations of the same system with the only difference is $LiEt_3BH$ is used instead of EtOH. This data suggests that presence of $LiEt_3BH$ results in increase in capacitance. This result may be explained by the intercalation of Li^+ ions present in the solution into the channels in ZnO structure and thus capacitance is increased via electrostatic interactions.

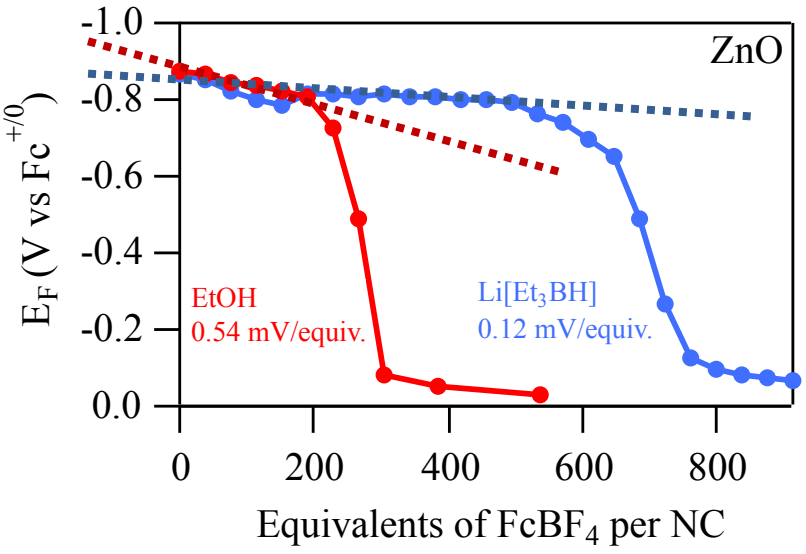

Figure 5.7 **Effect of Li+ on capacitance.** Potentiometric titrations of ZnO NCs in presence of different hole quenchers: EtOH (red) and $LiEt_3BH$ (blue). Red and blue lines are guides to an eye to show that slopes are different. Slopes of the fits (not shown) are given in mV/eq and are proportional to capacitance.

As mentioned in literature (*100*) the switch from EtOH to $LiEt_3BH$ in photodoping also results in higher electron capacities for ZnO NCs. My data on tetrapod ZnO NCs (**Figure 5.7**) supports this trend, as more $FcBF_4$ equivalents are needed to remove all photodoped electrons from ZnO NCs when $LiEt_3BH$ is used as a hole quencher in comparison to EtOH. However, more studies are needed to confirm this trend for spherical NCs.

It would also be interesting to investigate the effects of other similar hole quenchers, KEt_3BH and $NaEt_3BH$. The trend in ionic radii is the following: $r(Li^+) < r(Na^+) < r(K^+)$, where $r(Li^+)$ =0.59 Å, $r(Na^+)$ = 1.02 Å, $r(K^+)$ = 1.38 Å (*101*). Studies on tunneled oxide supercapacitor nanomaterial MnO_2 (tunnel size 4.6 × 4.6 Å) found that only Li^+ and Na^+ are able to intercalate, because steric strain for K^+ is too high (*102*). Tunnels in ZnO (tunnel size 4.5 × 3.2 Å) NCs are smaller than in MnO_2, however they may still be large enough for Na^+ intercalation. Further, several studies have demonstrated the effect of presence of large cations, such as K^+, on Li^+

intercalation in MnO_2. Some authors have concluded that Li^+ intercalation is impeded by large cations due to physical blocking and repulsive electrostatic forces. Others have argued that stable tunnel structure required for diffusion of Li^+ ions is facilitated by large cations (*103*). However, agreement on this question has not yet been found.

Intercalation-based supercapacitance combines high power and energy densities critical for charge storage applications. Establishing ways to enhance effect of intercalation will shed light on better supercapacitors and thus better energy storage materials.

5.3 Investigating origins of supercapacitance

With Sum-Frequency Generation (SFG) technique (*104*), it was expected to see changes in ion dynamics and no changes in structure of ZnO sample upon Li intercalation. Ion dynamics and structure changes in ZnO electrode (electrostatic charging hypothesized) were expected to be different in comparison with MnO_2 (redox charging supercapacitance mechanism concluded from literature). Difference in ion dynamics in spherical vs non-spherical ZnO NCs was also expected. However, sample quality was too poor (not crystalline enough) to obtain the expected results.

To compare effect of Li on supercapacitance with that of Al and Fe and to study the hypothesis that Li substitutes Zn upon photodoping with $LiEt_3BH$ and forms a state inside the band gap, thus leading to an increase in capacitance, Li-doped ZnO nanocrystals were directly synthesized.

Zinc oleate (0.63 g) and lithium acetate dihydrate (0.0322 g) were mixed with ODE (7.89 g) and oleic acid (0.0273 g) in 100 ml 3-neck flask, heated to 100°C under vacuum until airfree, then heated to 300°C under nitrogen. Separately dodecanol (2.25ml) and ODE (0.6 g) heated to

150°C (oil bath) and rapidly injected to the 3-neck flask. The flask is kept at 280°C for 30 min, nanocrystals washed with EtOH/hexanes 1- times for 5 min.

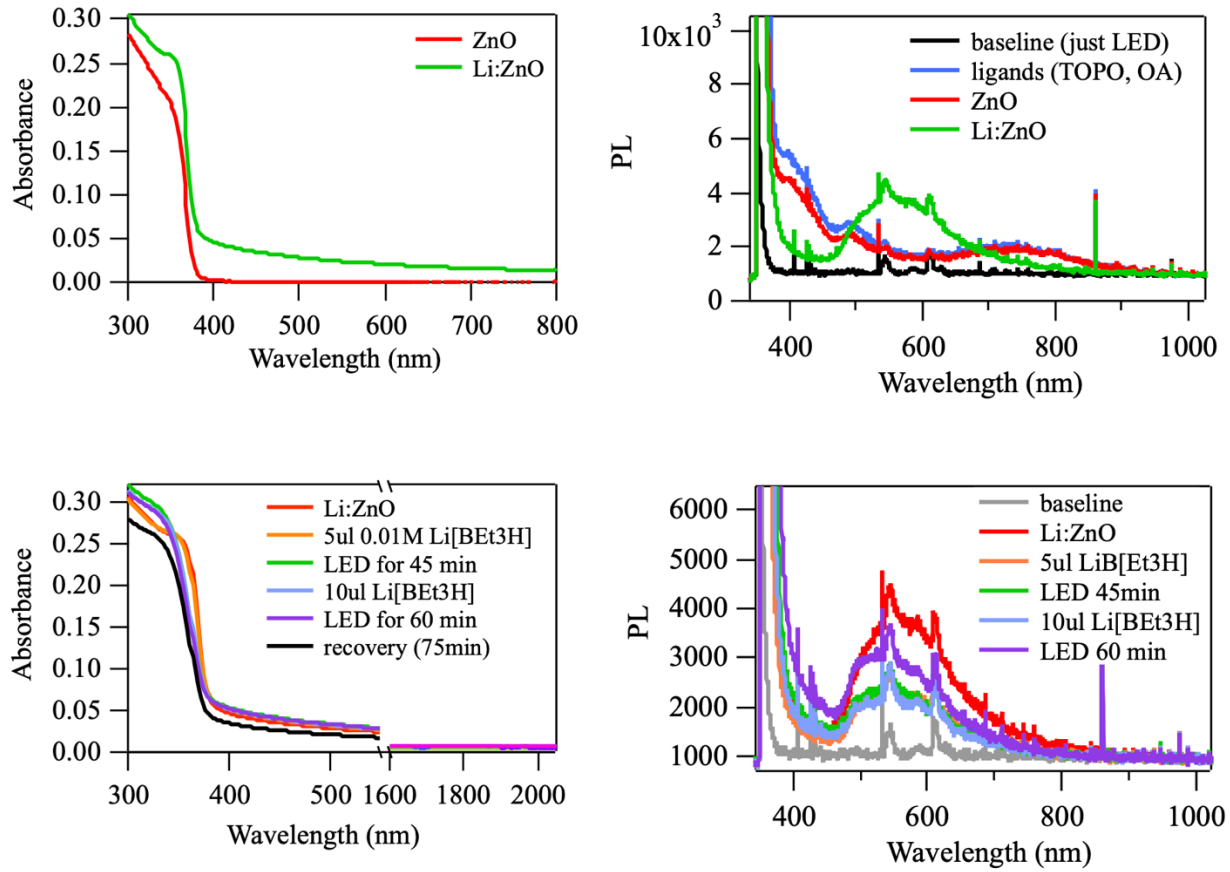

Figure 5.8 Spectroscopic investigation of Li doped ZnO nanocrystals. Top: absorption of Li:ZnO and ZnO. Bottom: photodoping of Li:ZnO

Spectroscopic behavior of Li:ZnO exhibits a better resolved excitonic feature (in comparison to ZnO) and a localized state with photoluminescence of the trap in agreement with literature. However, absorbance foot is growing in the presence of Li, indicating a possible loss of colloidal stability. Interestingly, photodoping of Li:ZnO NCs produced no plasmon, suggesting that there was no expected accumulation of free electrons, but resulted in changes in excitonic feature and decrease in trap photoluminescence, both indicating possible changes in Li cluster.

Modeling of electrostatic effects that govern supercapacitance (*53*, *92*, *105*, *106*) offers a deeper insight into origins of supercapacitance in nanomaterials and could help elucidate additional factors that affect this property. We looked at ZnO slabs passivated with ligands on 1-100 facet (**Figure 5.9**) and 0001 facet (**Figure 5.10**) and explored the effects of Li ion being interstitially inserted in the bulk of the slab, in the surface layer of the slab, and present outside of ZnO slab but not inserted.

Formation energy values suggest that Li inserted in ZnO slab is a preferred configuration, though structural reorganization within the slab occurs due to Li presence. O atoms move closer to Li atoms inside the slab suggesting electrostatic nature of structural distortions.

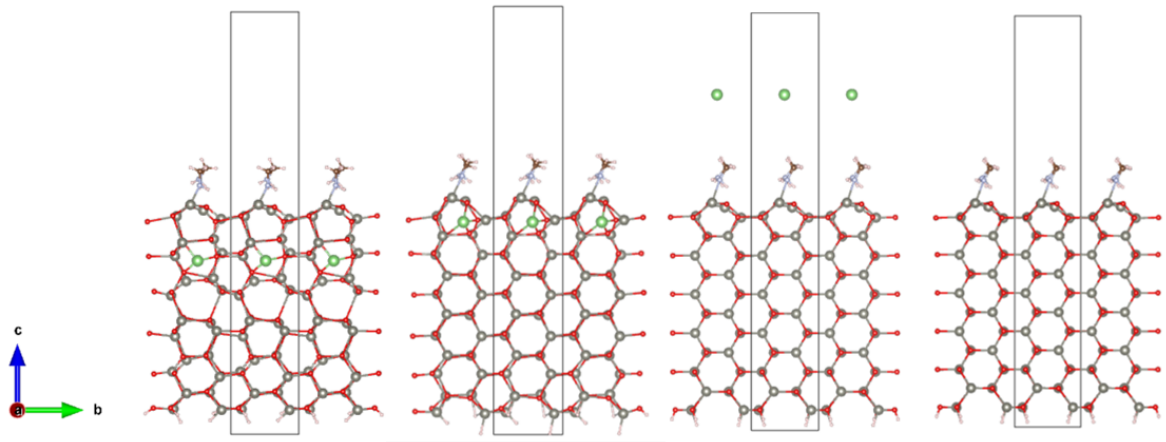

Figure 5.9 Modeling of 1-100 ZnO slabs with Li insertion. ZnO slab with DDA ligand passivation was used for modeling. (A) Slab with Li inserted in the bulk of the slab. (B) Li inserted in the surface layer of ZnO slab. (C) Li is present outside of ZnO slab, but not inserted. (D) ZnO slab without Li.

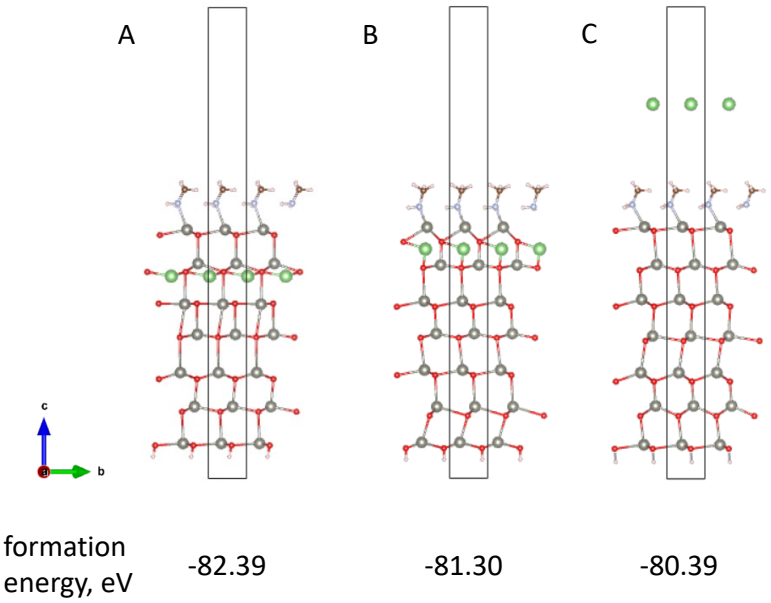

Figure 5.10 Modeling of 0001 ZnO slab with Li insertion. ZnO slab with DDA ligand passivation was used for modeling. (A) Slab with Li inserted in the bulk of the slab. (B) Li inserted in the surface layer of ZnO slab. (C) Li is present outside of ZnO slab, but not inserted. Formation energies are listed under each structure.

5.4 Summary

ZnO-based nanomaterials are promising for a wide range of applications, particularly semiconductor electronics, due to their synthetic tunability, low cost, and lack of toxicity. The utility of these materials stems from the large electron capacity and the ability to be electronically charged via defect doping, photodoping, and electron transfer. Band engineering for these materials has been shown to be very fruitful. Here we explore unique energy storage properties of ZnO and ZnO-related colloidal nanocrystals with focus on supercapacitance and band-edge potential tuning. We show that ZnO acquires a surprisingly high capacitance under various conditions, such as Al doping, interactions with Li^+, and shape/media changes (**Figure 5.11**), and propose a hypothesis attributing these effects to electrostatic interactions on the nanocrystal surface and within the tunneled ZnO crystal structure. Overall, this work aims to

provide new insights into electronic properties and processes in colloidal ZnO and ZnO-related nanocrystals that would guide design and engineering of novel materials for energy storage.

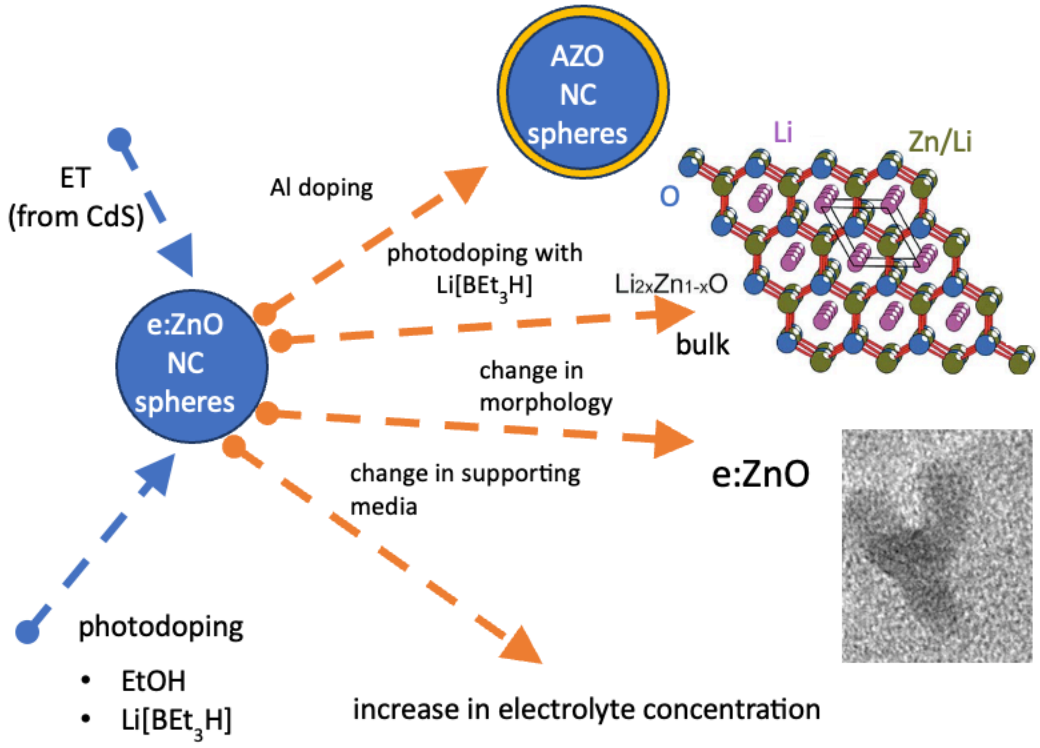

Figure 5.11 Summary of the approaches for increasing capacitance in ZnO nanocrystals. Supercapacitance is observed with Al doping, Li intercalation, change in nanocrystal morphology, and increase in electrolyte concentration.

CHAPTER 6: ELECTRON TRANSFER IN CdS/ZnO COLLOIDAL NANOCRYSTAL SYSTEM

Electron transfer (ET) in nanomaterials enables a wide range of clean energy applications. Electron transfer systems are designed based on the knowledge of electrochemical potentials of interacting components, which control ET behavior (*4*, *5*, *23*, *107–112*), with transfer being expected to proceed from higher to lower potential (*113*, *114*). Through our investigation of electron transfer in CdS/ZnO colloidal nanocrystal system, we found that electron transfer proceeds from CdS to ZnO upon selective CdS NC photodoping, contrary to expectations from bulk band-edge potentials (BEPs) for individual components of the mixture (described in Chapters 4 and 5). In this unique system electron accumulation happens on the order of minutes to hours, which enables direct observation of this process in real time. Chapter 6 describes experimental setup, material preparation, and experimental techniques used for the study of this unexpected phenomenon.

6.1 Synthesis and characterization of ZnO and CdS NCs

ZnO NCs. Spherical QDs were synthesized using known procedure (*96*). In brief, tetramethylammonium hydroxide ($N(Me)_4OH \cdot 5H_2O$) in ethanol is added dropwise to $Zn(OAc)_2 \cdot 2H_2O$ dissolved in DMSO under constant stirring. NCs are precipitated by addition of ethyl acetate and washed. After that the NCs were capped with DDA and then with TOPO and washed with EtOH. Diameter of particles (6.3 nm) was determined from TEM and ICP data (**Figure 6.1**).

The diameter of particles could not be determined based on energy of the first excitonic feature, because ZnO NCs are not quantum confined.

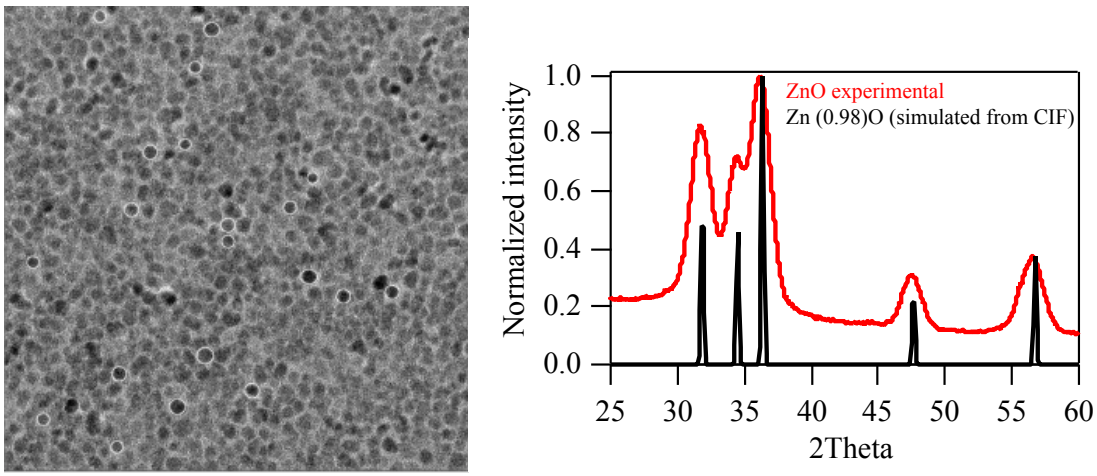

Figure 6.1 Characterization of ZnO nanocrystals. (a) TEM and (b) ICP showed monodisperse spherical nanoparticles with diameter of 6.3 nm.

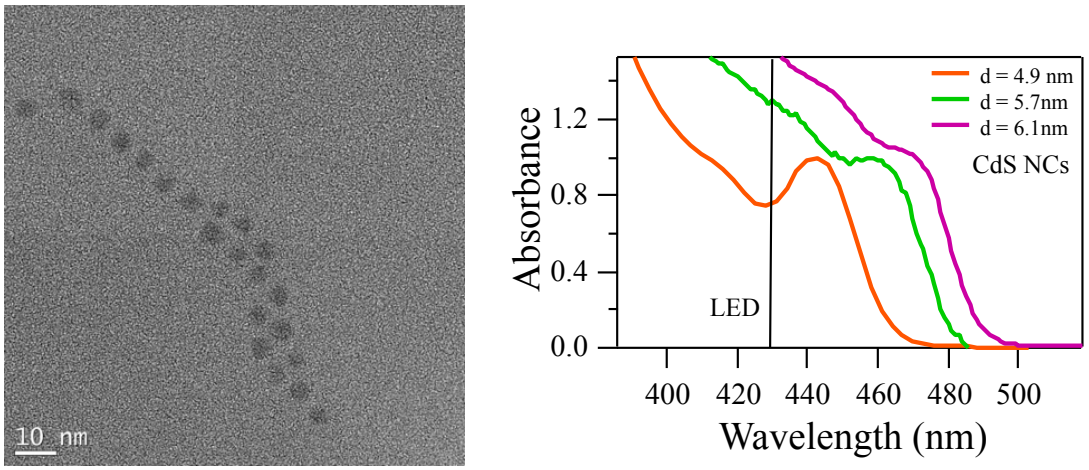

Figure 6.2 Characterization of CdS nanocrystals. (a) TEM and (b) UV-Vis spectroscopy confirmed production of spherical nanoparticles with tunable size.

CdS NCs. Spherical QDs were synthesized using known procedure (*84*). In brief, mixture of CdO, OA and ODE is heated to 300°C, TOP is added. After that the mixture of S in ODE is swiftly injected. Reaction should be quenched immediately after injection. Particles were washed with methanol and ethanol/acetone mixture. Diameter of particles (5.8 nm) was determined based on energy of the first excitonic feature (**Figure 6.2**) (*85*).

6.2 Electron transfer in CdS/ZnO colloidal nanocrystal system

Experiments were performed under inert atmosphere in $TBAPF_6$ as supporting electrolyte with $LiEt_3BH$ or EtOH as a hole quencher. Selective photoexcitation of CdS NCs was performed with Xe/Hg lamp and 440nm long-pass filter or 430nm LED (ThorLabs) (**Figure 6.3**). Control experiments confirming that ZnO was not excited directly were conducted under same conditions as selective excitation but without CdS NCs (**Figure 6.4**).

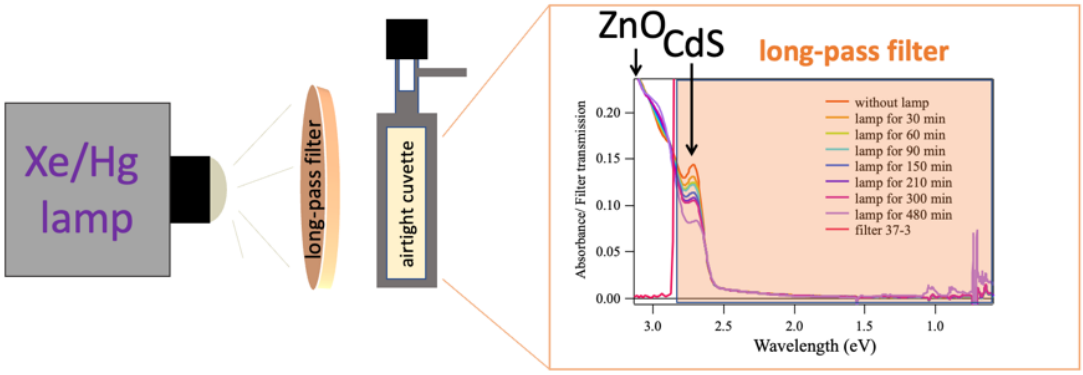

Figure 6.3 Experimental setup for the study of CdS-to-ZnO electron transfer. Selective photoexcitation produced electron doping on CdS, but not ZnO, nanocrystals. Consequent electron transfer from CdS to ZnO resulted in electron accumulation on ZnO nanocrystals, as evident by increase in Near-IR plasmonic absorption.

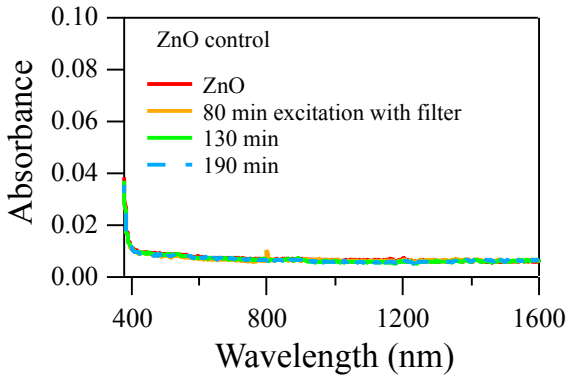

Figure 6.4 Control experiment for CdS-selective excitation. In the absence of CdS NCs, ZnO does not accumulate electrons under excitation with Xe/Hg lamp and 440nm long-pass filter or 430nm LED.

Since the band-edge potentials of CdS and ZnO turned out to be energetically similar (band-edge potential of ZnO is – 1.22 V vs $Fc^{+/0}$ (*44*)), we hypothesized that simultaneous electronic doping in mixtures of CdS and ZnO NCs was possible. We were able to observe inter-QD electronic equilibrium when CdS was selectively photodoped. Evidence for this equilibrium is shown in **Figure 6.5**a, where simultaneous exciton bleach in CdS and near-IR plasmonic absorption from doped ZnO are observed. From **Figure 6.5**b we see that CdS electron doping happens before electron transfer to ZnO. Photodoping of CdS begins immediately after excitation of CdS as observed by the bleach of the first excitonic feature. At the same time, no change in the CB of ZnO is initially observed. However, with continued CdS excitation we start seeing electron transfer from CdS to ZnO as shown by the increase of near-IR absorption feature of ZnO.

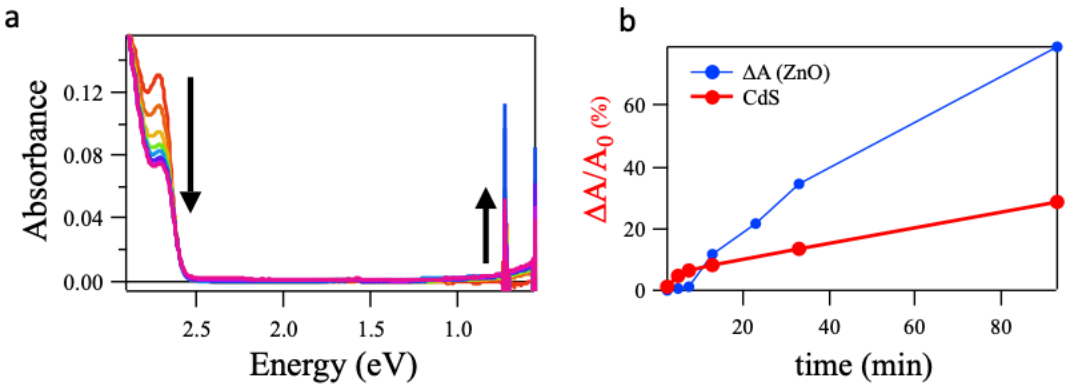

Figure 6.5 Simultaneous electronic doping in mixture of CdS and ZnO NCs. (a) electronic absorption spectra of as-prepared (red), fully electronically doped (pink) and intermediate cases (orange – purple) CdS NCs (d = 5.8 nm). Experiments were performed using TBAPF6 solution of CdS NCs, and EtOH. Electronic doping was conducted by selective photodoping of CdS NCs using EtOH as a hole quencher.

The constant of CdS/ZnO equilibrium (eq. 1) can be derived from spectra (eq. 2) and from potentials (eq. 3).

$$CdS^- + ZnO \leftrightarrow CdS + ZnO^- \qquad (1)$$

$$K = \frac{[CdS][ZnO^-]}{[CdS^-][ZnO]} \qquad (2)$$

$$\begin{aligned} \Delta G^0 &= -nFE^0_{cell} \quad E_F(V) = E_{cell}(V) \\ \Delta G^0 &= -RTlnK \\ \Delta G^0 &= -\Delta H - T\Delta S \end{aligned} \qquad (3)$$

Calculation of the equilibrium constant requires knowledge of ⟨n⟩ for CdS and ZnO. It is known from literature that CdS can hold up to two electrons in the conduction band (*115*). Quantitative titrations were conducted to find out the maximum number of electrons in the

conduction band of ZnO NCs (**Figure 6.6**). First, ZnO NCs are fully photodoped (**Figure 6.6**a). After that, equivalents of FcBF4 are added to remove the CB electrons, as evidenced by a decrease in the plasmon absorption (**Figure 6.6**b). Then this data is fitted to obtain the number of electrons that ZnO can hold in the conduction band (**Figure 6.6**c). This data shows that up to 5 electrons are added to the CB of these ZnO NCs under the doping conditions.

To gain insight on the redox properties of the doped CdS/ZnO mixture, specEchem experiments were conducted to find the potential that corresponds to the onset of the inter-QD electronic equilibrium (**Figure 6.7**). Preliminary results suggest that equilibrium is achieved when CdS has on average ⟨n⟩ = 0.35, and the potential that corresponds to the equilibrium onset is -0.94 V vs $Fc^{+/0}$.

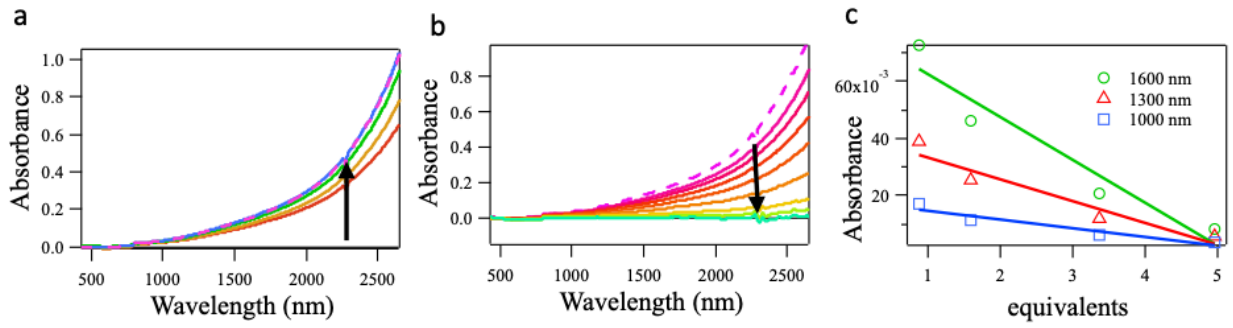

Figure 6.6 **Quantitative titrations of ZnO NCs.** (a) electronic absorption spectra of fully electronically doped (pink) and intermediate cases (red – blue) ZnO NCs (d = 7 nm). Experiments were performed using 0.1M $TBAPF_6$ solution of ZnO NCs and EtOH. Electronic doping was conducted by photodoping ZnO NCs using EtOH as a hole quencher. (b) electronic absorption spectra of fully oxidized (green) and intermediate cases (pink – yellow) ZnO NCs (d = 7 nm). (c) absorbance at different wavelengths from (b) is plotted vs number of equivalents of $FeBF_4$.

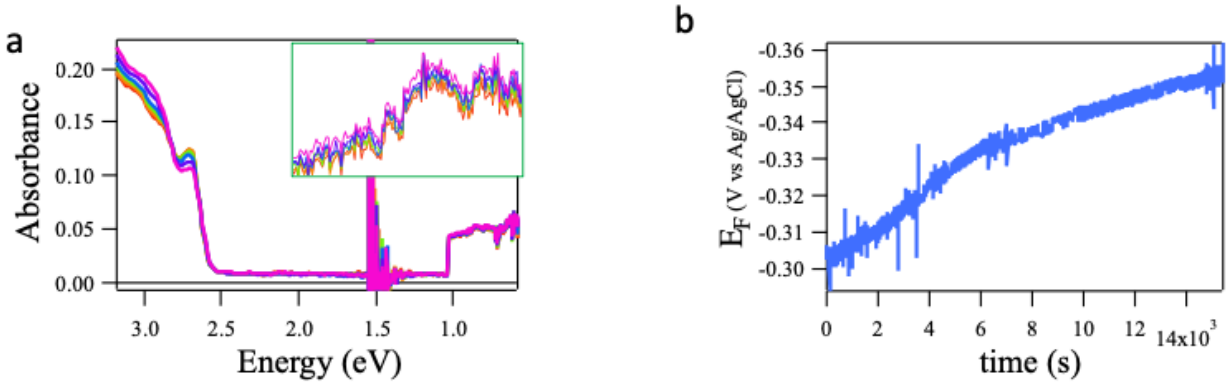

Figure 6.7 Spectroelectrochemical potentiometry in mixture of CdS and ZnO NCs. (a) electronic absorption spectra of as-prepared (red), fully electronically doped (pink) and intermediate cases (yellow – purple) CdS NCs (d = 5.7 nm). Experiments were performed using 0.1M TBAPF6 solution of CdS NCs, ZnO NCs and EtOH. Electronic doping was conducted by selective photodoping of CdS NCs using EtOH as a hole quencher. (b) Open-circuit potential of CdS/ZnO NCs mixture. Potential was measured simultaneously with absorption; inset: near IR feature of ZnO is blown up to show the increase in ZnO electronic doping.

Difference in conduction band potentials allows NCs with more positive band edge values to accept electrons from NCs with more negative conduction band potentials. A good example of such charging system is CdSe/ZnO NC mixture (*44*). Bulk band edge potential values suggest that in CdS/ZnO NC mixture electron transfer should be even more efficient, since the potential difference between CdS and ZnO conduction bands is bigger than that of CdSe and ZnO (*87*). Surprisingly, we have observed a less efficient electron transfer in CdS/ZnO NC system under selective CdS excitation, resulting in both CdS and ZnO NCs being electronically doped at the same time (**Figure 6.8**).

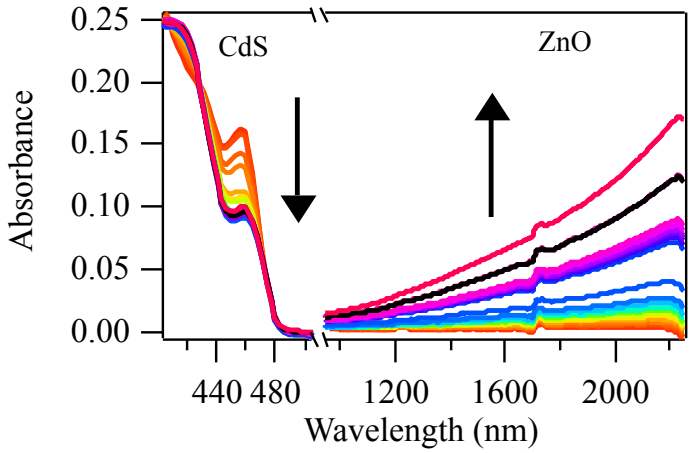

Figure 6.8 Electron transfer in CdS/ZnO mixture. Absorption spectra of a mixture of d = 5.8nm CdS NCs and d = 6.3nm ZnO NCs (molar ratio ZnO:CdS = 1:0.75) in 0.2M $TBAPF_6$ with $LiEt_3BH$ in airtight cuvette. Spectra collected after various durations (5min - 48hours) of selective photoexcitation of CdS NCs with Xe/Hg lamp and 440nm long-pass filter. Increase in ZnO NIR absorbance is attributed to electron transfer from CdS to ZnO NCs.

6.3 Kinetics of CdS/ZnO electron exchange

Kinetics of electron accumulation in NC mixture during inter-NC electron transfer is shown in **Figure 6.9**. Biexponential fit to the data reveals two steps in the process: fast and slow. This behavior is consistent with biexponential kinetics of electron accumulation during direct photodoping of ZnO NCs (*100*), but it occurs at a much slower pace in CdS/ZnO NC mixture.

Further analysis of charging of ZnO NCs through charge/discharge of CdS NCs is presented in **Figure 6.10**. Cycling between photodoping and recovery of CdS NCs is accompanied by accumulation of electrons in ZnO NCs, with fewer new electrons added with each cycle. This behavior may indicate that multicarrier Auger recombination usually competing with multiple electron accumulation (*100*) is not the only factor limiting electron transfer from CdS to ZnO. Another possible explanation is structural reorganization in ZnO NCs in order to facilitate charge compensation of many excess electrons.

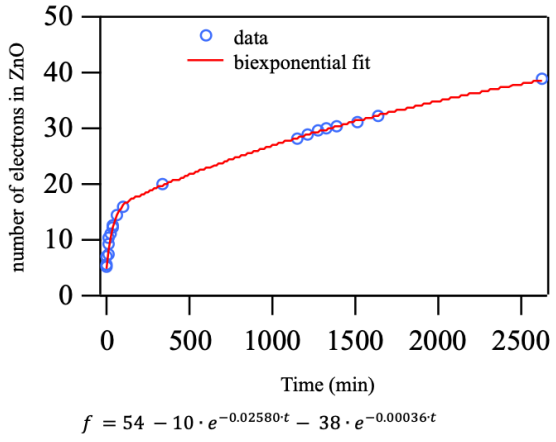

Figure 6.9 Kinetics of electron transfer. Number of delocalized electrons in the CB of ZnO is calculated using absorption data from Fig. 8 and plotted vs time of selective CdS photoexcitation. Biexponential fit (red line) to the data (blue circles) reveals two steps in electron accumulation in ZnO NCs.

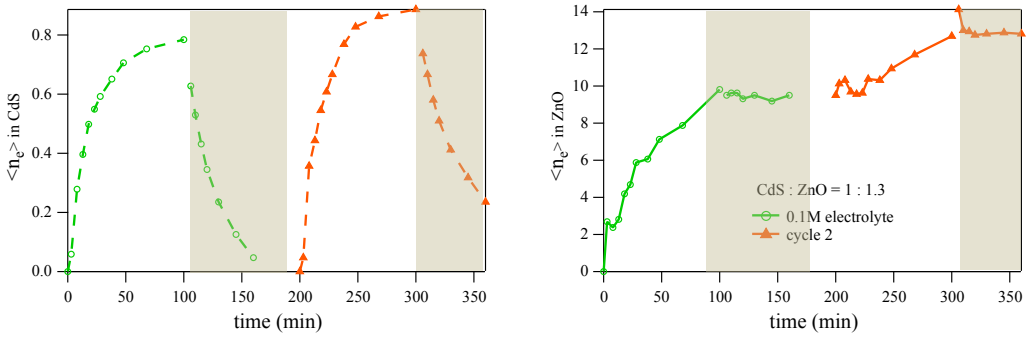

Figure 6.10 Charging of ZnO NCs through charge/discharge of CdS NCs in CdS/ZnO NC mixture. (a) Green circles (line is a guide to an eye) represent first CdS charge/discharge cycle in CdS/ZnO NC mixture. Number of delocalized electrons in the CB of CdS is calculated using absorption data (not shown) and plotted vs time of selective CdS photoexcitation (light area in the graph) and in the dark (grey area). Orange triangles (line is a guide to an eye) represent the second charge/discharge cycle that immediately follows the first (same experiment, same sample used). (b) Green circles (line is a guide to an eye) represent accumulation of electrons in ZnO NCs from first CdS charge/discharge cycle. Number of delocalized electrons in the CB of ZnO is calculated using absorption data (not shown) and plotted vs time (same timeline as in panel a) of selective CdS photoexcitation (light area in the graph) and in the dark (grey area). Orange triangles (line is a guide to an eye) represent accumulation of electrons in ZnO NCs from the second charge/discharge cycle that immediately follows the first (same experiment, same sample used).

Stability of accumulated CB electrons in CdS and ZnO NCs is compared in **Figure 6.11**. Electrons are accumulated in both CdS and ZnO during 45 hours of constant selective photoexcitation of CdS. When the excitation source is switched off electrons in the CB of ZnO are stably retained, whereas a rapid loss of CdS electrons is observed. When the NC mixture is exposed to air all CB electrons are gone from both CdS and ZnO. Longer stability of electrons in ZnO than CdS may be explained by the better availability of trap states for electrons leaving CdS.

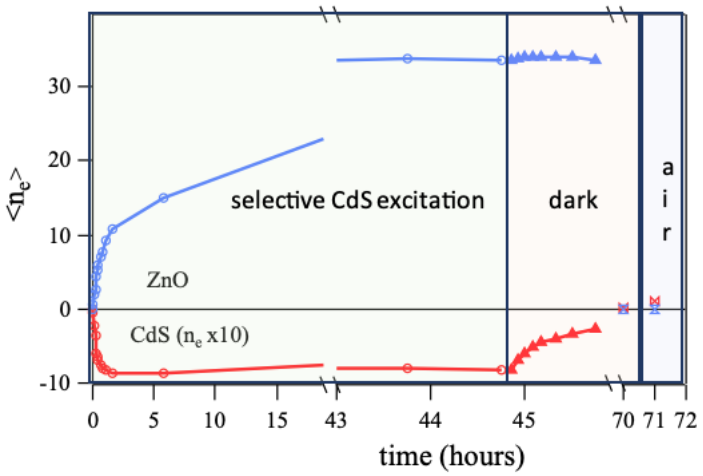

Figure 6.11 Difference in behavior of photodoped electrons in CdS and ZnO NCs. Number of delocalized electrons accumulated in the CB of ZnO (blue symbols, line is a guide to an eye) and lost in CdS (red symbols, line is a guide to an eye) is calculated using absorption data from Fig. 8 and plotted vs time of selective CdS photoexcitation (green area), recovery of exciton absorption in CdS (orange region), and exposure of NC mixture to air.

SpecEchem of the CdS/ZnO NC mixture reveals that potential of CdS NCs in the mixture is more negative than that in specEchem of CdS NCs alone (**Figure 6.12**). This data suggests that NCs interact and thus properties of the mixture are different from individual NCs under the same conditions. **Figure 6.12**d shows an interesting insight into this interaction: electron

accumulation in ZnO NCs happens only after CdS NC are fully photodoped. Prior studies have noted the importance of surface dipoles in tuning redox potentials of NCs (*21*). Thus, it is possible that ligand exchange in the NC mixture results in destabilization of CdS NCs and Fermi level equilibration between ZnO and CdS NCs leading to electron transfer.

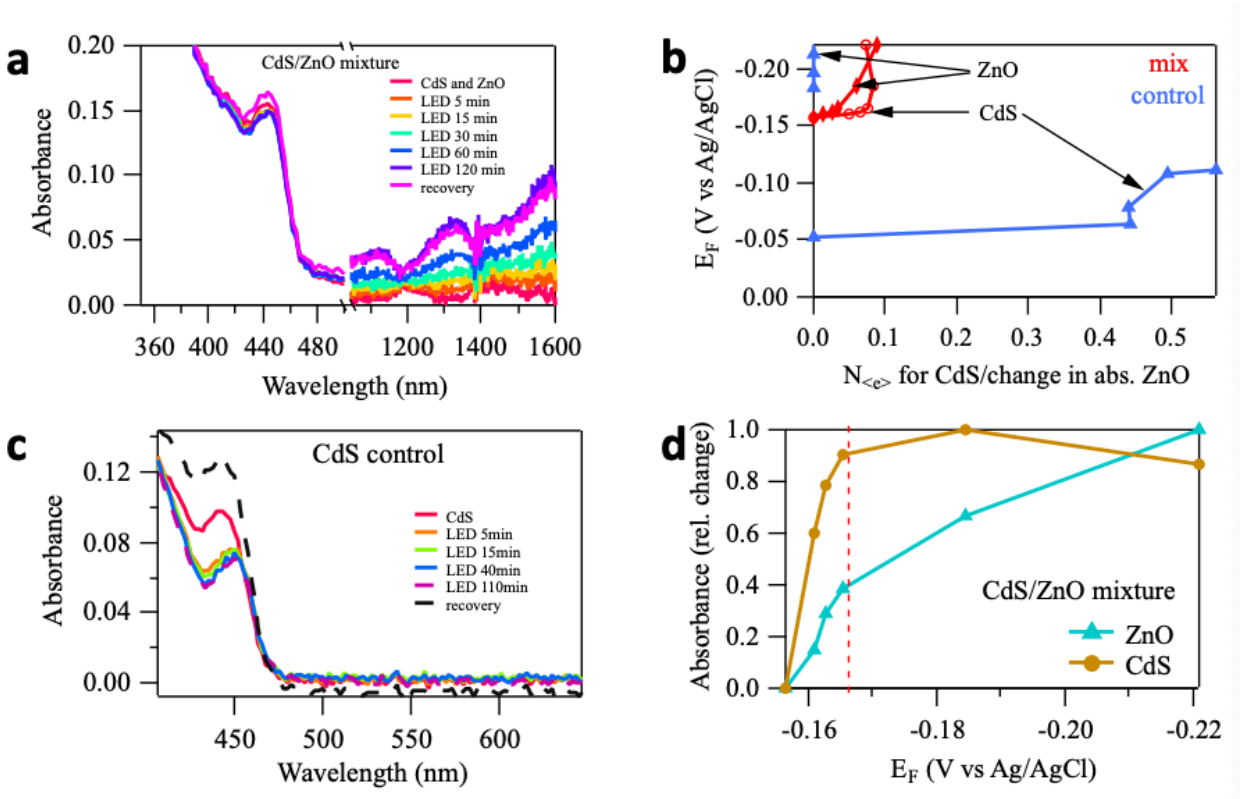

Figure 6.12 SpecEchem of CdS/ZnO NC mixture. (a) Absorption spectra of as prepared (red), maximally electronically doped (purple) CdS/ZnO NC mixture during selective CdS photoexcitation (orange – blue) and recovery in the dark (pink). (b) Open circuit potential of the CdS/ZnO NC mixture (red) and control experiments (ZnO or CdS NCs in the same experimental setup only, blue) during electron accumulation (number of electrons calculated from panel a). (c) Absorption spectra of as prepared (red), maximally electronically doped (purple) CdS NCs (control experiment) during selective CdS photoexcitation (orange – blue) and recovery in the dark (black). (d) Change in absorption spectra of CdS (yellow) and ZnO (cyan) NCs from the mixture vs open circuit potential (replotted from panel a, b). Red dashed line indicates complete photodoping of CdS.

6.4 Effect of electrolyte concentration on electron exchange efficiency

Change in electron accumulation rate in CdS/ZnO nanocrystal mixture when supporting media composition is altered is compared in **Figure 6.13**. This effect serves as an indirect confirmation of the change in relative potential difference in NCs. We attribute this effect to the change in surface charge compensation by the electrolyte, offering a new strategy for band engineering via a simple perturbation to electrolyte rather than the NC itself.

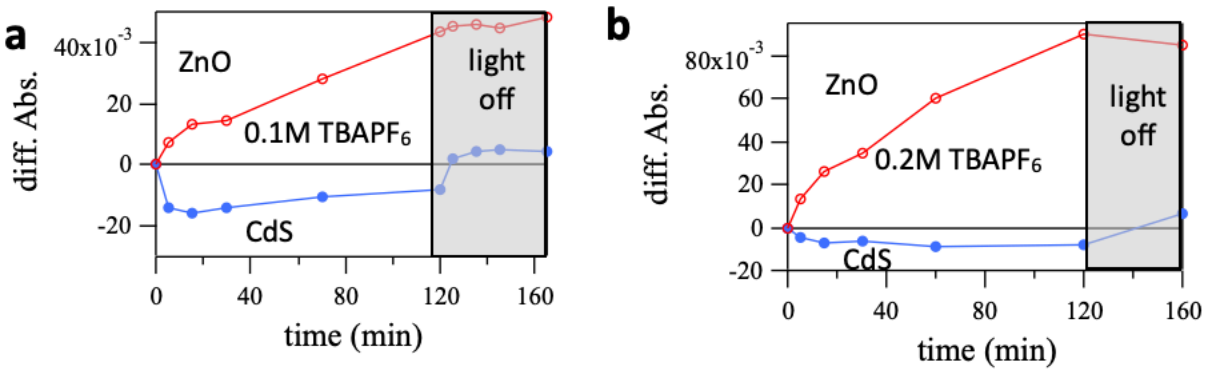

Figure 6.13 Electrolyte effect on electron transfer. Differential absorption of first excitonic feature of CdS (blue circles, line is a guide to an eye) and of NIR absorption of ZnO at 1600nm (red circles, line is a guide to an eye) during selective CdS photoexcitation in (a) 0.1M $TBAPF_6$ and (b) 0.2M $TBAPF_6$.

6.5 Summary

We observed charge transfer between CdS and ZnO nanocrystals upon CdS-selective photodoping. Spectroelectrochemistry was used for the measurement of band edge potentials in colloidal nanocrystals and showed that potentials of CdS/ZnO mixture is different from that of individual components. It is hypothesized that ligand-induced changes occur upon mixing of CdS and ZnO nanocrystals, resulting in a shift of the band edge potentials and enabling electron transfer. This hypothesis is explored experimentally and computationally in Chapter 7.

CHAPTER 7: CHARACTERIZATION OF THE CdS/ZnO SYSTEM

The occurrence of CdS-to-ZnO ET described in Chapter 6 indicates that relative BEPs of CdS and ZnO in the mixture must be different from that of individual components. We hypothesized that such a shift might occur due to ligand-induced changes on the NC surface, as the ligand environment changes upon mixing (**Figure 7.1**). Literature reports suggest a significant role of ligands in NC energetics and highlight opportunity to provide more facile charge transfer pathways via ligands (*35*, *56*, *109*, *111*, *116–119*). It is possible to displace native CdS ligands with those from ZnO (*120*). We explore this hypothesis experimentally by testing CdS NCs with different ligands and computationally by modeling the effects of NC-ligand interactions on CdS electronic properties.

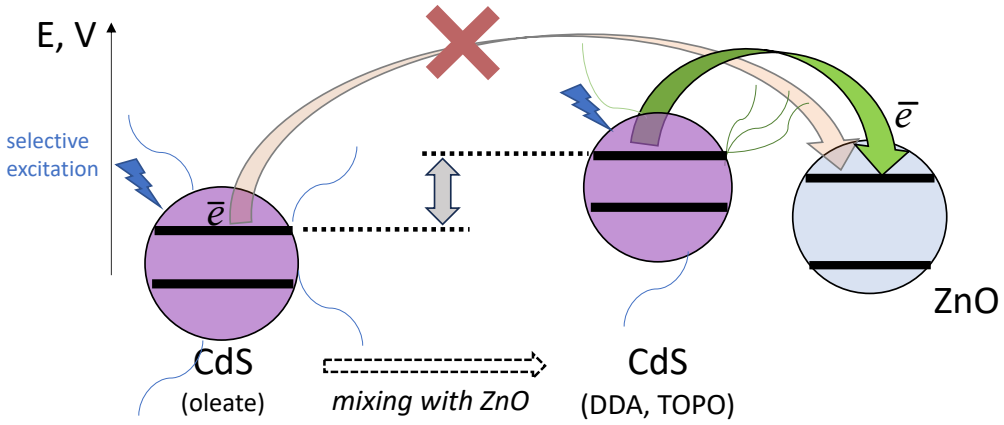

Figure 7.1 **Ligand-induced effects on band edge potential and CdS/ZnO electron transfer.** It is hypothesized that as-prepared CdS-oleate has a lower band edge potential in comparison to ZnO, which would prohibit electron transfer. Ligand-induced effects upon mixing of CdS with ZnO result in an increase of CdS potential to levels that support CdS-to-ZnO electron transfer.

7.1 Experimental investigation of the impact of ligands on NC band edge potential

The impact of ligands on NC band edge potential and electron transfer behavior was experimentally investigated on two model systems: (1) CdS NCs subjected to ligand treatment procedure and (2) CdSe NCs in CdSe/ZnO electron transfer mixture.

7.1.1 Ligand treatment of CdS NCs

Ligand treatment procedure on CdS NCs aimed to probe the possibility of BEP tuning upon CdS/ZnO mixing by altering CdS ligand passivation (**Figure 7.2**a). Since in the CdS/ZnO mixture oleic acid (OA), dodecylamine (DDA) and trioctylphosohine oxide (TOPO) are present, it was hypothesized that as-synthesized CdS NCs (OA passivated) experienced perturbations in surface chemistry from interaction with new ligands DDA, TOPO native to ZnO NCs. below shows relative BEPs measured by spectroelectrochemistry after ligand treatment of CdS NCs (**Figure 7.2**b), and after NC mixing (**Figure 7.2**c). This data shows that the treatment of OA-passivated CdS NCs with DDA and TOPO ligands could indeed raise CdS BEP to the level consistent with that observed in the CdS/ZnO NC mixture, providing support to our hypothesis.

As-synthesized CdS NCs were dried under N_2; used oil bath to melt DDA and TOPO (temperature 100°C); DDA treatment for 5min; after DDA treatment NCs were washed with EtOH/MeOH and resuspended in hexane; TOPO treatment for 10min; after TOPO treatment NCs were washed with EtOH and resuspended in THF; After ligand treatment procedure CdS NCs redissolved easily in THF and featured unperturbed optical properties (**Figure 7.3**).

We examined the impact of nanocrystal-ligand interactions on NC band-edge potential and electron transfer behavior. When surface passivation of CdS nanocrystals is altered through ligand treatment procedure, it is possible to observe shifts in band edge potential of CdS

nanocrystals. It is hypothesized that a similar shift in band edge potentials happens upon mixing of ZnO and CdS nanocrystals, which enables electron transfer in CdS/ZnO system.

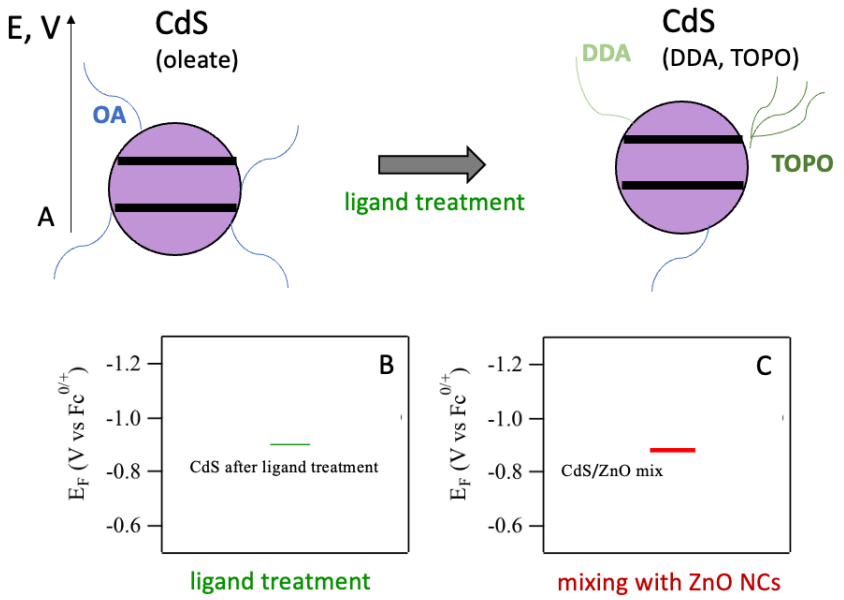

Figure 7.2 Band-edge potentials in CdS/ZnO NC mixture vs individual components. (A) Scheme illustrating CdS NC transformations during ether mixing with ZnO NCs or ligand treatment (bottom). (B) CdS NCs that underwent ligand (TOPO, DDA) treatment procedure show similar potential to the CdS/ZnO NC mix. (C) CdS/ZnO NC mix in the same experimental setup.

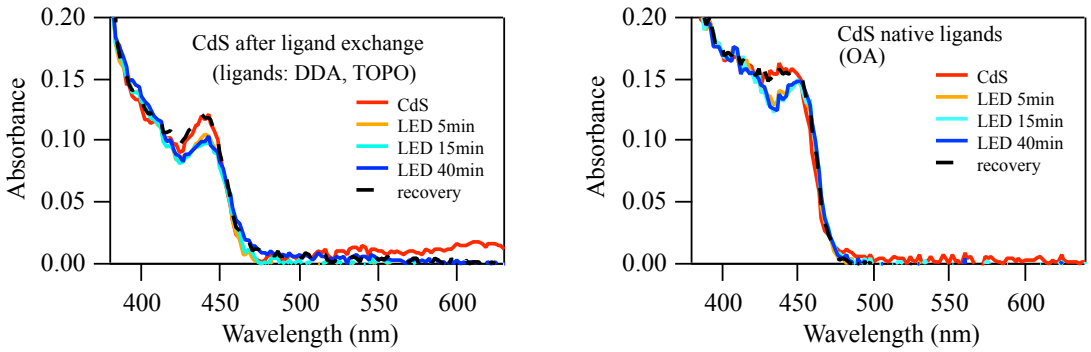

Figure 7.3 Characterization of CdS before and after ligand treatment procedure. Absorbance spectra of as-prepared NCs and NCs at different points of photodoping were measured.

7.1.2 Electron transfer behavior of CdSe NCs

CdSe NCs (OA passivated). Spherical QDs were synthesized using CdS procedure (*84*) by substituting S with Se. In brief, mixture of CdO, OA and ODE is heated to 300°C, TOP is added. After that the mixture of S in ODE is swiftly injected. Reaction should be quenched immediately after injection. Particles were washed with methanol and ethanol/acetone mixture.

CdSe NCs (OA, HDA, TOPO passivated). Spherical QDs were synthesized using known procedure (*121*). In brief, mixture of CdO, OA and ODE is heated to 280°C, TOP and HDA are added and heated at 300°C. After that the mixture of Se in TOP is swiftly injected. Reaction should be quenched 2 minutes after injection. About 16 ml of toluene is injected at 100°C. Particles were washed with methanol and ethanol mixture.

Conventional synthesis of CdSe NCs implies using TOPO and hexadecylamine (HDA). By synthesizing CdSe using OA (typical CdS synthesis) effect of passivating ligands on band-edge potentials can be spectroelectrochemically measured. Measured BEPs (**Figure 7.4**) suggest CdSe NCs (HDA and TOPO passivated) have higher CB and are expected to donate electrons to ZnO during ET. CdSe NCs (OA passivated) are not expected to participate in ET. Further analysis of absorption features of electronically doped (to circumvent potential changes after mixing) CdSe NCs during mixing with ZnO NCs indeed shows electron transfer from HDA and TOPO passivated NCs and no transfer from OA passivated NCs (**Figure 7.5**). This data confirms the hypothesis that NC BEP level can be raised by changing passivating ligands.

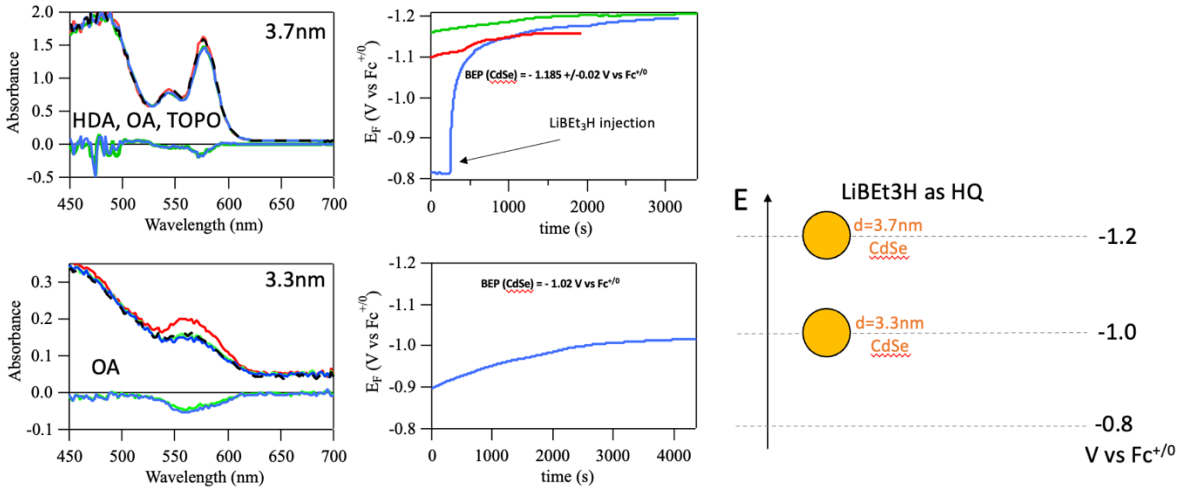

Figure 7.4 Spectroelectrochemical characterization of CdSe NCs. Measurements were performed on CdSe NCs obtained via different synthetic procedures to probe dependence of NC BEPs on ligand coverage. (Top left) Absorption spectra collected during NC photodoping ($LiEt_3BH$ as a HQ), in which 3.7nm HDA, OA, TOPO – coated CdSe NCs (red) are photoexcited with 430nm LED for 5min (green), 15 min (blue) and after recovery (black, dashed). The data show increase in absorption bleach during excitation. (Top right) Fermi level of CdSe NC solution measured during photodoping. Summary of 3 trials. The data show that BEP of CdSe NCs becomes more negative during photodoping. (Bottom left) Absorption spectra collected during NC photodoping ($LiEt_3BH$ as a HQ), in which 3.3nm OA – coated CdSe NCs (red) are photoexcited with 340nm LED for 5min (green), 15 min (blue) and after recovery (black, dashed). (Bottom right) Fermi level of CdSe NC solution measured during photodoping. The data show that BEP of OA – coated CdSe NCs is more positive than for HDA, OA, TOPO – coated CdSe NCs.

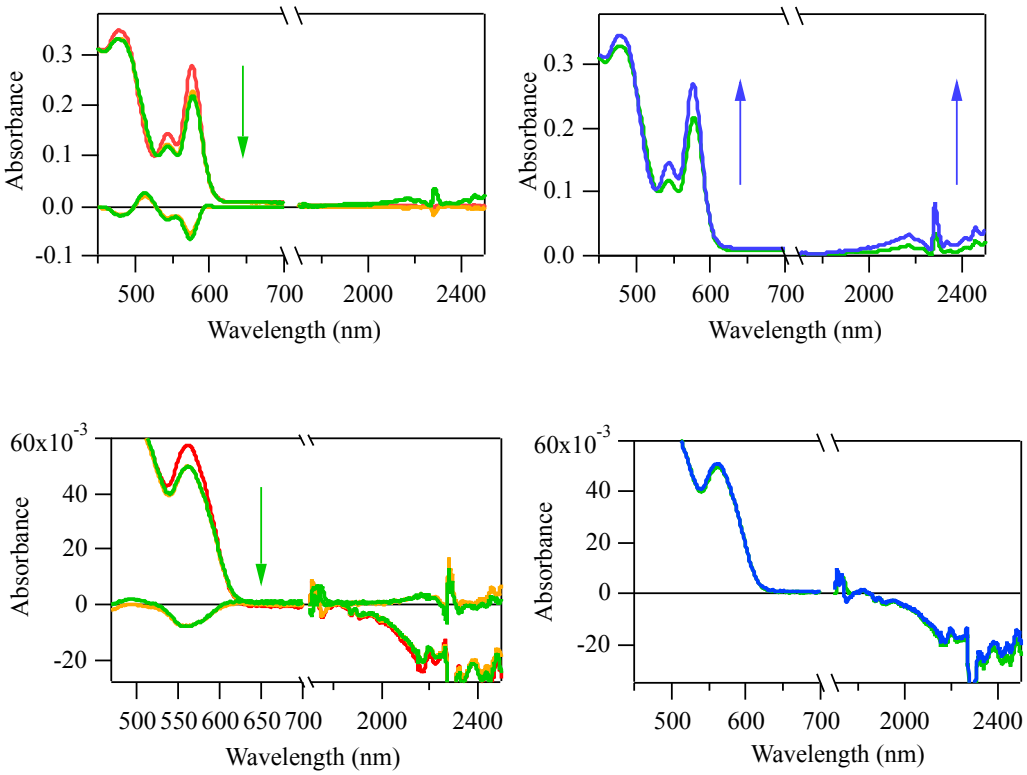

Figure 7.5 Electronic absorption spectra of CdSe NCs, collected after various durations of selective photoexcitation in airtight cuvette. (Top Left) Absorption spectra collected during NC photodoping, in which d = 3.7 nm CdSe NCs (red) are photoexcited with 430nm LED for 10min (gold), 30 min (green). The data show absorption bleach during photodoping with $LiEt_3BH$ indicative of electronic doping. (Top Right) ZnO NCs were added (blue) to the photodoped CdSe NCs (green) in air-free environment. The data show increase in absorption features of both CdSe and ZnO indicative of electron transfer. (Bottom Left) Absorption spectra collected during NC photodoping, in which d = 3.3 nm CdSe NCs (red) are photoexcited with 430nm LED for 10min (gold), 30 min (green). The data show absorption bleach during photodoping with $LiEt_3BH$. (Bottom Right) ZnO NCs were added (blue) to the photodoped CdSe NCs (green) in air-free environment. The data show no change in absorption features of both CdSe and ZnO indicative of lack of ET.

7.2 Computational framework for modeling of NC-ligand electronic properties

A computational framework was developed to investigate the scope and mechanisms of ligand effects on NC electronic properties.

7.2.1 Modeling of nanocrystal facets

Modeling NC-ligand interactions reveals the origin of complex effects observed experimentally in systems of interest (*37*, *56*, *109*, *122*).

To obtain slabs along particular NC facets bulk CdS CIF file was obtained from Materials Project [https://next-gen.materialsproject.org] and cut along 0001 , 1-101, 1-100 facets (**Figure 7.6**) known to be exposed during NC synthesis (*123*). Unit cells were redefined to expose the facets of interest by assigning new cell origin and a, b, c vectors, while retaining periodicity of the system. Transformation matrices were obtained in the process and were used to expose facets of wurtzite CdS nanocrystals. These transformation matrices can be used to expose 1-100 (Table 7.1) and 1-101 (Table 7.2) facets of any wurtzite structure starting with 0001 facet.

Cells were expanded in c directions to construct bulk-like region of the slab. Vacuum was added to new unit cells to accommodate ligand molecules on NC surface and approximate electrolyte in the NC mixture (**Figure 7.7**). Pseudo-H atoms (*124*) were used to passivate dangling bonds on the opposite side of the slab to retain the structure periodicity within the NC. Fractional charge of pseudo-H for each facet was chosen based on the structural data (number/nature of bonds each atom has on particular facet) and amount of valence electrons of atom: for example, for 0001 facet bottom sulfur atom (6 valence electrons) has 3 bonds with cadmium and 1 dangling bond. That means for each sulfur bond 6/4 = 1.5 electrons are contributed from sulfur. Each bond has 2 electrons total, so to compensate 1 dangling bond of sulfur 2-1=0.5 electrons are needed. So, pseudo-H with fractional charge of 0.5 *e* is used. To

confirm that pseudo-H passivation is appropriate, bond distances and angles in slab are compared to bulk (**Figure 7.8**).

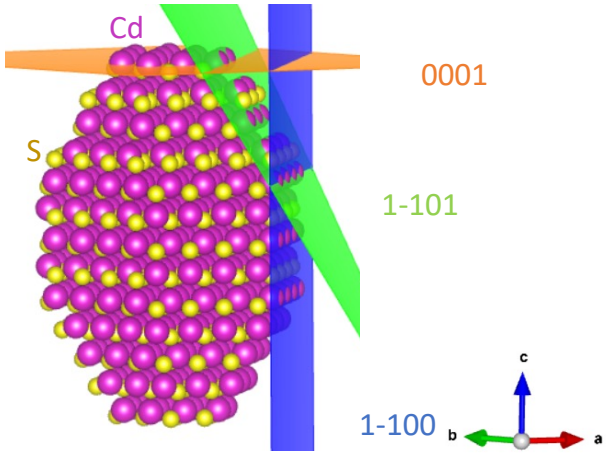

Figure 7.6 Facets of a spherical CdS nanocrystal. Lowest energy 0001 Cd-rich facet is shown in orange, 1-100 facet is shown in blue, 1-101 facet is shown in green.

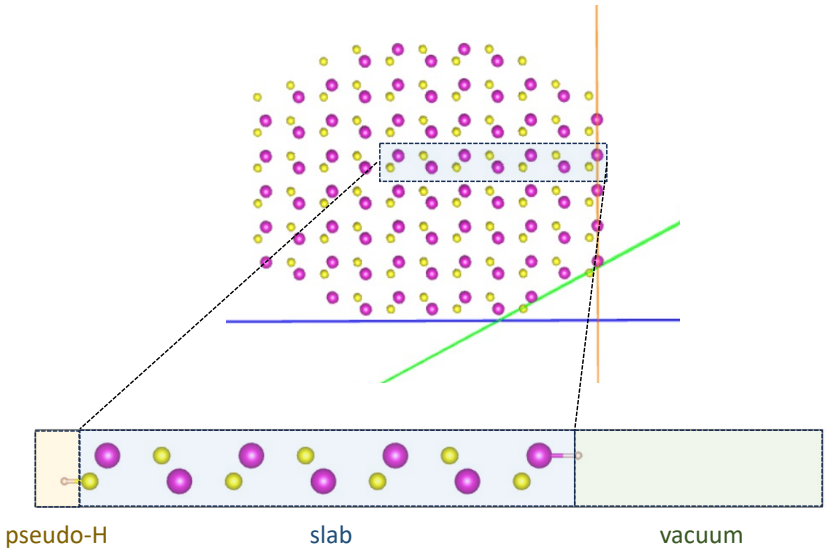

Figure 7.7 Structure of slab-vacuum unit cell. A CdS slab-vacuum unit cell used for DFT calculations consists of a slab region (multiple wurtzite unit cells expanded in c direction) and a vacuum region (which approximate solution and provides space for ligand placement). The opposite side of the slab is passivated with pseudo-hydrogen.

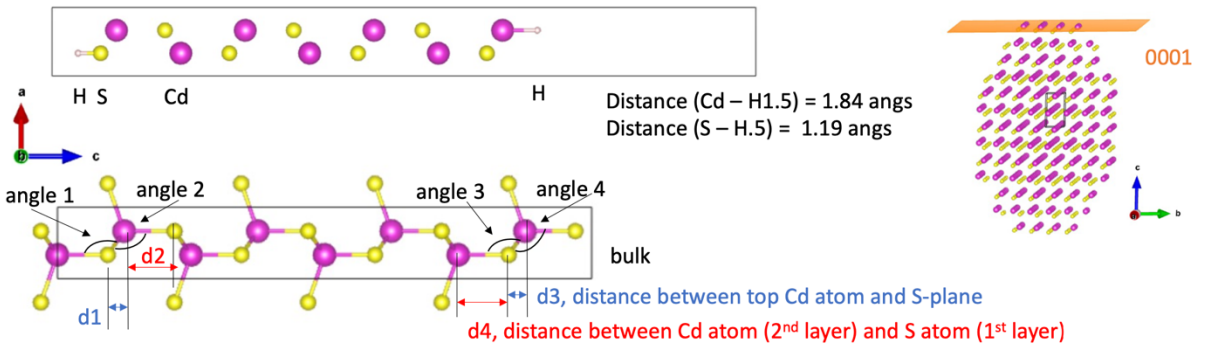

Bottom (S passivation)	bulk	0.5 pseudo-H
d1, angstroms	0.03	0.02
d2, angstroms	2.57	2.56
angle 1, degrees	109.2	108.6
angle 2, degrees	109.2	108.6

Top (Cd passivation)	bulk	1.5 pseudo-H
d3, angstroms	0.03	0.02
d4, angstroms	2.57	2.58
angle 3, degrees	109.2	108.9
angle 4, degrees	109.2	108.9

Figure 7.8 Validation of correct fractional charge of pseudo-H atoms for slab passivation. Relevant structural parameters were calculated for hydrogen-passivated CdS slab and compared to the values for bulk material.

Table 7.1 Transformation matrix to expose 1-100 facet from 0001

a	0	1	-1
b	0	-1	-1
c	-1	0	0

Table 7.2 Transformations to expose 1-101 facet from 1-100

	changing vectors in 1-100 facet				transforming to 1-101 facet, large cell				Transforming to 1-101 facet, smaller cell		
a	0	1	0		1	0	0		-1	0.5	0
b	0	0	1	⇒	0	2	-1	⇒	0	-0.5	0
c	1	0	0		0	1	2		0	0	1

7.2.2 Choosing an appropriate ligand model

Ligands commonly used in CdS synthesis (oleate, TOPO and DDA) were studied. To accurately model ligands acetate (CH_3COO-), methylamine (NH_2CH_3) and OPH_3 models were used. Starting geometries were taken from computational chemistry database. We show that our models show same potential shifts as those with additional CH_2 groups added, thus confirming that models accurately describe NC-ligand binding (**Figure 7.9**).

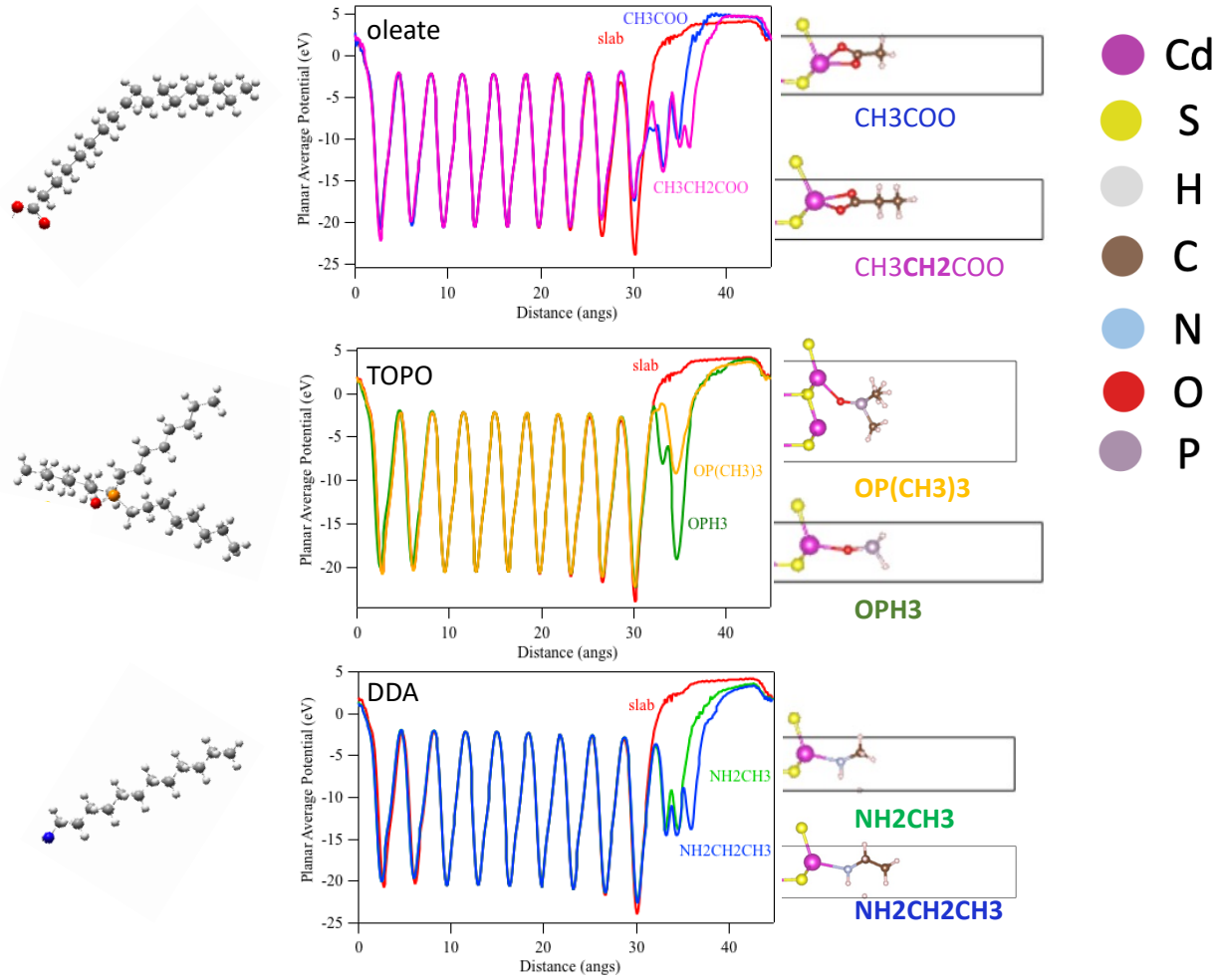

Figure 7.9 Planar average potentials of CdS slab with different ligand models. (top) A smaller CH_3COO was compared to a larger CH_3CH_2COO as a model of full-length oleate ligand (shown on the left). (middle) OPH_3 is compared to $OP(CH_3)_3$ as a model of TOPO. (bottom) NH_2CH_3 is compared to $NH_2CH_2CH_3$ as a model of DDA.

7.2.3 Global and local optimization of slab-ligand interfaces

Simulated annealing approach was used to find global energy minimum for the CdS-ligand slabs (*62*). By trying various MD conditions (**Figure 7.10**), we were able to find the most energetically favorable geometries for NC-ligand systems.

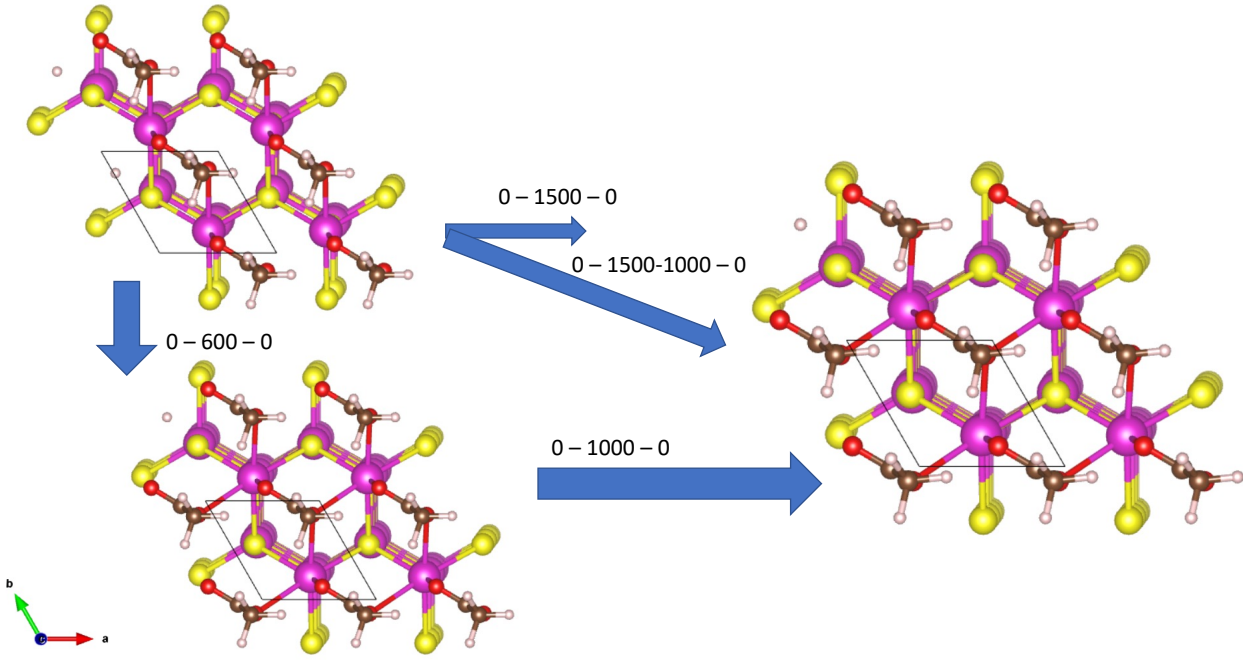

Figure 7.10 CdS slab-oleate geometry optimization via simulated annealing. Several heating/cooling conditions were applied to arrive at the global energy minimum for this system.

7.3 Applying computational framework to CdS slab-ligand system

The developed computational framework was applied to investigate CdS slab-ligand properties. Specifically, analysis of slab-ligand potentials, structural analysis of bonding in slab-ligand systems, density of states analysis of bonding in slab-ligand systems, and evaluation of total dipoles in slab-ligand systems were performed.

7.3.1 Analysis of slab-ligand potentials

To compare potentials in systems with different ligands, dipole correction was applied: offset in dipole is inserted at 74 Bohr (equals 39 Angstrom) to distinguish potentials at each facet making vacuum region flat and easy to evaluate. Calculated potential difference between the bulk region of the slab and vacuum region of each of the slabs for 0001 facet is shown in **Figure 7.11**. Other facets also show the biggest potential drop for slab-oleate case (Table 7.3). Differences in CdS-DDA potential drops for 1-100 and 1-101 facets compared to 0001 facet may originate from polarities of the facets: structural distortions in non-polar facets upon interactions with the ligand may increase interfacial dipoles and cause bigger potential drops. The bigger the potential drop – the lower the band-edge energy, because once the vacuum levels for all modeled systems are aligned – accounting for the shared electrolyte in the solution – the potential drop dictates the band offset. The trend in potential drops can be correlated with the spectroelectrochemical data, corroborating relative BEP positions obtained from the experiment.

Table 7.3 Calculated potential differences for different facets of CdS

Ligand / Facet	0001	1-100	1-101
oleate	7.39	11.39	10.31
TOPO	5.31	8.76	8.48
DDA	4.35	10.60	10.20

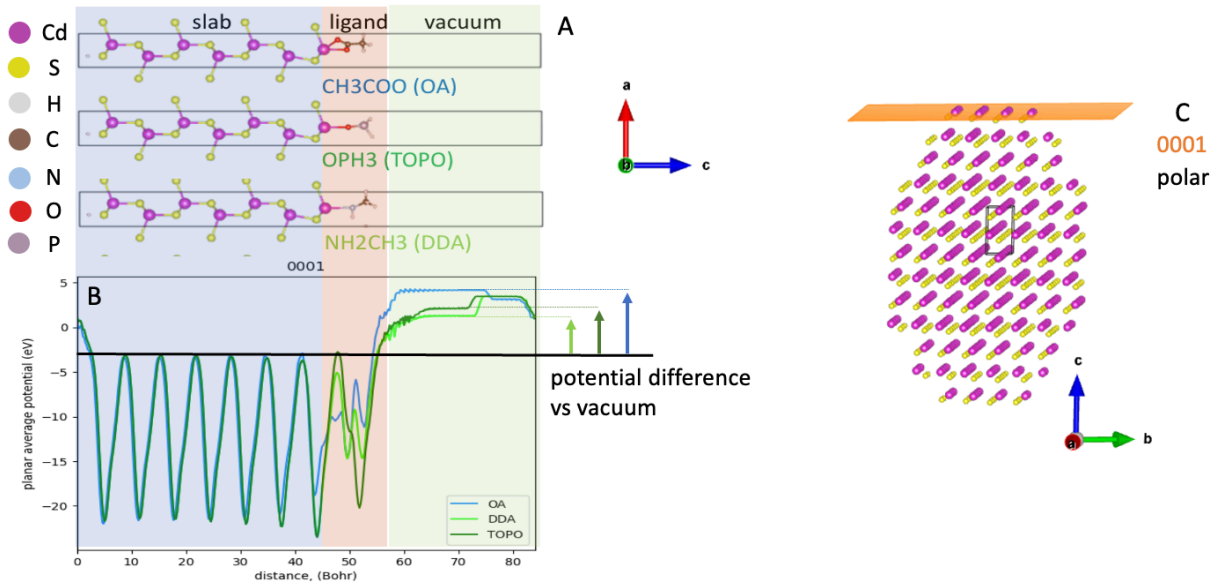

Figure 7.11 DFT modeling of ligand-induced potential differences for CdS slabs along 0001 facet. (A) Structure of modeled CdS-molecule slabs. The right side of the slab is passivated by adsorbed ligands (OA, DDA, TOPO) in vacuum, and the left side is passivated by pseudohydrogen atom. Ligand density is set at one molecule per surface Cd atom. (B) Planar-averaged electrostatic potentials of CdS slabs with different ligands. (C) Model of CdS NC. Lowest energy 0001 Cd-rich facet is shown in orange.

It should be noted that the magnitude of calculated potential offsets might depend on ligand coverage on the nanocrystal surface. Our calculations generally assume one-to-one ligand coverage, i.e. that each surface Cd atom is coordinated by 1 ligand. However, in experimental systems a lower ligand coverage is typically achieved. To test the effect of ligand coverage on the calculated potential in CdS-oleate system, we performed calculations with 1x4 (1 oleate per 4 Cd atoms), 2x4 (2 oleates per 4 Cd atoms), and 4x4 (one-to-one oleate-to-Cd) coverage (**Figure 7.12**). Modeling predicts that higher ligand coverage results in greater stabilization of the system, increasing potential offset and lowering the overall band edge potential.

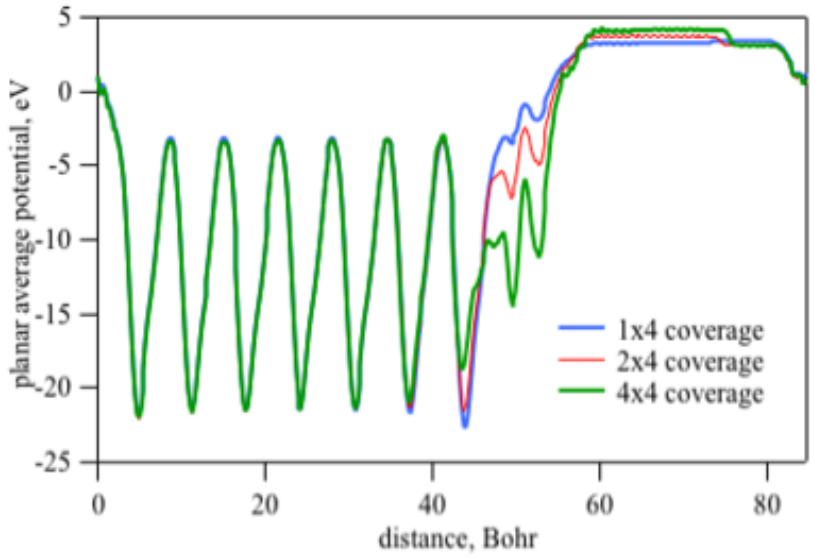

Figure 7.12 Ligand coverage dependent potential offsets in CdS-oleate. Potential offsets might vary in magnitude depending on the number of ligand molecules coordinated by the nanocrystal surface. Larger number of ligands in CdS-oleate system results in greater stabilization and larger potential offset.

7.3.2 Structural analysis of bonding in slab-ligand systems

Structural changes in slab-ligand systems also suggest that the nature of bonding in slab-oleate case is different from that in slab-DDA, and slab-TOPO (**Figure 7.13**a). Changes that top tetrahedron in CdS slab undergoes upon interaction with oleate, characterized by d1, d2 analysis are different from DDA, TOPO, and bare CdS surface (**Figure 7.13**b), suggesting that in case of interaction with oleate electrons are shared to larger extent. Slab-molecule bond (**Figure 7.13**c) in case of TOPO and DDA is longer than in oleate, indicating primarily electrostatic interaction. Binding energies allow to estimate bond strengths in slab-ligand systems (assuming oleic acid is fully dissociated, ligand coverage 1x1). Values for binding energies are obtained by subtracting formation energies of bare slab and ligand from formation energy of the bonded slab-ligand system: -239 kJ/mol in case of oleate and –25 and –8 kJ/mol for TOPO and DDA respectively, corroborating structural data. Compared to typical bond

strengths slab-oleate bond can be described as covalent-ionic and slab-DDA and slab-TOPO bond strengths are similar to hydrogen bonds, suggesting electrostatic interaction.

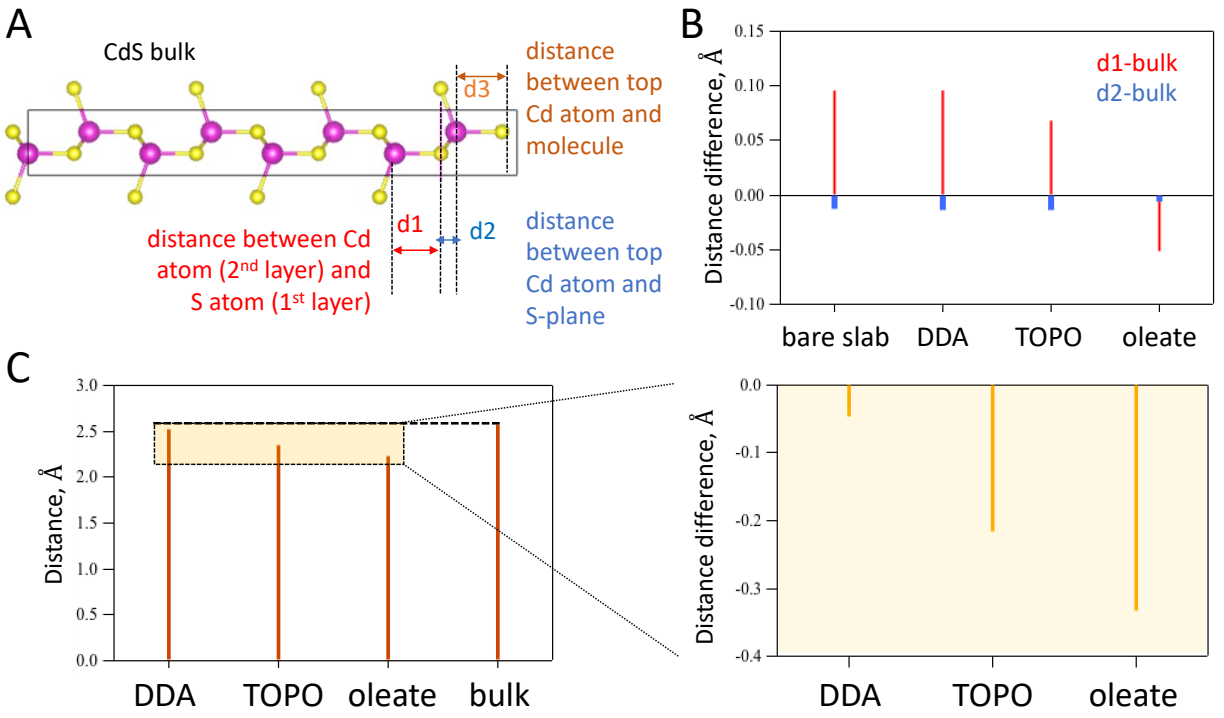

Figure 7.13 Structure analysis of bonding in CdS-molecule systems. Positive difference indicates bond elongation, negative difference reflects bond shortening. (A) Structure of modeled CdS bulk; distances used in analysis are indicated as d1, d2, d3. (B) Distance differences [d1-bulk], [d2-bulk] reflect deformation of top tetrahedron of CdS-molecule slabs in reference to corresponding distances in the bulk. (C) Distance d3 between slab-molecule and distance difference [d3-bulk] in reference to Cd-S bond length.

Several reports in literature suggest that impurities found in commercially available TOPO may bind to nanocrystal surface and change properties of the system (*125–127*). We have calculated binding energies for the following impurities: DOPO and OPA, because DOPO is reported to assist in QD growth (*127*) (CdS and ZnO nanocrystals used in this work are spherical), and OPA is reported to bind strongly to nanocrystal surface, though stabilizing nanorods (*125*, *126*). Our calculations show binding energies are very similar for TOPO and DOPO, suggesting

no preferential binding by impurity. It is difficult to assess if OPA played a significant role in CdS-ligand system, as all experiments with TOPO were conducted using 99% purity TOPO reagent, which has been shown to have OPA levels below detection limits (*127*). Further, calculated potential offset for deprotonated OPA is larger than that of TOPO and even oleate, which is inconsistent with experimental observations.

7.3.3 DOS analysis of bonding in slab-ligand systems

DOS analysis confirms structural observations (**Figure 7.14**). CdS slab-OA interaction happens in LUMO, electrons from slab are donated to OA, shifting Fermi level in the valence band. This data suggests more covalent nature of bonding compared to slab-DDA, and slab-TOPO, where interaction happens in HOMO, electrons from slab are not donated to molecule, thus Fermi level is in the conduction band. Thus, the more electrons are shared with the NC slab, the bigger the potential difference and the lower the BEP of the system.

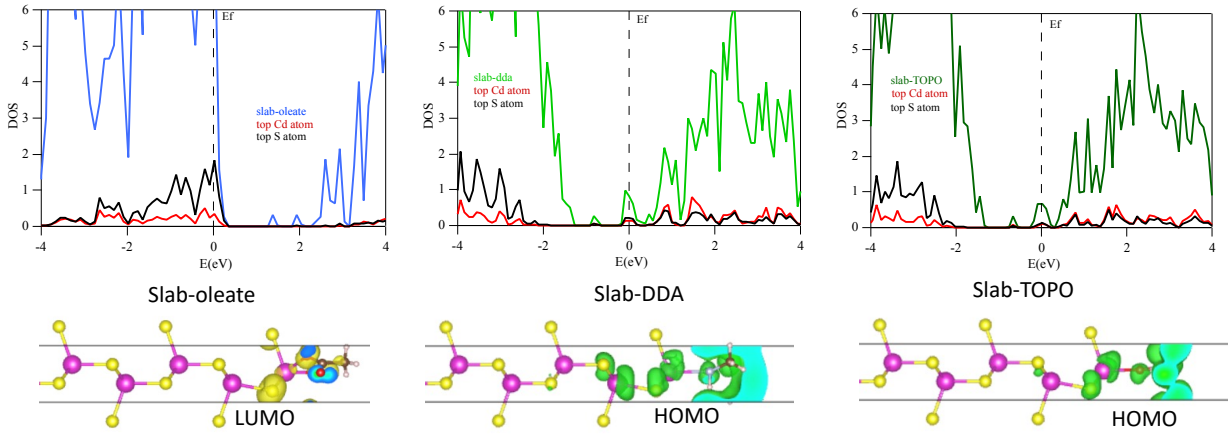

Figure 7.14 DOS analysis of bonding in CdS-molecule systems. DOS of CdS-ligand with respective slab molecular orbitals. This data shows p-doping (with molecule-slab interaction happening in LUMO) for CdS-OA system, and n-doping (with molecule-slab interaction happening in HOMO) for CdS-DDA and CdS-TOPO systems.

7.3.4 Effect of NC-ligand interaction on the total dipole of the system

NC-ligand interactions perturb dipoles in the system through structural and bonding changes, thus affecting electronic properties of the system. Here we use computational dipole analysis to gain insights into the origin of band edge potential shifts.

Total dipoles for the optimized slab-ligand systems were calculated from electron density difference using Synopsis QuantumATK (**Figure 7.15**) (*65*). The calculated dipole vectors, center mass, and dipole magnitude for the CdS-oleate, CdS-DDA, and CdS-TOPO systems are shown in Table 7.4. CdS slab-oleate exhibits largest dipole magnitude, followed by CdS-TOPO and CdS-DDA, consistent with relative magnitude of potential offsets calculated for these ligands.

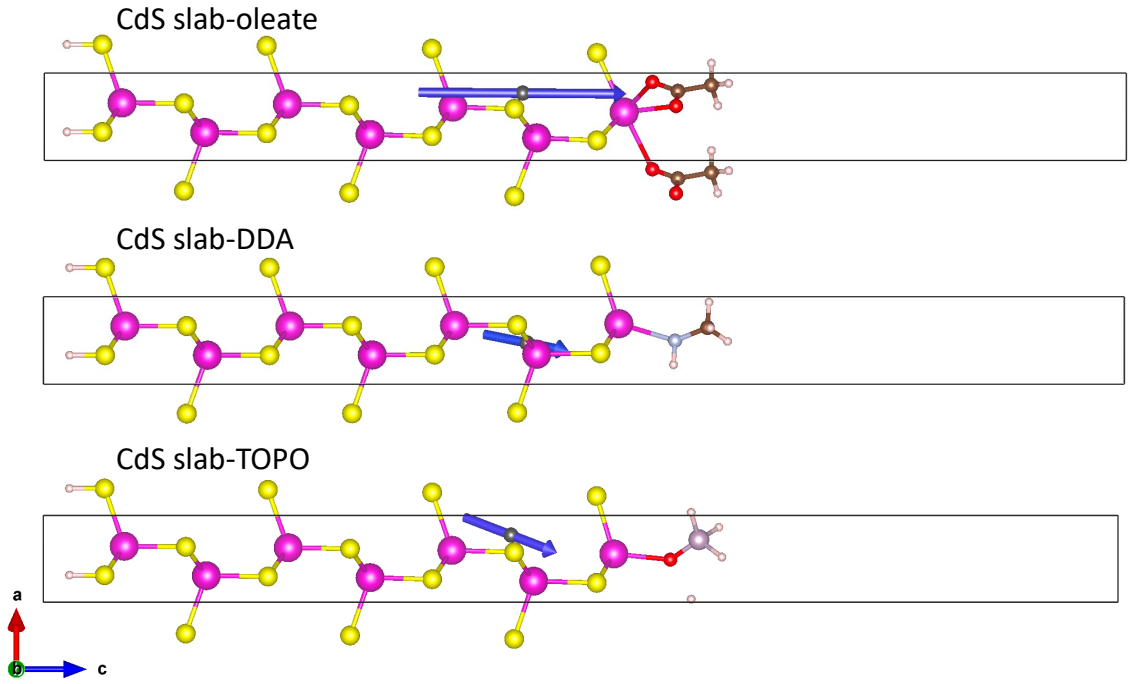

Figure 7.15 Dipole analysis in CdS slab-ligand system from charge density. Total dipole in CdS-oleate is larger than in CdS-DDA and CdS-TOPO. Cd atoms are shown on purple, S atoms in yellow, C atoms in brown, O atoms in red, N atoms in grey, P atoms in light grey, H atoms in white. Blue arrows show magnitude and direction of dipole anchored on charge center of mass.

Table 7.4 Position and magnitude of dipole in CdS-ligand system

System	Dipole vector (Bohr)			Center mass (Bohr)			Dipole (eBohr)
	x	y	z	x	y	z	
oleate	-0.31	0.42	8.16	14.03	12.51	37.59	8.17
DDA	-1.26	0.84	3.32	11.67	12.00	38.03	3.65
TOPO	-2.07	0.77	3.66	14.06	11.11	37.00	4.27

Difference in potential between two surfaces of the slab can also be indicative of total dipole in the system. Total dipoles for slab-ligand in reference to slab H-passivated surface (black) as well as for ligand molecules (blue) are plotted in **Figure 7.16**. For both DDA- and TOPO-passivated slabs, vacuum potential is lower than that of the hydrogen-passivated surface, whereas for CdS-oleate vacuum potential is higher. This indicates that for slab-oleate system a larger interface dipole must counteract the ligand to produce a greater magnitude of total dipole, suggesting that the slab-ligand interaction is stronger for slab-oleate system, again consistent with relative magnitude of potential offsets (**Figure 7.17**).

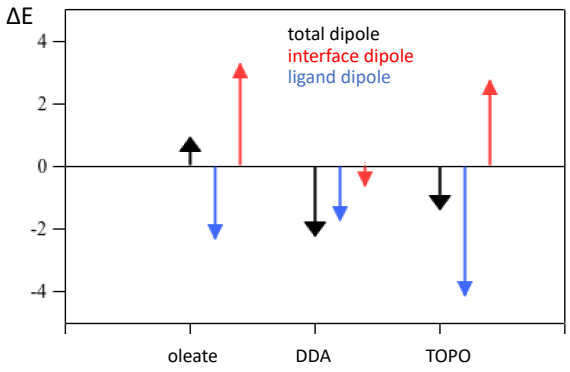

Figure 7.16 Dipole analysis in CdS slab-ligand system from differences in planar average potentials. Total dipole in CdS-oleate is different from CdS-DDA/TOPO. Total dipole is shown in reference to pseudo-H passivated facet of CdS slab.

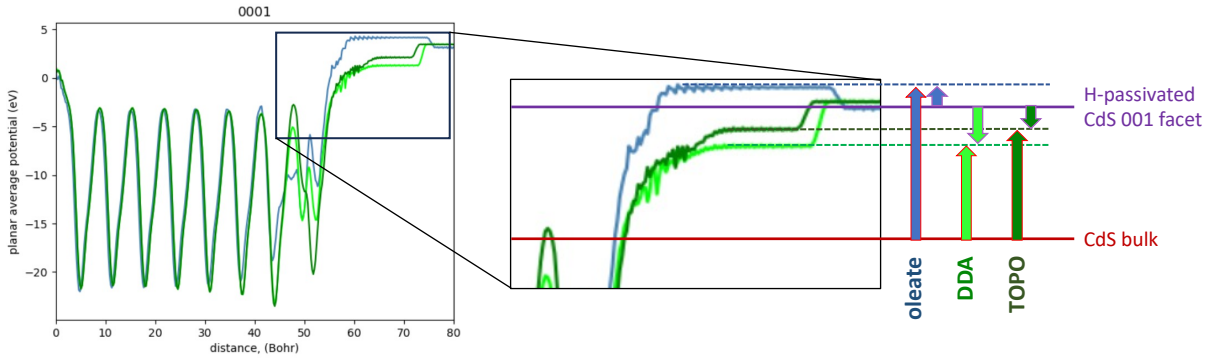

Figure 7.17 Effect of dipoles on potential offsets in CdS slab-ligand system. Dipoles are deduced from the difference of potentials between the vacuum region and H-passivated slab facet produced by dipole correction (highlighted in purple). Potential offsets reflective of band edge potentials are defined by the difference between the vacuum region and CdS slab (shown in red).

Observation from dipole analysis is consistent with the analysis of charge density distribution shown in **Figure 7.18**. Ligand–slab distance is the smallest for oleate, and the overlap of electron densities is the largest, suggesting stronger slab–ligand interaction in case of oleate. Smaller overlap in charge densities between slab and ligand in case of DDA and TOPO indicates a weaker slab-ligand interaction. As a result, Cd is moving closer to S plane of the slab to compensate for the lack of coordination by ligand.

7.4 Applying modeling results to CdS/ZnO charge transfer system

Experimental measurements of NC band-edge potential and modeling of NC slab-ligand potentials allowed us to gain an insight into the phenomena behind the unexpected charge transfer behavior in CdS/ZnO colloidal nanocrystal system. SpecEchem measurement of as-prepared CdS-oleate and ZnO-DDA/TOPO NCs before mixing indicated CdS having a lower potential than ZnO (**Figure 7.19**a). This result was consistent with the relative potential values obtained through modeling of CdS-oleate and ZnO-DDA slab-ligand systems (**Figure 7.19**b). Such

a configuration of potentials would be unfavorable to electron transfer from CdS to ZnO NCs (**Figure 7.19**c).

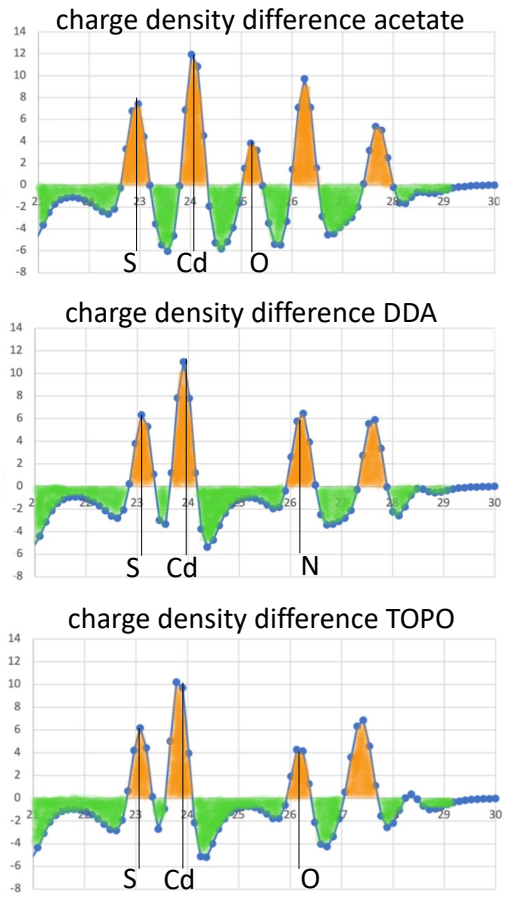

Figure 7.18 Total charge distribution in CdS slab-ligand system. Distribution of positive (orange) and negative (green) charge is shown across the slab-ligand interface.

In contrast to as-prepared CdS and ZnO NCs in separate solutions, a mixture of CdS and ZnO NCs in the same solution produced a shifted band-edge potential (**Figure 7.19**d). We hypothesized that a change in NC environment altered NC electronic properties. Specifically, we hypothesized that ligands present in ZnO NC solution interacted with CdS NCs. Therefore, we modeled the potential of CdS NC slab with ligands native to ZnO solution – DDA and TOPO. In both cases, CdS slab-ligand systems exhibited higher potential compared to ZnO-DDA (**Figure**

7.19e). This new configuration of relative CdS/ZnO band positions would enable electron transfer from CdS to ZnO NCs (**Figure 7.19**f).

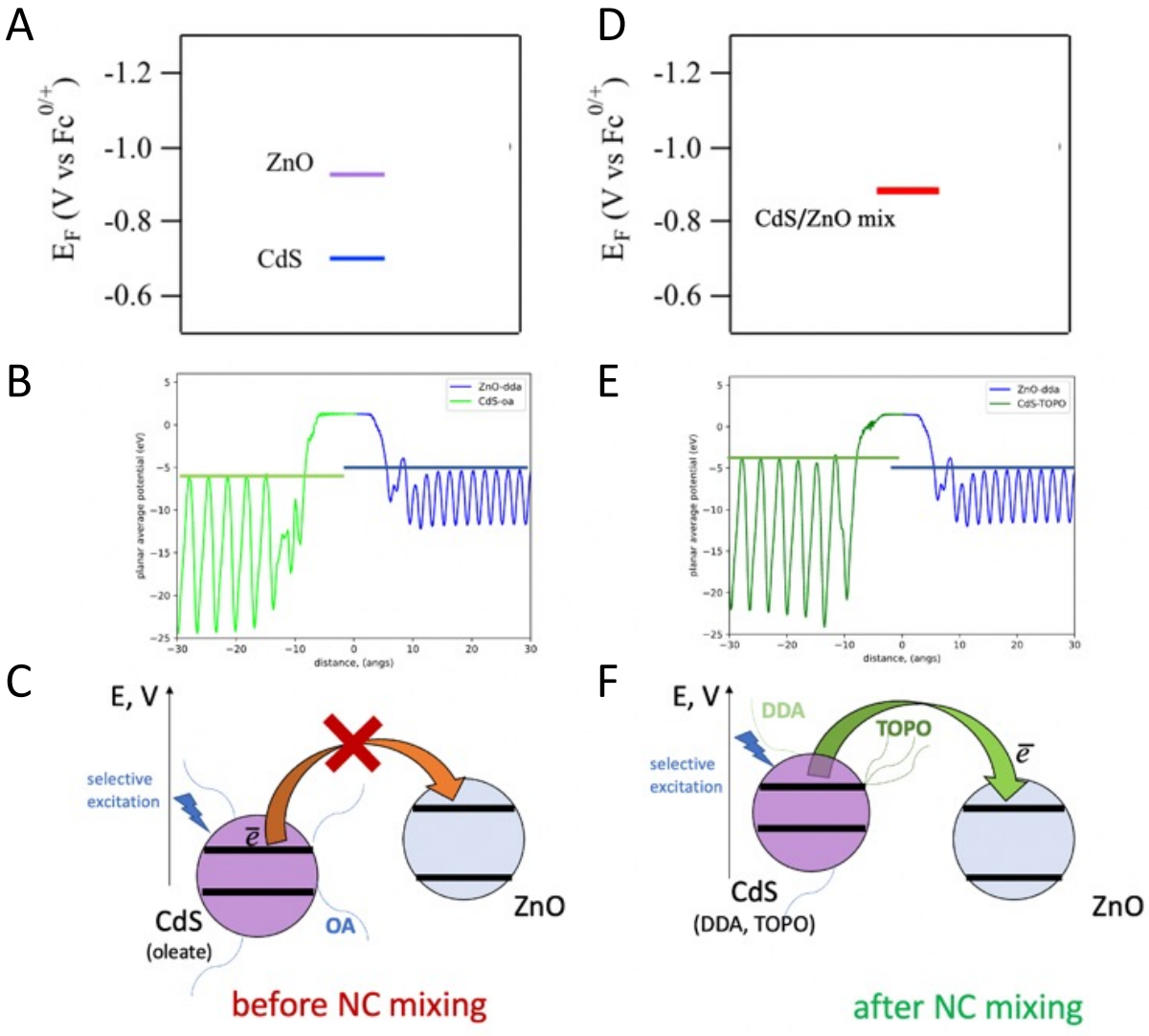

Figure 7.19 Electron transfer is enabled by changing the CdS NC environment in solution. (top) Spectroelectrochemical measurement of band edge potentials of CdS and ZnO nanocrystals before (a) and after (d) mixing. (middle) Modeled relative band-edge potentials of CdS (green) and ZnO (blue) with different ligand passivation: CdS-oleate (b) and CdS-TOPO (e). (bottom) Scheme illustrating CdS and ZnO NC band-edge positions based on modeling data presented in middle panels.

7.5 Summary

We present a complex nanocrystal system, where we observed electron transfer from CdS to ZnO NCs despite unfavorable BEPs of NCs prior to mixing. We hypothesize that ET is enabled by changing the NC environment upon mixing. DFT modeling performed on CdS slabs with different ligand passivation revealed differences in the nature of nanocrystal-ligand bonding based on the potential, structure, and density of states analysis, explaining the experimental observations. We show bigger potential drop for slab/vacuum region in case of surface passivation of as-prepared CdS with oleate ligand compared to that with dodecylamine and tryoctylphosphine ligands present in the nanocrystal mixture with ZnO. Consistent trends are calculated for the two main facets of CdS nanocrystals. Modeling reveals how more covalent nature of slab-oleate bond dictates larger extent of electron sharing between slab and ligand, resulting in smaller slab-molecule distances, stronger binding energies, shift in Fermi level and change in band-edge potentials. A more electrostatic nature of CdS nanocrystal passivation with tryoctylphosphine oxide ligands or dodecylamine ligands present in the CdS/ZnO nanocrystal mixture yields a smaller total dipole in the system (in reference to bulk region of the NC slab), increasing the band-edge potential of CdS in comparison to the native oleate ligands. The developed computational approach opens an opportunity to predict, through modelling, effects of ligand-nanocrystal interactions on band edge potentials in complex nanomaterial systems.

CHAPTER 8: EMERGING APPLICATIONS OF THE COMPUTATIONAL FRAMEWORK FOR MODELING OF NANOCRYSTAL-LIGAND INTERACTIONS

The computational framework described in this dissertation is potentially generalizable to any crystalline system with known exposed facets and surface passivation. This provides a unique opportunity to predict energetics and properties of a wide variety of materials to support and explain experimental evidence and even characterize properties that might be challenging to measure experimentally. For example, we started applying this framework to predict electron transfer behavior in CdSe/ZnO nanocrystal mixture, expand the library of surface molecules used to passivate the NCs, investigate surface passivation in diamond, nanocrystal-ligand interactions in bornite, and elpasolite stability. Chapter 8 presents results of these pilot projects and outlines the scope of potential applications.

8.1 Electron transfer behavior in CdSe/ZnO nanocrystal system

The developed computational framework was applied to characterize wurtzite CdSe-ligand properties and predict the effects of different ligands on NC band edge potential, structure, and binding energies in analogy to modeling performed for CdS (described in Chapter 7). CdSe slab was constructed from bulk wurtzite CdSe crystal (CIF file was obtained from Materials Project [https://next-gen.materialsproject.org]), and ligands were placed on 0001 facet (*128*). Simulated annealing was performed to optimize the structure. Even though CdS and CdSe are isostructural, replacing S with Se in the optimized CdS-ligand structure (to obtain CdSe-ligand) results in higher energies compared to simulated annealing approach on CdSe slab-ligand,

highlighting the need to construct and optimize each NC slab-ligand system starting with the reference bulk crystal structure.

Potential offset was calculated for CdSe slab covered with oleate, HDA, or TOPO ligands (**Figure 8.1**). Similar to CdS results, a bigger potential offset is obtained with oleate ligand, consistent with experimental results (shown in Chapter 7): band edge potential of oleate-covered nanocrystal was lower than that of HDA-, TOPO- covered nanocrystal measured by spectroelectrochemistry.

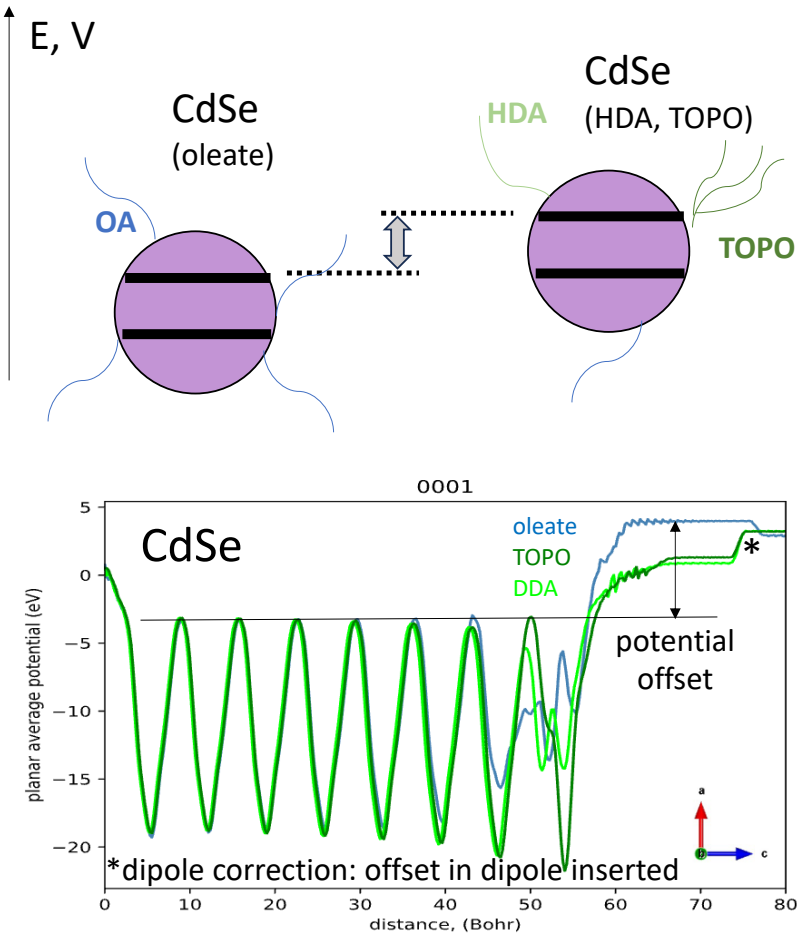

Figure 8.1 **Potential offset calculated for CdSe slab with different ligands.** Potential offset for oleate-covered CdSe slab is bigger than that for HDA-, and TOPO-covered slabs, predicting a lower band edge potential for oleate-covered nanocrystals.

8.2 Going beyond experimentally measured ligands: expanding library of surface molecules

The developed computational framework allows to generalize the characterization of NC-ligand interactions and predict the effects of inorganic ligands, such as chloride and fluoride, on nanocrystal electronic properties based on bonding nature between ligand and top atoms on NC surface. In **Figure 8.2** we show how electronegativity difference (changing the nature of Cd-ligand bond) affects potential drops allowing to tune band edge potential. Electronegativity increases from H to Cl to F, suggesting stronger bonding than in slab-oleate case. Stronger bonding results in better nanocrystal stabilization (bigger potential offset) and more efficient electron transfer to these materials. Also these results highlight the role of interfacial dipoles on determining total dipoles, since in these systems ligand dipole is 0.

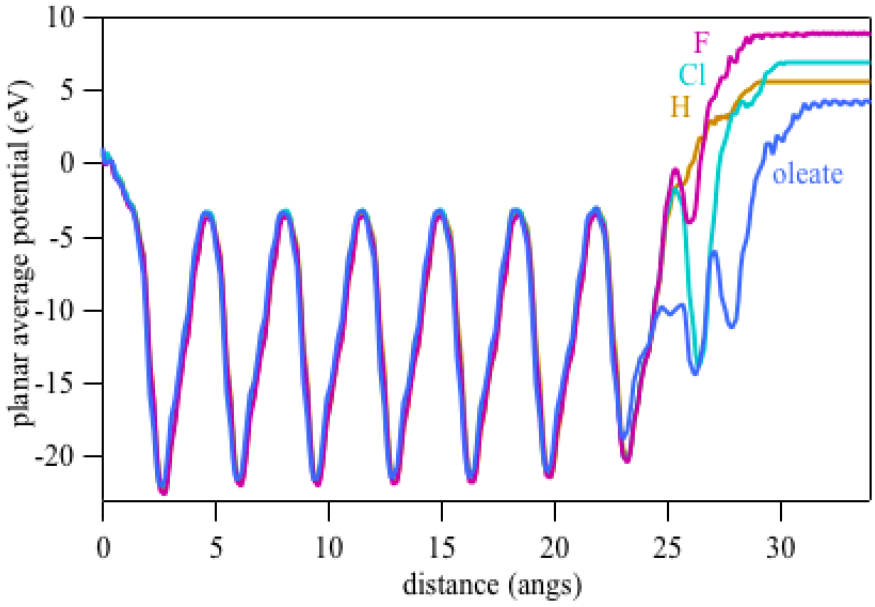

Figure 8.2 Predicting NC band edge potentials from modeling inorganic ligands. Planar average electrostatic potentials of CdS slabs with ligands H, Cl, and F are shown in comparison to slab-oleate for 0001 facet.

8.3 Effects of surface passivation on properties of diamond

Diamonds with modified surfaces are promising materials for quantum network technologies (*129*). Changes in surface termination result in lower electron affinities and change band bending (*130*, *131*). We applied our computational framework to examine the impact of diamond surface passivation with H, Be, Mg, Ca. We constructed diamond slabs passivated with H, Be, Mg, or Ca on one side and O on the opposite side (as a reference) and applied DFT modeling to predict band edge potential shifts emerging from each surface passivation motif (**Figure 8.3**).

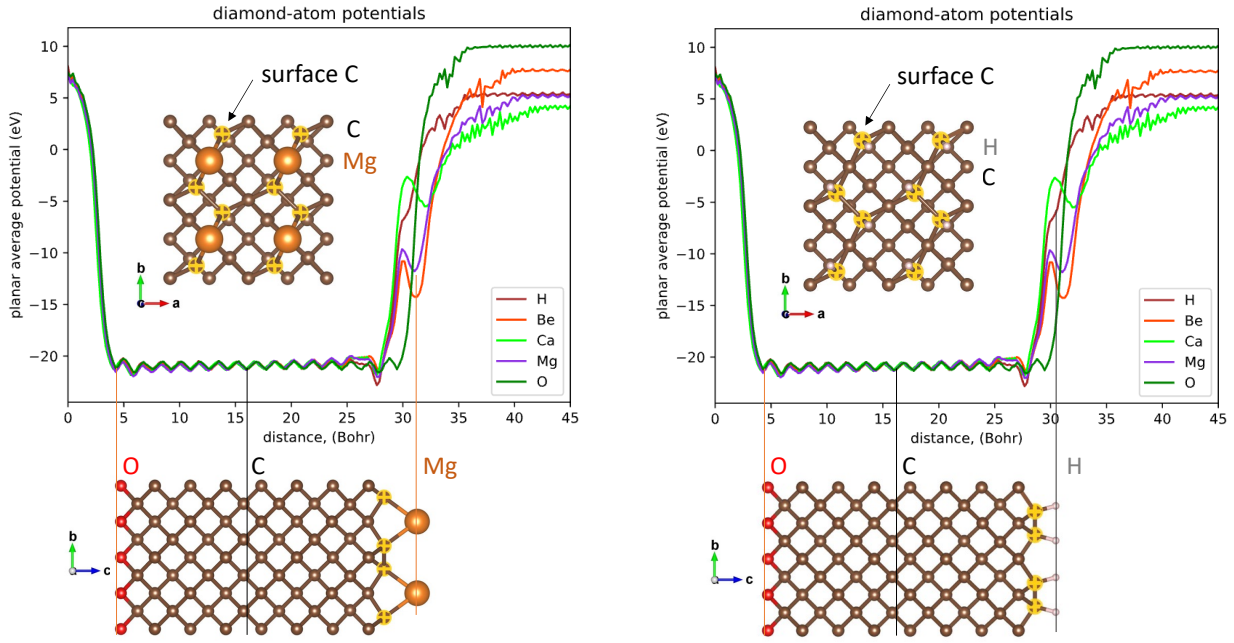

Figure 8.3 **Modeling of diamond slab.** Slab was passivated with O on the left side and H, Be, Ca, Mg, or O on the right (vacuum) side for calculation of potentials. Planar average potential is shown for diamond slab with different surface passivation. (left) Example structure of diamond passivated with O and Mg. O atoms are shown in red, Mg in orange, C in brown. (right). Example structure of diamond passivated with O and H. O atoms are shown in red, H in grey, C in brown. Different ligands yield different reconstruction of surface carbon atoms.

Ca-passivated surface featured the largest predicted band edge potential shift compared to the O-passivated reference; however, due to large size, Ca atoms had weaker surface binding energy, which would likely lead to an unstable interaction. H- and Mg-passivated slabs (2x1 reconstruction) were determined to be most promising candidates for band edge potential tuning in diamond.

8.4 Impact of ligands on phase stability

The developed computational framework can also be applied to study the impact of ligands on phase stability. As a proof-of-principle, we examined the impact of nanocrystal-ligand interactions on stability of bornite (Cu_2FeS_2) and elpasolite (Cs_2AgBiI_6) structures.

Bornite is a tunable material with properties depending on iron content (*54*). It has been experimentally observed that stability of bornite nanocrystals depends on the surface ligands used during synthesis. Thus, we modeled bornite Cu_2FeS_2 slab passivated with common ligands – oleylamine (OAM) or 1-dodecanethiol (DDT) – to computationally assess the effects of these ligands on bornite stability. DFT modeling shows significant reconstruction of the nanocrystal surface for both ligands compared to the bare reconstructed surface (**Figure 8.4**). Formation energy of OAM-passivated bornite (-225.6 eV) is substantially lower than that of DDT-passivated bornite (-217.2 eV), suggesting that bornite structure is more stable with OAM passivation.

Iodide elpasolites are promising materials for optoelectronic applications (*132*). We apply our computational approach to characterize stability of Cs_2AgBiI_6 and show that in bulk this structure is not stable. However, Cs_2AgBiI_6 has been experimentally obtained as a nanomaterial, suggesting that ligands could play an important role in stabilization of elpasolite structure. Our calculations predict tetragonal structure to be more stable than cubic structure, consistent

with experimental data. Modeling of elpasolite tetragonal and cubic structures is shown in **Figure 8.5.**

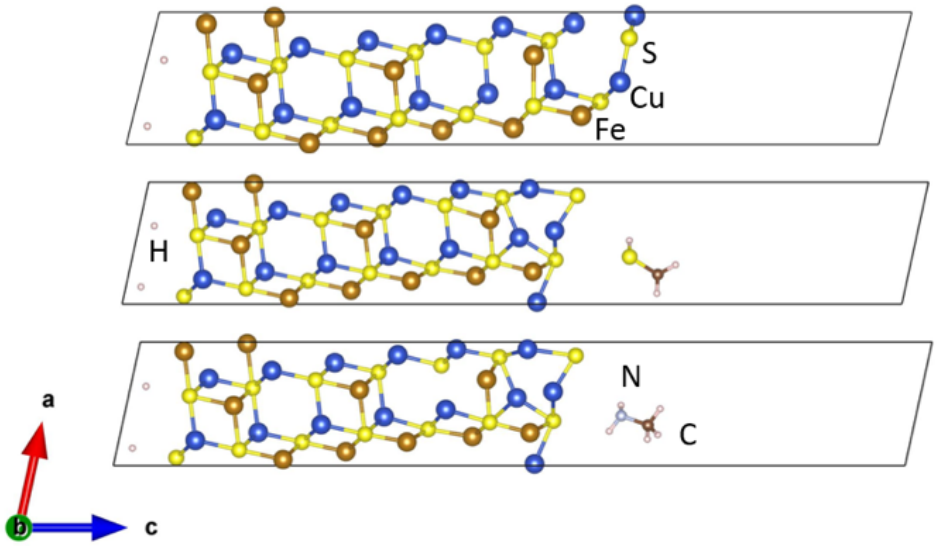

Figure 8.4 Modeling of bornite. (top) reconstructed bornite surface; (middle) bornite – DDT system; (bottom) bornite – OAM system.

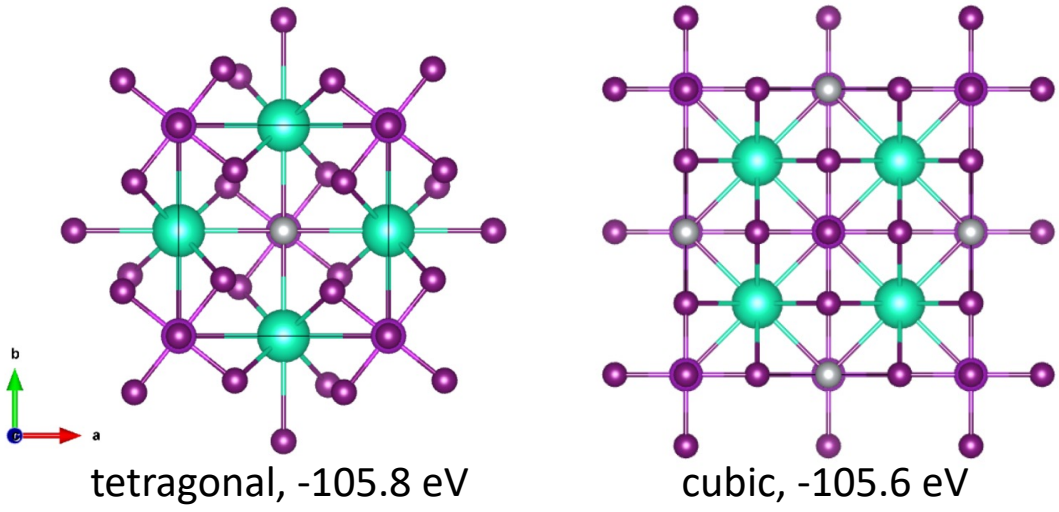

Figure 8.5 Modeling of elpasolite. Tetragonal and cubic structures are shown, with calculated formation energies indicated under each structure. Cs is shown in teal, Ag in grey. Large purple atoms are Bi, small purple atoms are I.

To evaluate stability of elpasolite structure in bulk, formation energies for elpasolite and products of its decomposition were calculated (Table 8.1). Decomposition reaction is shown below:

$$2Cs_2AgBiI_6 = Cs_3Bi_2I_9 + 2AgI + CsI$$

Table 8.1 Formation energies of elpasolite and its decomposition products

Cs_2AgBiI_6	CsI	$Cs_3Bi_2I_9$	AgI
-52.91134834	-3.53387154	-76.16248181	-19.29831521

8.5 Summary

Future applications of the developed computational framework could include a variety of complex nanocrystal-ligand systems due to its generalizability to potentially any crystalline structure with known facets and ligands. Here, we explore properties of several different materials and compare computational results to experimental evidence. We show that ligands could have a major effect on band edge potential of CdSe NCs, similar to that described for CdS NCs (in Chapter 7). We further show that inorganic ligands could provide an even greater stabilization of CdS NCs in comparison to organic ligands. Modeling confirms that surface modifications in diamond change its electronic structure and result in reconstruction of the top carbon layer. Finally, we explore stability of bornite and elpasolite structures and provide initial computational support to experimental observations. The proof-of-principle studies demonstrate the wide utility of the developed computational framework.

CHAPTER 9: DISSERTATION SUMMARY

This dissertation aims to gain a better understanding of the effects of surface interactions on electronic properties of semiconductor nanocrystals, explore the emergence of supercapacitance, and examine the effects of band engineering on electron transfer in complex nanocrystal systems. To achieve this aim, this dissertation combines experimental methods for nanocrystal synthesis and characterization with a computational framework for modeling of the nanocrystal-ligand interfaces. Specifically, we develop and employ experimental and computational approaches to study electronic structures of colloidal Cu:ZnSe, PbS, CdS, CdSe, ZnO nanocrystals. Further, we explore emerging applications of the developed computational framework to expand the library of surface molecules used to passivate the NC, and investigate such systems as diamond surface passivation, nanocrystal-ligand interactions in bornite and chalcopyrite NCs, and elpasolite stability.

We report synthetic procedure that yields successful doping of ZnSe NCs with large amounts of Cu and identify further parameters for procedure optimization.

Spectroelectrochemical measurements of the band-edge potentials of colloidal PbS (d = 5.7 nm) and CdS (d = 5.8 nm) NCs result – as anticipated from comparison of NC films and bulk materials – in values of band-edge potentials of colloidal NCs different from bulk and films. We confirm that for colloidal PbS NCs – in agreement with literature for films – the band-edge potential can be tuned by hundreds of mVs with simple ligand exchange treatments. This data supports the hypothesis that band-edge potentials of colloidal NCs differ from band-edge

potentials of NCs in films and bulk materials, because of the greater influence of dynamic surface chemistry.

ZnO proves to be a versatile material for energy storage due to large capacity for electron accumulation. We have further observed an emergence of supercapacitance in ZnO nanocrystals upon electronic doping under the following conditions: aluminum doping, photodoping in the presence of $LiEt_3BH$, non-spherical NC morphology, changes in supporting media.

SpecEchem measurements of CdS NCs reveal that the conduction band of CdS is more positive than that of CdSe and ZnO, contrary to what is expected from bulk. Interestingly, we observe simultaneous electronic doping in mixtures of CdS and ZnO nanocrystals under CdS-selective photochemical doping conditions, indicating that an electron transfer occurs from CdS to ZnO despite band edge potential of as-prepared CdS nanocrystals being lower than that of ZnO nanocrystals. This unique system has allowed us to study the effects of surface chemistry on properties of inter-NC electron transfer and Fermi level equilibration. A series of experiments has revealed that a shift in CdS band edge potentials happens upon mixing of ZnO and CdS nanocrystals due to change in total dipole caused by new ligands present in the mixture, thus enabling CdS-to-ZnO electron transfer.

Modeling reveals how strong nanocrystal-ligand interaction dictates larger extent of electron sharing between slab and ligand, resulting in smaller slab-molecule distances, stronger binding energies, shift in Fermi level and change in band-edge potentials. These findings explain experimental results and open an opportunity to generalize modeling of this phenomenon. The developed computational framework can, thus, be employed to predict the effects of ligand-nanocrystal interactions on nanocrystal properties and resulting behavior of complex nanomaterial systems.

Overall, this work provides new insights into properties of colloidal semiconductor nanocrystals with excess charge carriers and informs rational design and tuning of electronic properties for next-generation nanomaterials and applications.

Literature Cited

1. P. Zrazhevskiy, M. Sena, X. Gao, Designing multifunctional quantum dots for bioimaging, detection, and drug delivery. *Chem. Soc. Rev.* **39**, 4326–4354 (2010).

2. R. Bera, A. Dutta, S. Kundu, V. Polshettiwar, A. Patra, Design of a CdS/CdSe Heterostructure for Efficient H_2 Generation and Photovoltaic Applications. *J. Phys. Chem. C*. **122**, 12158–12167 (2018).

3. W. Li, F. Jäckel, Size-controlled electron transfer rates determine hydrogen generation efficiency in colloidal Pt-decorated CdS quantum dots. *Nanoscale*. **10**, 16153–16158 (2018).

4. W. Li, G. O'Dowd, T. J. Whittles, D. Hesp, Y. Gründer, V. R. Dhanak, F. Jäckel, Colloidal dual-band gap cell for photocatalytic hydrogen generation. *Nanoscale*. **7**, 16606–16610 (2015).

5. A. Li, T. Wang, C. Li, Z. Huang, Z. Luo, J. Gong, Adjusting the Reduction Potential of Electrons by Quantum Confinement for Selective Photoreduction of CO_2 to Methanol. *Angew. Chem. Int. Ed.* **58**, 3804–3808 (2019).

6. N. Meir, I. Pinkas, D. Oron, NIR-to-visible upconversion in quantum dots *via* a ligand induced charge transfer state. *RSC Adv.* **9**, 12153–12161 (2019).

7. W. Wang, M. Zhang, Z. Pan, G. M. Biesold, S. Liang, H. Rao, Z. Lin, X. Zhong, Colloidal Inorganic Ligand-Capped Nanocrystals: Fundamentals, Status, and Insights into Advanced Functional Nanodevices. *Chem. Rev.* **122**, 4091–4162 (2022).

8. M. A. Boles, D. Ling, T. Hyeon, D. V. Talapin, Erratum: The surface science of nanocrystals. *Nat. Mater.* **15**, 364–364 (2016).

9. A. P. Alivisatos, Semiconductor Clusters, Nanocrystals, and Quantum Dots. *Science*. **271**, 933–937 (1996).

10. A. P. Alivisatos, Perspectives on the Physical Chemistry of Semiconductor Nanocrystals. *J. Phys. Chem.* **100**, 13226–13239 (1996).

11. A. M. Smith, S. Nie, Semiconductor Nanocrystals: Structure, Properties, and Band Gap Engineering. *Acc. Chem. Res.* **43**, 190–200 (2010).

12. H. A. Nguyen, G. Dixon, F. Y. Dou, S. Gallagher, S. Gibbs, D. M. Ladd, E. Marino, J. C. Ondry, J. P. Shanahan, E. S. Vasileiadou, S. Barlow, D. R. Gamelin, D. S. Ginger, D. M. Jonas, M. G. Kanatzidis, S. R. Marder, D. Morton, C. B. Murray, J. S. Owen, D. V. Talapin, M. F. Toney, B. M. Cossairt, Design Rules for Obtaining Narrow Luminescence from Semiconductors Made in Solution. *Chem. Rev.* **123**, 7890–7952 (2023).

13. E. Roduner, Size matters: why nanomaterials are different. *Chem. Soc. Rev.* **35**, 583 (2006).

14. D. Ung, I. A. Murphy, B. M. Cossairt, Designing nanoparticle interfaces for inner-sphere catalysis. *Dalton Trans.* **49**, 4995–5005 (2020).

15. H. H. Ripberger, S. M. Harvey, B. M. Cossairt, Editorial: The molecular underpinnings of nanoscale semiconductor synthesis. *Front. Nanotechnol.* **5** (2023) (available at https://www.frontiersin.org/articles/10.3389/fnano.2023.1229232).

16. F. Y. Dou, S. M. Harvey, K. G. Mason, M. K. Homer, D. R. Gamelin, B. M. Cossairt, Effect of a redox-mediating ligand shell on photocatalysis by CdS quantum dots. *J. Chem. Phys.* **158**, 184705 (2023).

17. H. Larson, B. M. Cossairt, Indium–Poly(carboxylic acid) Ligand Interactions Modify InP Quantum Dot Nucleation and Growth. *Chem. Mater.* **35**, 6152–6160 (2023).

18. D. A. Henckel, M. J. Enright, N. Panahpour Eslami, D. M. Kroupa, D. R. Gamelin, B. M. Cossairt, Modeling Equilibrium Binding at Quantum Dot Surfaces Using Cyclic Voltammetry. *Nano Lett.* **20**, 2620–2624 (2020).

19. Y. Huang, T. A. Cohen, B. M. Sperry, H. Larson, H. A. Nguyen, M. K. Homer, F. Y. Dou, L. M. Jacoby, B. M. Cossairt, D. R. Gamelin, C. K. Luscombe, Organic building blocks at inorganic nanomaterial interfaces. *Mater. Horiz.* **9**, 61–87 (2022).

20. F. W. Eagle, N. Park, M. Cash, B. M. Cossairt, Surface Chemistry and Quantum Dot Luminescence: Shell Growth, Atomistic Modification, and Beyond. *ACS Energy Lett.* **6**, 977–984 (2021).

21. A. M. Schimpf, K. E. Knowles, G. M. Carroll, D. R. Gamelin, Electronic Doping and Redox-Potential Tuning in Colloidal Semiconductor Nanocrystals. *Acc. Chem. Res.* **48**, 1929–1937 (2015).

22. Y. Hinuma, A. Grüneis, G. Kresse, F. Oba, Band alignment of semiconductors from density-functional theory and many-body perturbation theory. *Phys. Rev. B*. **90**, 155405 (2014).

23. F. Al Marzouqi, Y. Kim, R. Selvaraj, Shifting of the band edge and investigation of charge carrier pathways in the CdS/g-C_3N_4 heterostructure for enhanced photocatalytic degradation of levofloxacin. *New J. Chem.* **43**, 9784–9792 (2019).

24. J. Castillo-Lora, R. Mitsuhashi, J. M. Mayer, Revealing the Relative Electronic Landscape of Colloidal ZnO and TiO_2 Nanoparticles via Equilibration Studies. *J. Phys. Chem. C*. **123**, 10262–10271 (2019).

25. M. Ballabio, E. Cánovas, Electron Transfer at Quantum Dot–Metal Oxide Interfaces for Solar Energy Conversion. *ACS Nanosci. Au*. **2**, 367–395 (2022).

26. G. M. Carroll, E. Y. Tsui, C. K. Brozek, D. R. Gamelin, Spectroelectrochemical Measurement of Surface Electrostatic Contributions to Colloidal CdSe Nanocrystal Redox Potentials. *Chem. Mater.* **28**, 7912–7918 (2016).

27. N. Stumme, A. S. Perera, A. Horvath, S. Ruhunage, D. H. Duffy, E. M. Koltonowski, J. Tupper, C. Dzierba, A. D. McEndaffer, C. M. Teague, C. Risko, S. K. Shaw, Probing Redox Properties of Extreme Concentrations Relevant for Nonaqueous Redox-Flow Batteries. *ACS Appl. Energy Mater.* **6**, 2819–2831 (2023).

28. L. S. Li, N. Pradhan, Y. Wang, X. Peng, High Quality ZnSe and ZnS Nanocrystals Formed by Activating Zinc Carboxylate Precursors. *Nano Lett.* **4**, 2261–2264 (2004).

29. C. B. Murray, D. J. Norris, M. G. Bawendi, Synthesis and characterization of nearly monodisperse CdE (E = sulfur, selenium, tellurium) semiconductor nanocrystallites. *J. Am. Chem. Soc.* **115**, 8706–8715 (1993).

30. Z. A. Peng, X. Peng, Formation of High-Quality CdTe, CdSe, and CdS Nanocrystals Using CdO as Precursor. *J. Am. Chem. Soc.* **123**, 183–184 (2001).

31. Z. A. Peng, X. Peng, Nearly Monodisperse and Shape-Controlled CdSe Nanocrystals via Alternative Routes: Nucleation and Growth. *J. Am. Chem. Soc.* **124**, 3343–3353 (2002).

32. X. Peng, J. Wickham, A. P. Alivisatos, Kinetics of II-VI and III-V Colloidal Semiconductor Nanocrystal Growth: "Focusing" of Size Distributions. *J. Am. Chem. Soc.* **120**, 5343–5344 (1998).

33. D. Mocatta, G. Cohen, J. Schattner, O. Millo, E. Rabani, U. Banin, Heavily Doped Semiconductor Nanocrystal Quantum Dots. *Science*. **332**, 77–81 (2011).

34. C. He, Z. Zhang, C. Wang, Y. Jiang, E. A. Weiss, Reversible Modulation of the Electrostatic Potential of a Colloidal Quantum Dot through the Protonation Equilibrium of Its Ligands. *J. Phys. Chem. Lett.* **8**, 4981–4987 (2017).

35. K. V. Prather, J. T. Stoffel, E. Y. Tsui, Z-Type Ligand Coordination at Colloidal Semiconductor Nanocrystals Modifies Surface Electrostatics. *Chem. Mater.* **34**, 3976–3984 (2022).

36. K. V. Prather, J. T. Stoffel, E. Y. Tsui, Redox Reactions at Colloidal Semiconductor Nanocrystal Surfaces. *Chem. Mater.* **35**, 3386–3403 (2023).

37. P. R. Brown, D. Kim, R. R. Lunt, N. Zhao, M. G. Bawendi, J. C. Grossman, V. Bulović, Energy Level Modification in Lead Sulfide Quantum Dot Thin Films through Ligand Exchange. *ACS Nano*. **8**, 5863–5872 (2014).

38. M. Jakob, H. Levanon, P. V. Kamat, Charge Distribution between UV-Irradiated TiO_2 and Gold Nanoparticles: Determination of Shift in the Fermi Level. *Nano Lett.* **3**, 353–358 (2003).

39. G. A. Grinbom, M. Saraf, C. Saguy, A. C. Bartnik, F. Wise, E. Lifshitz, Density of states in a single PbSe/PbS core-shell quantum dot measured by scanning tunneling spectroscopy. *Phys. Rev. B*. **81**, 245301 (2010).

40. P. Liljeroth, L. Jdira, K. Overgaag, B. Grandidier, S. Speller, D. Vanmaekelbergh, Can scanning tunnelling spectroscopy measure the density of states of semiconductor quantum dots? *Phys. Chem. Chem. Phys.* **8**, 3845 (2006).

41. A. S. Karakoti, S. Sanghavi, P. Nachimuthu, P. Yang, S. Thevuthasan, Probing the Size- and Environment-Induced Phase Transformation in CdSe Quantum Dots. *J. Phys. Chem. Lett.* **2**, 2925–2929 (2011).

42. J. J. A. Lozeman, P. Führer, W. Olthuis, M. Odijk, Spectroelectrochemistry, the future of visualizing electrode processes by hyphenating electrochemistry with spectroscopic techniques. *The Analyst*. **145**, 2482–2509 (2020).

43. W. Kaim, J. Fiedler, Spectroelectrochemistry: the best of two worlds. *Chem. Soc. Rev.* **38**, 3373 (2009).

44. G. M. Carroll, C. K. Brozek, K. H. Hartstein, E. Y. Tsui, D. R. Gamelin, Potentiometric Measurements of Semiconductor Nanocrystal Redox Potentials. *J. Am. Chem. Soc.* **138**, 4310–4313 (2016).

45. S. K. Haram, B. M. Quinn, A. J. Bard, Electrochemistry of CdS Nanoparticles: A Correlation between Optical and Electrochemical Band Gaps. *J. Am. Chem. Soc.* **123**, 8860–8861 (2001).

46. S. Lee, C. E. Hoyer, C. Liao, X. Li, V. C. Holmberg, Phase-Controlled Synthesis and Quasi-Static Dielectric Resonances in Silver Iron Sulfide ($AgFeS_2$) Nanocrystals. *Small*. **18**, 2104975 (2022).

47. R. A. Beck, S. Sun, X. Xu, D. R. Gamelin, T. Cao, X. Li, Understanding External Pressure Effects and Interlayer Orbital Exchange Pathways in the Two-Dimensional Magnet─Chromium Triiodide. *J. Phys. Chem. C*. **126**, 19327–19335 (2022).

48. D. E. Sommer, D. Mutter, S. T. Dunham, Defects in Na-, K-, and Cd-Doped $CuInSe_2$: Canonical Thermodynamics Based on Ab Initio Calculations. *IEEE J. Photovolt.* **7**, 1143–1152 (2017).

49. D. Mutter, S. T. Dunham, Calculation of Defect Concentrations and Phase Stability in Cu_2 $ZnSnS_4$ and Cu_2 $ZnSnSe_4$ From Stoichiometry. *IEEE J. Photovolt.* **5**, 1188–1196 (2015).

50. M. C. De Siena, D. E. Sommer, S. E. Creutz, S. T. Dunham, D. R. Gamelin, Spinodal Decomposition During Anion Exchange in Colloidal Mn2+-Doped CsPbX3 (X = Cl, Br) Perovskite Nanocrystals. *Chem. Mater.* **31**, 7711–7722 (2019).

51. D. E. Sommer, S. T. Dunham, Understanding copper diffusion in CuInSe2 with first-principles based atomistic and continuum models. *J. Appl. Phys.* **130**, 235701 (2021).

52. D. E. Sommer, D. R. Gamelin, S. T. Dunham, Defect formation in Yb-doped $CsPbCl_3$ from first principles with implications for quantum cutting. *Phys. Rev. Mater.* **6**, 025404 (2022).

53. H. Liu, C. K. Brozek, S. Sun, D. B. Lingerfelt, D. R. Gamelin, X. Li, A Hybrid Quantum-Classical Model of Electrostatics in Multiply Charged Quantum Dots. *J. Phys. Chem. C*. **121**, 26086–26095 (2017).

54. S. Lee, S. Ghosh, C. E. Hoyer, H. Liu, X. Li, V. C. Holmberg, Iron-Content-Dependent, Quasi-Static Dielectric Resonances and Oxidative Transitions in Bornite and Chalcopyrite Copper Iron Sulfide Nanocrystals. *Chem. Mater.* **33**, 1821–1831 (2021).

55. C. Freysoldt, B. Grabowski, T. Hickel, J. Neugebauer, G. Kresse, A. Janotti, C. G. Van de Walle, First-principles calculations for point defects in solids. *Rev. Mod. Phys.* **86**, 253–305 (2014).

56. I. du Fossé, S. Lal, A. N. Hossaini, I. Infante, A. J. Houtepen, Effect of Ligands and Solvents on the Stability of Electron Charged CdSe Colloidal Quantum Dots. *J. Phys. Chem. C*. **125**, 23968–23975 (2021).

57. D. A. Fenoll, M. Sodupe, X. Solans-Monfort, Influence of Capping Ligands, Solvent, and Thermal Effects on CdSe Quantum Dot Optical Properties by DFT Calculations. *ACS Omega*. **8**, 11467–11478 (2023).

58. S. Yang, D. Prendergast, J. B. Neaton, Tuning Semiconductor Band Edge Energies for Solar Photocatalysis via Surface Ligand Passivation. *Nano Lett.* **12**, 383–388 (2012).

59. G. Kresse, J. Furthmüller, Efficient iterative schemes for *ab initio* total-energy calculations using a plane-wave basis set. *Phys. Rev. B*. **54**, 11169–11186 (1996).

60. G. Kresse, D. Joubert, From ultrasoft pseudopotentials to the projector augmented-wave method. *Phys. Rev. B*. **59**, 1758–1775 (1999).

61. G. Kresse, J. Hafner, *Ab initio* molecular dynamics for liquid metals. *Phys. Rev. B*. **47**, 558–561 (1993).

62. M. Abatal, A. R. Ruiz-Salvador, N. C. Hernández, A DFT-based simulated annealing method for the optimization of global energy in zeolite framework systems: Application to natrolite, chabazite and clinoptilolite. *Microporous Mesoporous Mater.* **294**, 109885 (2020).

63. S. L. Dudarev, G. A. Botton, S. Y. Savrasov, C. J. Humphreys, A. P. Sutton, Electron-energy-loss spectra and the structural stability of nickel oxide: An LSDA+U study. *Phys. Rev. B*. **57**, 1505–1509 (1998).

64. M. Aras, Ç. Kılıç, Combined hybrid functional and DFT+ *U* calculations for metal chalcogenides. *J. Chem. Phys.* **141**, 044106 (2014).

65. S. Smidstrup, T. Markussen, P. Vancraeyveld, J. Wellendorff, J. Schneider, T. Gunst, B. Verstichel, D. Stradi, P. A. Khomyakov, U. G. Vej-Hansen, M.-E. Lee, S. T. Chill, F. Rasmussen, G. Penazzi, F. Corsetti, A. Ojanperä, K. Jensen, M. L. N. Palsgaard, U. Martinez, A. Blom, M. Brandbyge, K. Stokbro, QuantumATK: an integrated platform of electronic and atomic-scale modelling tools. *J. Phys. Condens. Matter*. **32**, 015901 (2020).

66. V. Wang, N. Xu, J.-C. Liu, G. Tang, W.-T. Geng, VASPKIT: A user-friendly interface facilitating high-throughput computing and analysis using VASP code. *Comput. Phys. Commun.* **267**, 108033 (2021).

67. K. Momma, F. Izumi, *VESTA 3* for three-dimensional visualization of crystal, volumetric and morphology data. *J. Appl. Crystallogr.* **44**, 1272–1276 (2011).

68. A. Stukowski, Visualization and analysis of atomistic simulation data with OVITO–the Open Visualization Tool. *Model. Simul. Mater. Sci. Eng.* **18**, 015012 (2009).

69. J. S. Kim, S. H. Kim, H. S. Lee, Energy spacing and sub-band modulation of Cu doped ZnSe quantum dots. *J. Alloys Compd.* **914**, 165372 (2022).

70. R. Viswanatha, S. Brovelli, A. Pandey, S. A. Crooker, V. I. Klimov, Copper-Doped Inverted Core/Shell Nanocrystals with "Permanent" Optically Active Holes. *Nano Lett.* **11**, 4753–4758 (2011).

71. S. Gul, J. K. Cooper, C. Corrado, B. Vollbrecht, F. Bridges, J. Guo, J. Z. Zhang, Synthesis, Optical and Structural Properties, and Charge Carrier Dynamics of Cu-Doped ZnSe Nanocrystals. *J. Phys. Chem. C*. **115**, 20864–20875 (2011).

72. S. Gul, J. K. Cooper, P.-A. Glans, J. Guo, V. K. Yachandra, J. Yano, J. Z. Zhang, Effect of Al^{3+} Co-doping on the Dopant Local Structure, Optical Properties, and Exciton Dynamics in Cu^{+}-Doped ZnSe Nanocrystals. *ACS Nano*. **7**, 8680–8692 (2013).

73. Z. Zhang, D. Li, R. Xie, W. Yang, Insights into the Energy Levels of Semiconductor Nanocrystals by a Dopant Approach. *Angew. Chem. Int. Ed.* **52**, 5052–5055 (2013).

74. N. K. Morozova, E. M. Gavrishchuk, I. A. Karetnikov, V. V. Blinov, V. S. Zimogorskii, V. G. Galstyan, E. V. Yashina, ZnSe·CuO Luminescence at High Doping Levels. **38** (2002).

75. M. C. Weidman, M. E. Beck, R. S. Hoffman, F. Prins, W. A. Tisdale, Monodisperse, Air-Stable PbS Nanocrystals *via* Precursor Stoichiometry Control. *ACS Nano*. **8**, 6363–6371 (2014).

76. L. Cademartiri, E. Montanari, G. Calestani, A. Migliori, A. Guagliardi, G. A. Ozin, Size-Dependent Extinction Coefficients of PbS Quantum Dots. *J. Am. Chem. Soc.* **128**, 10337–10346 (2006).

77. M. Shim, P. Guyot-Sionnest, n-type colloidal semiconductor nanocrystals. *Nature*. **407**, 981–983 (2000).

78. J. Jasieniak, M. Califano, S. E. Watkins, Size-Dependent Valence and Conduction Band-Edge Energies of Semiconductor Nanocrystals. *ACS Nano*. **5**, 5888–5902 (2011).

79. W. Koh, A. Y. Koposov, J. T. Stewart, B. N. Pal, I. Robel, J. M. Pietryga, V. I. Klimov, Heavily doped n-type PbSe and PbS nanocrystals using ground-state charge transfer from cobaltocene. *Sci. Rep.* **3**, 2004 (2013).

80. C. Giansante, L. Carbone, C. Giannini, D. Altamura, Z. Ameer, G. Maruccio, A. Loiudice, M. R. Belviso, P. D. Cozzoli, A. Rizzo, G. Gigli, Colloidal Arenethiolate-Capped PbS Quantum Dots: Optoelectronic Properties, Self-Assembly, and Application in Solution-Cast Photovoltaics. *J. Phys. Chem. C*. **117**, 13305–13317 (2013).

81. J. J. Li, Y. A. Wang, W. Guo, J. C. Keay, T. D. Mishima, M. B. Johnson, X. Peng, Large-Scale Synthesis of Nearly Monodisperse CdSe/CdS Core/Shell Nanocrystals Using Air-Stable Reagents via Successive Ion Layer Adsorption and Reaction. *J. Am. Chem. Soc.* **125**, 12567–12575 (2003).

82. X. Peng, M. C. Schlamp, A. V. Kadavanich, A. P. Alivisatos, Epitaxial Growth of Highly Luminescent CdSe/CdS Core/Shell Nanocrystals with Photostability and Electronic Accessibility. *J. Am. Chem. Soc.* **119**, 7019–7029 (1997).

83. F. García-Santamaría, Y. Chen, J. Vela, R. D. Schaller, J. A. Hollingsworth, V. I. Klimov, Suppressed Auger Recombination in "Giant" Nanocrystals Boosts Optical Gain Performance. *Nano Lett.* **9**, 3482–3488 (2009).

84. W. W. Yu, X. Peng, Formation of High-Quality CdS and Other II-VI Semiconductor Nanocrystals in Noncoordinating Solvents: Tunable Reactivity of Monomers. *Angew. Chem. Int. Ed.* **41**, 2368–2371 (2002).

85. W. W. Yu, L. Qu, W. Guo, X. Peng, Experimental Determination of the Extinction Coefficient of CdTe, CdSe, and CdS Nanocrystals. *Chem. Mater.* **15**, 2854–2860 (2003).

86. J. D. Rinehart, A. M. Schimpf, A. L. Weaver, A. W. Cohn, D. R. Gamelin, Photochemical Electronic Doping of Colloidal CdSe Nanocrystals. *J. Am. Chem. Soc.* **135**, 18782–18785 (2013).

87. H. Zhu, T. Lian, Wavefunction engineering in quantum confined semiconductor nanoheterostructures for efficient charge separation and solar energy conversion. *Energy Environ. Sci.* **5**, 9406 (2012).

88. B. E. Conway, *Electrochemical Supercapacitors: Scientific Fundamentals and Technological Applications* (Kluwer Academic / Plenum Publishers, New York, 1999).

89. R. Van Noorden, The rechargeable revolution: A better battery. *Nature*. **507**, 26–28 (2014).

90. P. Simon, Y. Gogotsi, Materials for electrochemical capacitors. *Nat. Mater.* **7**, 845–854 (2008).

91. Y. Wang, Y. Song, Y. Xia, Electrochemical capacitors: mechanism, materials, systems, characterization and applications. *Chem. Soc. Rev.* **45**, 5925–5950 (2016).

92. C. K. Brozek, D. Zhou, H. Liu, X. Li, K. R. Kittilstved, D. R. Gamelin, Soluble Supercapacitors: Large and Reversible Charge Storage in Colloidal Iron-Doped ZnO Nanocrystals. *Nano Lett.* **18**, 3297–3302 (2018).

93. E. Pomerantseva, F. Bonaccorso, X. Feng, Y. Cui, Y. Gogotsi, Energy storage: The future enabled by nanomaterials. *Science*. **366**, eaan8285 (2019).

94. M. G. El-Shaarawy, M. Khairy, M. A. Mousa, Structural, electrical and electrochemical properties of ZnO nanoparticles synthesized using dry and wet chemical methods. *Adv. Powder Technol.* **31**, 1333–1341 (2020).

95. C. K. Brozek, K. H. Hartstein, D. R. Gamelin, Potentiometric Titrations for Measuring the Capacitance of Colloidal Photodoped ZnO Nanocrystals. *J. Am. Chem. Soc.* **138**, 10605–10610 (2016).

96. D. A. Schwartz, N. S. Norberg, Q. P. Nguyen, J. M. Parker, D. R. Gamelin, Magnetic Quantum Dots: Synthesis, Spectroscopy, and Magnetism of Co^{2+}- and Ni^{2+}-Doped ZnO Nanocrystals. *J. Am. Chem. Soc.* **125**, 13205–13218 (2003).

97. I. Kriegel, F. Scotognella, L. Manna, Plasmonic doped semiconductor nanocrystals: Properties, fabrication, applications and perspectives. *Phys. Rep.* **674**, 1–52 (2017).

98. D. Zhou, P. Wang, C. R. Roy, M. D. Barnes, K. R. Kittilstved, Direct Evidence of Surface Charges in n-Type Al-Doped ZnO. *J. Phys. Chem. C*. **122**, 18596–18602 (2018).

99. V. Pavlyuk, R. Misztal, W. Ciesielski, Structural and Thermal Characterization of the Incorporation of Lithium into ZnO. *Eur. J. Inorg. Chem.* **2014**, 925–931 (2014).

100. A. M. Schimpf, C. E. Gunthardt, J. D. Rinehart, J. M. Mayer, D. R. Gamelin, Controlling Carrier Densities in Photochemically Reduced Colloidal ZnO Nanocrystals: Size Dependence and Role of the Hole Quencher. *J. Am. Chem. Soc.* **135**, 16569–16577 (2013).

101. P. Atkins, J. de Paula, J. Keeler, *Atkins' Physical Chemistry* (Oxford University Press, 2018).

102. M. J. Young, A. M. Holder, S. M. George, C. B. Musgrave, Charge Storage in Cation Incorporated α-MnO_2. *Chem. Mater.* **27**, 1172–1180 (2015).

103. Y. Yuan, C. Zhan, K. He, H. Chen, W. Yao, S. Sharifi-Asl, B. Song, Z. Yang, A. Nie, X. Luo, H. Wang, S. M. Wood, K. Amine, M. S. Islam, J. Lu, R. Shahbazian-Yassar, The influence of large cations on the electrochemical properties of tunnel-structured metal oxides. *Nat. Commun.* **7**, 13374 (2016).

104. J. Z. Olson, P. K. Johansson, D. G. Castner, C. W. Schlenker, Operando Sum-Frequency Generation Detection of Electrolyte Redox Products at Active Si Nanoparticle Li-Ion Battery Interfaces. *Chem. Mater.* **30**, 1239–1248 (2018).

105. J. J. Araujo, C. K. Brozek, H. Liu, A. Merkulova, X. Li, D. R. Gamelin, Tunable Band-Edge Potentials and Charge Storage in Colloidal Tin-Doped Indium Oxide (ITO) Nanocrystals. *ACS Nano*. **15**, 14116–14124 (2021).

106. J. J. Goings, A. M. Schimpf, J. W. May, R. W. Johns, D. R. Gamelin, X. Li, Theoretical Characterization of Conduction-Band Electrons in Photodoped and Aluminum-Doped Zinc Oxide (AZO) Quantum Dots. *J. Phys. Chem. C*. **118**, 26584–26590 (2014).

107. R. L. Chamousis, F. E. Osterloh, Use of potential determining ions to control energetics and photochemical charge transfer of a nanoscale water splitting photocatalyst. *Energy Env. Sci*. **7**, 736–743 (2014).

108. D. A. Hines, P. V. Kamat, Recent Advances in Quantum Dot Surface Chemistry. *ACS Appl. Mater. Interfaces*. **6**, 3041–3057 (2014).

109. E. K. Raulerson, D. M. Cadena, M. A. Jabed, C. D. Wight, I. Lee, H. R. Wagner, J. T. Brewster, B. L. Iverson, S. Kilina, S. T. Roberts, Using Spectator Ligands to Enhance Nanocrystal-to-Molecule Electron Transfer. *J. Phys. Chem. Lett.* **13**, 1416–1423 (2022).

110. R. Seoudi, A. A. Shabaka, M. Kamal, E. M. Abdelrazek, W. Eisa, Dependence of spectroscopic and electrical properties on the size of cadmium sulfide nanoparticles. *Phys. E Low-Dimens. Syst. Nanostructures*. **45**, 47–55 (2012).

111. M. B. Wilker, J. K. Utterback, S. Greene, K. A. Brown, D. W. Mulder, P. W. King, G. Dukovic, Role of Surface-Capping Ligands in Photoexcited Electron Transfer between CdS Nanorods and FeFe Hydrogenase and the Subsequent H_2 Generation. *J. Phys. Chem. C*. **122**, 741–750 (2018).

112. G. K. Grandhi, R. Tomar, R. Viswanatha, Low temperature dynamics of surface and bulk electronic structure of quantum dots. *Mater. Res. Express*. **4**, 094001 (2017).

113. K. Tvrdy, P. A. Frantsuzov, P. V. Kamat, Photoinduced electron transfer from semiconductor quantum dots to metal oxide nanoparticles. *Proc. Natl. Acad. Sci.* **108**, 29–34 (2011).

114. H. Zhao, C. Sun, H. Yin, Y. Li, J. Gao, Y. Shi, M. Sun, Tunable electron transfer rate in a CdSe/ZnS-based complex with different anthraquinone chloride substitutes. *Sci. Rep.* **9**, 7756 (2019).

115. J. J. Hopfield, Exciton States and Band Structure in CdS and CdSe. *J. Appl. Phys.* **32**, 2277–2281 (2004).

116. D. C. Grauer, A. P. Alivisatos, Ligand Dissociation Mediated Charge Transfer Observed at Colloidal $W_{18}O_{49}$ Nanoparticle Interfaces. *Langmuir*. **30**, 2325–2328 (2014).

117. K. J. Schnitzenbaumer, T. Labrador, G. Dukovic, Impact of Chalcogenide Ligands on Excited State Dynamics in CdSe Quantum Dots. *J. Phys. Chem. C*. **119**, 13314–13324 (2015).

118. C. L. Hartley, M. L. Kessler, C. Y. Dones Lassalle, A. M. Camp, J. L. Dempsey, Effects of Ligand Shell Composition on Surface Reduction in PbS Quantum Dots. *Chem. Mater.* **33**, 8612–8622 (2021).

119. Y. B. Vogel, M. Stam, J. T. Mulder, A. J. Houtepen, Long-Range Charge Transport via Redox Ligands in Quantum Dot Assemblies. *ACS Nano*. **16**, 21216–21224 (2022).

120. N. C. Anderson, M. P. Hendricks, J. J. Choi, J. S. Owen, Ligand Exchange and the Stoichiometry of Metal Chalcogenide Nanocrystals: Spectroscopic Observation of Facile Metal-Carboxylate Displacement and Binding. *J. Am. Chem. Soc.* **135**, 18536–18548 (2013).

121. C. J. Barrows, V. A. Vlaskin, D. R. Gamelin, Absorption and Magnetic Circular Dichroism Analyses of Giant Zeeman Splittings in Diffusion-Doped Colloidal Cd1–xMnxSe Quantum Dots. *J. Phys. Chem. Lett.* **6**, 3076–3081 (2015).

122. A. L. Kaledin, T. Lian, C. L. Hill, D. G. Musaev, A Hybrid Quantum Mechanical Approach: Intimate Details of Electron Transfer between Type-I CdSe/ZnS Quantum Dots and an Anthraquinone Molecule. *J. Phys. Chem. B*. **119**, 7651–7658 (2015).

123. X. Wang, M. Liu, Z. Zhou, L. Guo, Toward Facet Engineering of CdS Nanocrystals and Their Shape-Dependent Photocatalytic Activities. *J. Phys. Chem. C*. **119**, 20555–20560 (2015).

124. Y. Zhang, J. Zhang, K. Tse, L. Wong, C. Chan, B. Deng, J. Zhu, Pseudo-Hydrogen Passivation: A Novel Way to Calculate Absolute Surface Energy of Zinc Blende (111)/(T T T) Surface. *Sci. Rep.* **6**, 20055 (2016).

125. R. Gomes, A. Hassinen, A. Szczygiel, Q. Zhao, A. Vantomme, J. C. Martins, Z. Hens, Binding of Phosphonic Acids to CdSe Quantum Dots: A Solution NMR Study. *J. Phys. Chem. Lett.* **2**, 145–152 (2011).

126. J. De Roo, Z. Zhou, J. Wang, L. Deblock, A. J. Crosby, J. S. Owen, S. S. Nonnenmann, Synthesis of Phosphonic Acid Ligands for Nanocrystal Surface Functionalization and Solution Processed Memristors. *Chem. Mater.* **30**, 8034–8039 (2018).

127. F. Wang, R. Tang, W. E. Buhro, The Trouble with TOPO; Identification of Adventitious Impurities Beneficial to the Growth of Cadmium Selenide Quantum Dots, Rods, and Wires. *Nano Lett.* **8**, 3521–3524 (2008).

128. S. J. Lim, A. Schleife, A. M. Smith, Optical determination of crystal phase in semiconductor nanocrystals. *Nat. Commun.* **8**, 14849 (2017).

129. S. Chakravarthi, C. Pederson, Z. Kazi, A. Ivanov, K.-M. C. Fu, Impact of surface and laser-induced noise on the spectral stability of implanted nitrogen-vacancy centers in diamond. *Phys. Rev. B*. **104**, 085425 (2021).

130. Y.-H. Kim, S. B. Zhang, Y. Yu, L. F. Xu, C. Z. Gu, Dihydrogen bonding, p-type conductivity, and origin of change in work function of hydrogenated diamond (001) surfaces. *Phys. Rev. B*. **74**, 075329 (2006).

131. J. Furthmüller, J. Hafner, G. Kresse, Dimer reconstruction and electronic surface states on clean and hydrogenated diamond (100) surfaces. *Phys. Rev. B*. **53**, 7334–7351 (1996).

132. K. T. Kluherz, S. T. Mergelsberg, J. J. De Yoreo, D. R. Gamelin, Structure and Stability of the Iodide Elpasolite, Cs2AgBiI6. *Chem. Mater.* **35**, 5699–5708 (2023).

Python code for data analysis

```
import matplotlib.pyplot as plt
import matplotlib.cbook as cbook

import numpy as np
import pandas as pd

from scipy.signal import find_peaks
from statistics import mean
import os

## assign directory
directory = "C:\\Users\\annme\\Desktop\\potentials\\cds"
output_dir = os.path.join(directory, "output")
if not os.path.exists(output_dir):
    os.makedirs(output_dir)

# assign ligand names and plot colors
# ligands must match labels in the data .csv files
ligands = ['acid','dda','topo']
plot_colors = ['steelblue','lime','g']

# iterate over all files in directory
for filename in os.listdir(directory):
    f = os.path.join(directory, filename)
    # checking if it is a .csv file
    if os.path.isfile(f) and filename.endswith(".csv"):
        print(filename)
        # assign data_name using file name
        data_name = filename.replace(".csv", "")
        # read data into frame
        frame = pd.read_csv(f)

        # plot original data
        fig, ax = plt.subplots()
        # plot potential for each ligand vs distance 'd'
        for lig in range(len(ligands)):
            ligand = ligands[lig]
            ax.plot(frame['d'], frame[ligand], color=plot_colors[lig], label=ligand)
        plt.xlim(0,80)
        ax.set_title(data_name)
        ax.set_ylabel('planar average potential (eV)')
        ax.set_xlabel('distance, (Bohr)')
        plt.legend()
        # save original data plot to [data_name]_orig.svg file
        fig.savefig(os.path.join(output_dir,"{}_orig.svg".format(data_name)))

        # create dataframe for measurements
        init_val = np.zeros(len(ligands))
        metrics = {'orig_bulk':init_val, 'orig_vac':init_val,
                   'adj_bulk':init_val, 'adj_vac':init_val,
                   'pot_dif':init_val}
        metrics_df = pd.DataFrame(metrics, index=ligands)
        # define "bulk" region for peak finding
        index_from = next(x for x, val in enumerate(frame['d']) if val>14)
        index_to = next(x for x, val in enumerate(frame['d']) if val>35)
        frame_mid = frame[index_from:index_to]
        # fid peaks and vacuum - iterate through ligands
        for lig in range(len(ligands)):
            ligand = ligands[lig]
```

```
    # find peaks in the "bulk" region
    peaks, _ = find_peaks(frame_mid[ligand])
    metrics_df.loc[ligand, 'orig_bulk'] = mean(frame_mid.iloc[peaks][ligand])
    # find flat "vacuum" region
    grad = np.gradient(frame[ligand], frame['d'])
    flat = np.where(abs(grad)<0.315)[0]
    n = 0
    vacuum = []
    for i in range(len(flat)-1):
        if (flat[i+1]-flat[i]==1):
            vacuum.append(flat[i])
            n = n+1
        else:
            vacuum = []
            n = 0
        if n>15: break
    metrics_df.loc[ligand, 'orig_vac'] = mean(frame.iloc[vacuum][ligand])
    # find [vacuum]-[peak] potential difference
    metrics_df.loc[ligand, 'pot_dif'] = \
    metrics_df.loc[ligand, 'orig_vac'] - \
    metrics_df.loc[ligand, 'orig_bulk']

    # change index of peaks to match full range
    peaks_mid = [x + index_from for x in peaks]
    # add peak markers in the "bulk" region to plot
    plt.plot(frame.iloc[peaks_mid]['d'], frame.iloc[peaks_mid][ligand], "x", color = 'r')
    # add vacuum markers to plot
    plt.plot(frame.iloc[vacuum]['d'], frame.iloc[vacuum][ligand], "x", color = 'black')

# save original data plot with marked "bulk" and "vacuum" regions
# to [data_name]_orig_x.svg file
fig.savefig(os.path.join(output_dir,"{}_orig_x.svg".format(data_name)))
# show plot for original data with marked "bulk" and "vacuum" regions
plt.show()

# normalize data to oleate ("acid") trace
peaks_o, _ = find_peaks(frame_mid['acid'])
peaks_o_mean = mean(frame_mid.iloc[peaks_o]['acid'])
for lig in range(len(ligands)):
    ligand = ligands[lig]
    peaks_atom, _ = find_peaks(frame_mid[ligand])
    peaks_atom_mean = mean(frame_mid.iloc[peaks_atom][ligand])
    frame[ligand] = frame[ligand] - peaks_atom_mean + peaks_o_mean

# plot data adjusted to oleate ("acid") trace
fig, ax = plt.subplots()
for lig in range(len(ligands)):
    ligand = ligands[lig]
    ax.plot(frame['d'], frame[ligand], color=plot_colors[lig], label=ligand)
plt.xlim(0,80)
ax.set_title(data_name)
ax.set_ylabel('planar average potential (eV)')
ax.set_xlabel('distance, (Bohr)')
plt.legend()

# define "bulk" and "vacuum" regions for peak finding in adjusted plots
index_from = next(x for x, val in enumerate(frame['d']) if val>14)
index_to = next(x for x, val in enumerate(frame['d']) if val>35)
frame_mid = frame[index_from:index_to]
for lig in range(len(ligands)):
    ligand = ligands[lig]
    # find peaks in the "adj-bulk" region
    peaks_, _ = find_peaks(frame_mid[ligand])
```

```
    metrics_df.loc[ligand, 'adj_bulk'] = mean(frame_mid.iloc[peaks_][ligand])
    # find flat "adj-vacuum" region
    grad = np.gradient(frame[ligand], frame['d'])
    flat = np.where(abs(grad)<0.315)[0]
    n = 0
    vacuum = []
    for i in range(len(flat)-1):
        if (flat[i+1]-flat[i]==1):
            vacuum.append(flat[i])
            n = n+1
        else:
            vacuum = []
            n = 0
        if n>15: break
    metrics_df.loc[ligand, 'adj_vac'] = mean(frame.iloc[vacuum][ligand])

    # change index of peaks to match full range
    peaks_mid = [x + index_from for x in peaks_]

# save adjusted data plot to [data_name]_adj.svg file
fig.savefig(os.path.join(output_dir,"{}_adj.svg".format(data_name)))
# show plot for adjusted data
plt.show()

# print and save measurements to [data_name]_metrics.csv file
print(metrics_df)
metrics_df.to_csv(os.path.join(output_dir,"{}_metrics.csv".format(data_name)))
```